Nano-Micro Letters

ISSN 2311-6706
e-ISSN 2150-5551
CN 31-2103/TB

REVIEW

https://doi.org/10.1007/s40820-020-00558-3

Cite as
Nano-Micro Lett.
(2021) 13:38

Received: 26 August 2020
Accepted: 29 October 2020
Published online: 4 January 2021

Strategy and Future Prospects to Develop Room-Temperature-Recoverable NO_2 Gas Sensor Based on Two-Dimensional Molybdenum Disulfide

Abhay V. Agrawal[1], Naveen Kumar[1], Mukesh Kumar[1] ✉

HIGHLIGHTS

- MoS_2 shows enormous potential for gas sensing due to its high surface to volume ratio, position-dependent gas molecules adsorption and easy control on morphology.
- The recent experimental and theoretical strategies to develop NO_2 chemiresistance sensors based on MoS_2 are addressed.
- A detailed overview of the fabrication of MoS_2 chemiresistance sensors in terms of devices, structure, morphology, defects, heterostructures, metal doping, and under light illumination are discussed.

ABSTRACT Nitrogen dioxide (NO_2), a hazardous gas with acidic nature, is continuously being liberated in the atmosphere due to human activity. The NO_2 sensors based on traditional materials have limitations of high-temperature requirements, slow recovery, and performance degradation under harsh environmental conditions. These limitations of traditional materials are forcing the scientific community to discover future alternative NO_2 sensitive materials. Molybdenum disulfide (MoS_2) has emerged as a potential candidate for developing next-generation NO_2 gas sensors. MoS_2 has a large surface area for NO_2 molecules adsorption with controllable morphologies, facile integration with other materials and compatibility with internet of things (IoT) devices. The aim of this review is to provide a detailed overview of the fabrication of MoS_2 chemiresistance sensors in terms of devices (resistor and transistor), layer thickness, morphology control, defect tailoring, heterostructure, metal nanoparticle doping, and through light illumination. Moreover, the experimental and theoretical aspects used in designing MoS_2-based NO_2 sensors are also discussed extensively. Finally, the review concludes the challenges and future perspectives to further enhance the gas-sensing performance of MoS_2. Understanding and addressing these issues are expected to yield the development of highly reliable and industry standard chemiresistance NO_2 gas sensors for environmental monitoring.

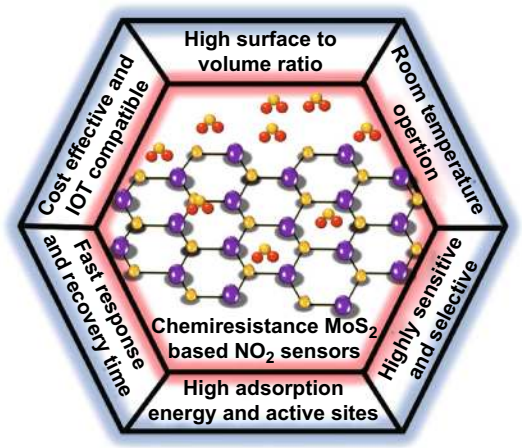

KEYWORDS MoS_2; NO_2 gas sensors; Light illumination; Heterojunction

✉ Mukesh Kumar, mkumar@iitrpr.ac.in
[1] Functional and Renewable Energy Materials Laboratory, Indian Institute of Technology Ropar, Rupnagar, Punjab 140001, India

1 Introduction

The earth's environment consists of various chemical elements, gases, and dust particles such as N_2, O_2, CO, CO_2, NO_2, NH_3. Among these gases, O_2, present in the environment is beneficial to living beings, while some gases, such as CO_2, NO_2, are toxic and dangerous. The presence of these toxic gases is majorly fixed in the environment. Among all toxic and dangerous gases, NO_2, a hazardous gas, acidic in nature, highly reactive with a stinky smell is continuously being produced and liberated in the atmosphere due to human activity [1–6]. NO_2 is produced by fossil fuel burning, forest fires, industry and motor vehicles [7–9]. NO_2 has recently become a matter of concern in Europe and Australia, owing to its increased concentration. The recent satellite data revealed an unprecedented increase in NO_2 concentration due to motor vehicles, power plants and wildfire in Europe and Australia in the year 2019 [10–14]. Moreover, after the worldwide outbreak of the novel COVID-19 virus, the lockdown was implemented in highly affected countries, which resulted in the shutdown of factories, manufacturing firms, and transport. This lockdown benefitted the world inadvertently with a dramatic reduction in NO_2 emissions. Importantly, the high reactiveness of NO_2 molecules with moisture and its tendency to create an acidic environment makes NO_2 production thought of concern [5, 15, 16]. It causes respiratory diseases beyond a certain NO_2 concentration limit in the environment, e.g. coronary assault, cancer, asthma, pneumonia, coughing and bronchitis [16–18]. The presence of NO_2 in the environment makes the air hazy and thick, which reduces the visibility of human eyes. In addition, the World Health Organization (WHO) reported that major cities around the world had failed to qualify the WHO's air quality standards [19]. An estimated 30.7 million people died due to cardiovascular disease, cancer and chronic respiratory disease in 2016 [19, 20]. Thus, considering the toxicity and hazardousness of NO_2 gas, there is an urgent need to detect the precise levels of NO_2 gas in the environment.

A hazardous gas in the environment can be detected by a gas sensor which is an electronic device having two-essential parts; a receptor unit and a transducer unit. Chemical information generated due to gas molecules exposure is gathered and stored in the form of chemical energy in the receptor device. The energy stored in the transducer component is transmuted to an analytical signal [21]. Hulanicki et al. categorized the gas sensors into six classes depending on the transducer mechanism: (1) electrochemical, (2) mass sensitive, (3) magnetic, (4) optical, (5) thermoelectric, and (6) electrical. The classification of gas sensors is carried out on the basis of their transducer operating principle. In today's fast moving and unstoppable life, the rapid detection of low concentration of toxic gases is indispensable. Among all gas sensors, electrical transducer-based NO_2 gas sensor has grabbed the prime attention due to their easy handling, simple fabrication process, easy to connect with IOTs, real-time gas detection provision, low-cost and power consumptions, small size and long-term stability in harsh working conditions. In electrical or chemical resistance sensors, the resistance of the sensing material is changed due to charge transfer between the gas molecules and the sensing materials whenever the gas molecules are exposed to the sensing device. The chemiresistance gas sensors have extensive applications in H_2, NH_3, NO, H_2S, NO_2 gas detection in the environment, industry, cities, space science, transport, vehicles, cultivation, indoors, and various health sectors [22, 23]. Some figures of merits are specified to compare the performance of a gas sensor with different sizes, morphologies and operating conditions, i.e. sensor response, response and recovery time, and selectivity. Generally, sensor response is the ratio of change in resistance with exposure of gas molecules to the resistance of the film before the exposure of gas molecules. It is given by different forms of expression by many groups such as $S = \frac{(R_{gas}-R_{air})}{R_{air}}$; $\frac{(R_{air}-R_{gas})}{R_{air}}$; $\frac{(I_{gas}-I_{air})}{I_{air}}$; $\frac{R_{gas}}{R_{air}}$, $\frac{R_{air}}{R_{gas}}$ [17, 24–36]. Where, $R_{gas}(I_{gas})$ is the resistance (current) of the sensing film in the presence of the gas molecules, R_{air} (I_{air}) is the resistance (current) of the sensing film in the presence of the air and S is the sensor response. The response time is the time taken by any gas sensor to attain 90% of the maximum sensor response when the gas is introduced to the sensor. The recovery time is the time taken by any gas sensor to reach 10% of the maximum sensor response when the gas is turned off. The capacity of a gas sensor to respond to a particular gas in the presence of other gases is called selectivity ability of the gas sensor. Usually, sensing films are sensitive to every gas present in the atmosphere at a same time. Also, some gases have nearly same sensor response for specific sensing film. It is therefore difficult to determine the exact change in the sensor response

 https://doi.org/10.1007/s40820-020-00558-3

generated by the target gas. Therefore, sensing film must be very selective for the target gas with highest sensor response.

Graphene as a 2D material has some unique properties such as the large surface area (2360 $m^2 g^{-1}$), zero rest mass of charge carriers near Dirac points and high carrier mobility 200,000 $cm^2 V^{-1} s^{-1}$ at room temperature (RT) [37–42]. Similarly, other 2D layered materials have numerous properties and applications in comparison to their bulk form [43–45]. The intriguing properties of 2D TMDCs are their high surface to volume ratio, absence of dangling bonds in the pristine form, strong spin–orbit coupling interaction and the high interaction ability for the gas molecules adsorption [46–52]. These features of 2D materials offer interest in exploring their new fundamental physics [32, 53]. The layer-dependent mechanical, electronic, and optical properties of 2D materials create curiosity to learn and explore their fundamental properties [54–56]. A one atom thick layer of graphene has shown an appealing role in gas sensing by detecting 1 ppb concentration of various gases such as NH_3, NO_2, H_2O, and CO [57]. Gas sensors based on graphene have been widely inspected and employed owing to its high carrier mobility, mechanical strengths greater than to steal, remarkable optical and electronic properties [58–60]. Despite having an impressive sensor response and response time, the NO_2 sensors have suffered from long recovery time owing to the very high adsorption energy of gas molecules with graphene [61–63]. In terms of growth and production, the synthesis of graphene is very costly with the use of toxic chemicals at high temperatures [64–67]. Another challenge associated with graphene is the production of high quality and large surface area graphene film, which is very difficult to attain and the presence of any non-carbon elements disrupts the hexagonality of graphene [68]. Moreover, graphene has zero bandgap, and less environment stability which reduces the gas-sensing performance and long term stability of graphene-based sensors [47, 69].

These limitations of graphene mold the direction of research to discover new nonzero bandgap 2D materials like MoS_2, $MoSe_2$, $MoTe_2$, WS_2, WSe_2, BP, and many more [70–83]. The interaction between the gas molecules and sensing materials is the indelible part of any gas-sensing process. In 2D materials, especially MoS_2, is at the forefront in the race of an ideal gas-sensing material [84, 85]. The other substitutes of the 2D materials family are WS_2, WSe_2, $NbSe_2$, $MoTe_2$, etc. [86–90]. However, most of the research on NO_2 detection is carried out with MoS_2. MoS_2-based gas sensors have achieved noticeable research interest in recent years. MoS_2 has already shown emerging environmental applications in energy storage, light interaction, flexible electronic devices and in biofield due to its semiconducting nature [50, 91–96]. MoS_2 has two possible crystal phases, trigonal and hexagonal, where hexagonal is semiconducting while trigonal is having metallic nature [97]. The presence of weak Van der Waals force enables the easy isolation of layers from bulk MoS_2. The indirect bandgap of 1.2 eV in bulk MoS_2 is converted to a direct bandgap of 1.8 eV for monolayer MoS_2 [50, 98, 99]. The absence of dangling bonds provides stability to pristine MoS_2 flakes in liquid and gaseous media in the presence of oxygen. These facilities make MoS_2 compatible for gas-sensing application [100]. The low binding energy of 6.1 and 13.9 eV is needed to create S and Mo vacancies, respectively, which can turn the edges of MoS_2 flakes into metallic sites [101, 102]. MoS_2 has a tunable bandgap compared to graphene which increases the overall sensing performance of MoS_2 film [103]. The MoS_2 flakes have strong photoluminescence (PL) absorption due to the presence of direct bandgap, helpful to design the optical gas sensors. The high on/off ratio (10^8), the high carrier mobility of 400 $cm^2 V^{-1} s^{-1}$ at RT, low effective electron mass of 0.48 m_e are advantageous for developing fast gas sensors [54, 104–106]. Owing to these electronic properties, any minor change in the electron concentration of MoS_2 flakes can be easily detected. MoS_2 flakes have four Raman active modes ($E_{1g}, E^1_{2g}, A_{1g}, E^2_{2g}$). The E^1_{2g} mode is an in-plane mode and A_{1g} is an out of plane mode [107, 108]. Chakraborty et al. studied in situ Raman spectroscopy of single-layer MoS_2 flakes [109]. It has been found that E^1_{2g} is not sensitive to electron doping while the A_{1g} mode is very sensitive to electron doping [109]. With higher electron concentration, the A_{1g} mode gets soften due to stronger electron–phonon coupling mode than E^1_{2g} mode [109]. These vibrational characteristics are ideal for the chemiresistance gas sensors where charge concentration has remained an important parameter. Furthermore, MoS_2 film has impressive mechanical and optical properties with high Young's modulus up to 300 GPa, deformity up to 11% without any fracture and amazing transparent nature, making it a potential candidate for optical and flexible devices [110–114]. Moreover, MoS_2 flakes can be bent up to the radius of 0.75 mm, without deteriorating its electronic properties [115]. Excellent gas molecules detection ability,

enormous active sites, large surface to volume ratio and presence of favorable adsorption sites have endorsed MoS_2 as the unique sensing material. The development and key accomplishment of MoS_2-based NO_2 gas sensors in last 8 years are summarized in Fig. 1. With the discovery of the graphene by mechanical exfoliation (ME) technique by the Geim and Novoselov, they further revealed in 2005 that the ME technique can also be employed to thin down the other bulk materials such as MoS_2 [43]. Following the uniqueness of the MoS_2, Li et al. developed the NO_x sensitive gas sensor

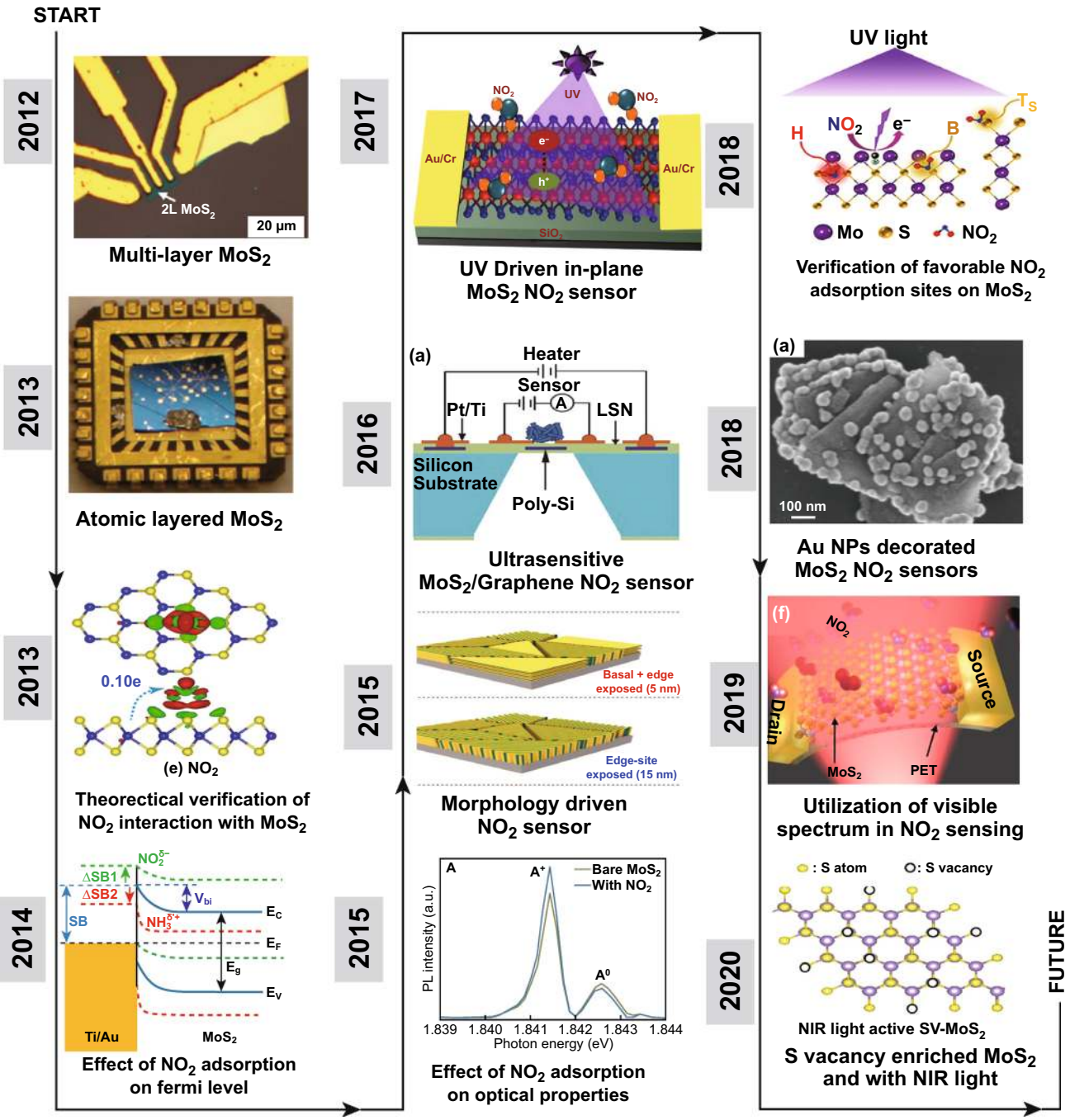

Fig. 1 Schematic representation of the 8-year journey of MoS_2-based NO_2 sensors. Reproduced with permission from Refs. [34, 118]. Copyright @ Wiley-VCH; Refs. [17, 32, 35, 36, 119, 120, 123]. Copyright @ American Chemical Society; Ref. [117]. Copyright @ Springer; Ref. [121]. Copyright @ AIP Publishing; Ref. [122]. Copyright @ Elsevier

https://doi.org/10.1007/s40820-020-00558-3

[34]. In a similar year, He et al. developed the NO_2 sensor based on multilayer MoS_2 flakes and confirm the role of MoS_2 in NO_2 detection [42]. The fundamental research to study the electronic properties of MoS_2 was boosted after the fabrication of first MoS_2 transistor by Kis et al. [116]. In 2013, Late et al. studied the role of negative and positive back gate voltage on NO_2 sensing by fabricating the MoS_2 field effect transistor (FET) [17]. The year 2014–2015 was devoted to the charge transfer mechanism due to the gas molecules exposure. Yue et al. investigated theoretically and confirmed that gas molecule detection in MoS_2 is attributed to the charge transfer process [117]. Liu et al. demonstrated that NO_2 gas adsorption strongly affects the Schottky barrier height (SBH) [36]. Cho et al. performed the in-situ PL spectroscopy and investigated the p-type doping in MoS_2 flakes due to NO_2 exposure [32].

Till 2015, MoS_2 has been established itself as the potential candidate for the gas sensing with a well-defined gas-sensing mechanism. However, MoS_2-based NO_2 sensors suffered from the incomplete recovery due to the high adsorption of NO_2 on MoS_2. Cho et al. studied the role of active sites in gas sensing [35]. NO_2 adsorption is very high at the active sites in MoS_2. The active sites are highest at the edges due to presence of dangling bonds, defects and vacancies, while the terrace of MoS_2 is inert due to absence of dangling bonds. Authors synthesized MoS_2 flakes of three different orientations: in-plane MoS_2, mixed MoS_2 and vertical aligned MoS_2 flakes. The number of active sites and NO_2 sensing performance were highest in the case of vertical MoS_2 flakes. Several studies have been published in parallel years for the fabrication of hybrid MoS_2 heterostructures to improve the charge transfer in MoS_2. Long et al. fabricated the low temperature MoS_2/graphene hybrid structure and develop ultrasensitive NO_2 sensors up to 50 ppb [118]. Although researchers have achieved full recovery at high temperatures, but the production of RT-recoverable gas sensors has remained a challenging task.

Since 2017, light-assisted NO_2 sensors have attracted the worldwide scientific community. Rahul et al. in 2017, investigated the role of ultraviolet (UV) light in basal plane MoS_2 flakes and achieved the full recovery at RT under UV light illumination. Agrawal et al. demonstrated the role of favorable NO_2 adsorption sites in MoS_2 by synthesizing the unique morphology of MoS_2 flakes [119, 120]. Metal NP doping has theoretically proven to be a great combination for enhanced gas sensor response, reactivity and recovery in the past years. Zhou et al. developed the MoS_2 sensor decorated with Au NPs [121]. It is important to remember that, until 2018, most of the published report used only UV light to boost the efficiency of the sensing light. In the next years, 2019 and 2020 (running) researchers fabricated the visible spectra and near infrared (NIR) spectra-driven NO_2 sensors [122, 123].

Thus we may conclude that gas-sensing characteristics of MoS_2 film-based device are highly dependent on size, shape, thickness, morphology, growth direction, polytype composition, defects, metal functionality and the hybrid structure of MoS_2 films. These factors can be used to classify MoS_2-based NO_2 sensors [25, 42, 124].

Apart from the experimental efforts, theoretical studies have also played a noticeable role in designing the experiments and predicting the gas-sensing potential of the proposed materials [125]. Theoretical methods such as density functional theory (DFT) always prove their advantage in terms of time, efforts and cost [125]. DFT provides a broad and detailed view to understand the fundamental mechanism happening between the gas molecules and the sensing material [126, 127]. The key features of DFT are the pre-calculation of the charge transfer and understanding of fundamental interaction between the sensing material and gas molecules. These features are helpful to understand the physical and chemical adsorption of gas molecules, theoretical estimation of defects, their effects on electronic and optical properties and functionalizing the defects with other materials and noble metals. Very few reviews are focused on both the theoretical contribution and the experimental contribution of MoS_2 for NO_2 sensing.

The goal of this review is to discuss in detail the MoS_2-based NO_2 gas sensors and to provide in-depth insights into previously established theoretical and experimental approaches. We focused on the various properties of MoS_2 which played a vital role in gas sensing. Mainly, the role of 1T and 2H MoS_2 phases, large surface area available in MoS_2 film for gas molecule adsorption, faster charge transport in MoS_2, effect of modulating favourable adsorption sites via morphology, optical properties and defects available in MoS_2 will be discussed.

Considering all these points, we have categorized various strategies for enhancing the performances of MoS_2 sensors as follows: role of device structure (resistor and transistor), monolayer MoS_2, multilayer MoS_2, defect tailoring, morphology engineering, heterostructures, functionalizing

with noble metals and light-assisted NO_2 sensors. We have focused our present review in the direction as mentioned above and a schematic view is shown in Fig. 2.

We also focus a little bit on the traditional NO_2 sensing materials such as metal oxides and carbon-based nanomaterials to gain a clear difference between NO_2 sensing performance of traditional materials and MoS_2.

A tremendous effort has been employed to develop fast, high sensor response, selective and low-cost NO_2 electrical sensors. Various nanomaterial-based sensors from zero dimension (0D, quantum dots) [128–135] to two dimensions (2D, metal oxides, TMDCs) [27, 81, 83, 136–138] showed their exceptional detection ability to detect parts per billion (ppb) NO_2 gas traces [139–143]. Every nanomaterials has its own merits and demerits in the NO_2 gas detection. The traditional metal oxides (ZnO, SnO_2, TiO_2, In_2O_3, WO_3 etc.) based NO_2 sensors showed a fast response and high sensor response. However, the highly sensitive nature of metal oxides to humidity reduces the sensor response and stability of gas sensors. Moreover, for accelerating the interaction between the gas molecules and metal oxides, metal oxides gas sensors are need to operate at a higher temperature (250–500 °C). High temperature results in the agglomeration of nanomaterials and increase the grain size of the metal oxide film [28, 143–155]. On the contrary, the carbon material-based NO_2 sensors provide the high sensor response but at RT the desorption rate of gas molecules is too slow. Thus, the CNT-based NO_2 sensors are suffered from long recovery time [30, 156–158]. In summary, metal oxide and carbon-based NO_2 sensors are suffered from thermal safety due to high temperature, structure complexity and complex device fabrication, which restricts the use of metal oxides in smart, wearable and next-generation device for the internet of things (IoT).

The problems associated with metal oxide and carbon-based NO_2 sensor have demanded the development of new noble materials with advanced gassensing properties. In Fig. 3, we have summarized the NO_2 detection performance of various reported traditional materials-based sensors such as ZnO, SnO_2, CNTs, TiO_2, In_2O_3 SnS_2, and WO_3, in terms of operating temperature, sensor response and recovery time [26, 91, 154, 159–197]. Most of the traditional nanomaterial-based NO_2 sensors reported good sensor response at high operating temperatures (purple star) and simultaneously, they also suffered from the high recovery time (green circles). However, for an ideal gas sensor, it should be operated near RT for high sensing performances. The ideal sensor should have a high sensor response, lower response, and recovery time near to RT, as shown in star region of Fig. 3. Therefore, there is a great demand to develop a low temperature, highly sensitive and fast NO_2 sensors.

The roadmap of the review is as follows. In Sect. 1, we introduced MoS_2 as the NO_2 sensors and addressed its benefits over the traditional metal oxide sensors. In Sect. 2, we will present some peculiar properties of MoS_2, which played a critical role in gas molecule adsorption. Section 3 is focused on the interaction mechanism of NO_2 with MoS_2 and effect of NO_2 on electronic, optical and surface

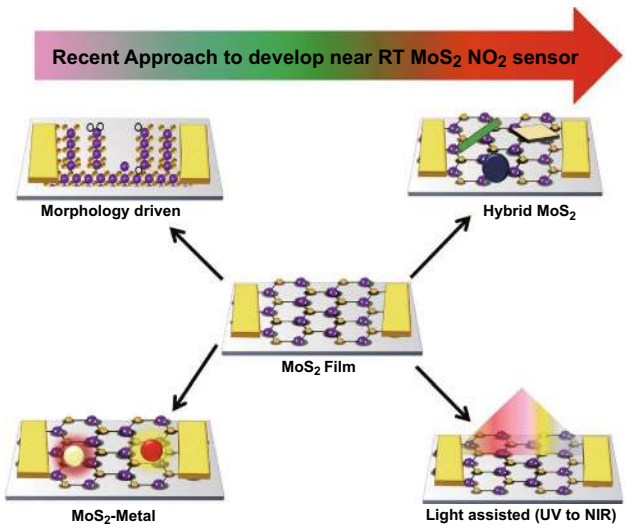

Fig. 2 Schematic representation of strategies adopted to develop a high-performance NO_2 gas sensor based on MoS_2 flakes

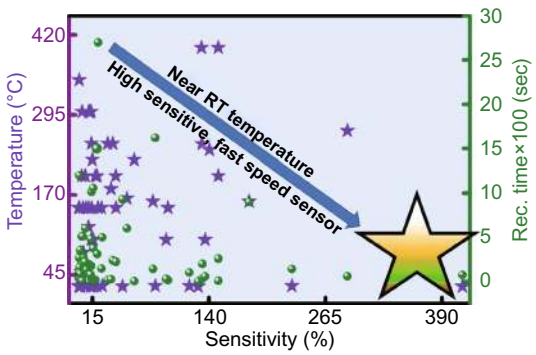

Fig. 3 Traditional material-based NO_2 gas sensors. Most of the traditional NO_2 sensors have a high operating temperature requirement. The colored star area shows the ideal states for a gas sensor. Data has been taken from Refs. [26, 91, 154, 160–209]

https://doi.org/10.1007/s40820-020-00558-3

properties. In Sect. 4, we will discuss several theoretical findings in which, interaction between NO_2 and MoS_2 is discussed. Section 5 covers the experimental reports where bare MoS_2, morphology-driven MoS_2, metal-doped MoS_2, vacancy-driven and photon-assisted MoS_2-based NO_2 sensors will be discussed briefly. In Sect. 6, we are going to present some findings where MoS_2-based heterostructures are utilized for NO_2 sensing. Finally, in Sect. 7, we will conclude our review and discussed the future of MoS_2-based NO_2 sensor.

2 MoS_2: A Unique Material for Gas Sensing

2.1 Structure of MoS_2

The single layer of MoS_2 has two polymorphs: trigonal prismatic (2H-MoS_2 Phase) and octahedral phase (1T-MoS_2 Phase), belonging to D_{3h} and D_{3d} point groups, respectively. Both polytype structures are shown in Fig. 4a, c [210]. Here, H and T depict hexagonal and trigonal symmetry, respectively, while digits equate to layers repeat per unit cells. In general, the 2H phase is obtained by synthesizing MoS_2 film using methods such as mechanical exfoliation (ME), chemical vapor deposition (CVD) or ultrasonication [108, 211]. The 1T phase is preferred by the Li intercalation method. The 2H and 1T phases has been widely studied experimentally and theoretically. The 2H-MoS_2 phase is semiconducting, while the 1T-MoS_2 phase exhibits metallic nature. The varied electronic nature of MoS_2 can be understood using crystal field theory (CFT). In CFT, five d orbital $d_{x^2-y^2}$, d_{z^2}, d_{xy}, d_{yz} and d_{zx} of transition metal (Mo) are non-degenerate. These d-bands are located between the bonding (σ) and antibonding bands (σ^*), shown in Fig. 4b, d. In trigonal prismatic (D_{3h}), the orbitals splits into three levels, d_{z^2} (a_1), $d_{x^2-y^2}+d_{xy}$ (e) and $d_{yz}+d_{zx}$ (e'). The octahedral group divided into levels e_g having d_{z^2} and $d_{x^2-y^2}$ orbital and in t_{2g} having d_{xy}, d_{yz} and d_{zx} [212]. When the highest orbitals are partially filled the MoS_2 possess the metallic like conductivity (1T-MoS_2, Fig. 4d) and if the highest orbitals are fully filled, MoS_2 behave like semiconductor (2H-MoS_2, Fig. 4b). In recent years, a lot of research work has been done on 2H-MoS_2 phases in gas-sensing applications and many of them addressed in the next sections [17, 34, 35, 42, 120, 213, 214]. The 1T-MoS_2 has higher active sites and electronic conductivity reaches up to sixfold higher than the 2H-MoS_2 [99]. Mark et al. prepared a stable metallic phase of MoS_2 and they observed an enhanced catalytic performance in 1T phase [215]. In addition, the metallic MoS_2 showed enhanced photoluminescence due to higher sulfur vacancies [99]. Furthermore, Kappera et al. studied the device performance of both phases and observed the low contact resistance at zero bias gate voltage. The low contact resistance generates high drive current with high mobility of 50 $cm^2\ V^{-1}\ s^{-1}$ [216, 217]. These all properties showed that 1T-MoS_2 is an important phase for NO_2 gas sensing. Thus, consideration of the role of both phases in NO_2 sensing is equally important.

2.2 Large Surface Area for Gas Molecule Adsorption

In contrast to metal oxides, the MoS_2 has a large specific surface area. The large surface area provides maximum adsorption sites for the adsorption of gas molecules and enhances the surface perturbation in the presence of gas molecules. Moreover, in chemiresistance gas sensors, sensor response is directly proportional to the change in the resistance arises due to the adsorption of gas molecules on the surface [42, 218]. Tongay et al. proposed that if one O_2 molecule gets physiosorbed on the unit cell of MoS_2, it withdraws 0.04e per unit cell and the sheet charge density reduced up to 5×10^{13} cm^{-2} [219]. Therefore, MoS_2 is very sensitive and amenable to be used in gas-sensing devices. In this context, MoS_2 established himself as the promising chemical sensing material due to large highly sensitive surface. CVD, ME, and hydrothermal methods are the most popular methods for synthesizing MoS_2 for the gas-sensing devices. Among them, the most effective and occupied method to grow large size wafer-scale MoS_2 flakes is the CVD. We have prepared a comparative graph of flakes sizes with the two most prominent methods i.e., ME and CVD. It has been observed that individual flakes size grown by the ME method can go maximum up to 10 μm. However, with CVD, MoS_2 flakes of larger size can be grown in comparison with ME. It is worth to mention, we collected data of domain size of only individual MoS_2 single-layer flakes generated by ME and CVD methods for the data in Fig. 4e. CVD can grow highly uniform, high density, large area and control on morphology of the film while the ME can synthesize highly pure MoS_2 flakes, which is desirable for many electrical and optical applications. Agrawal et al. synthesized uniform

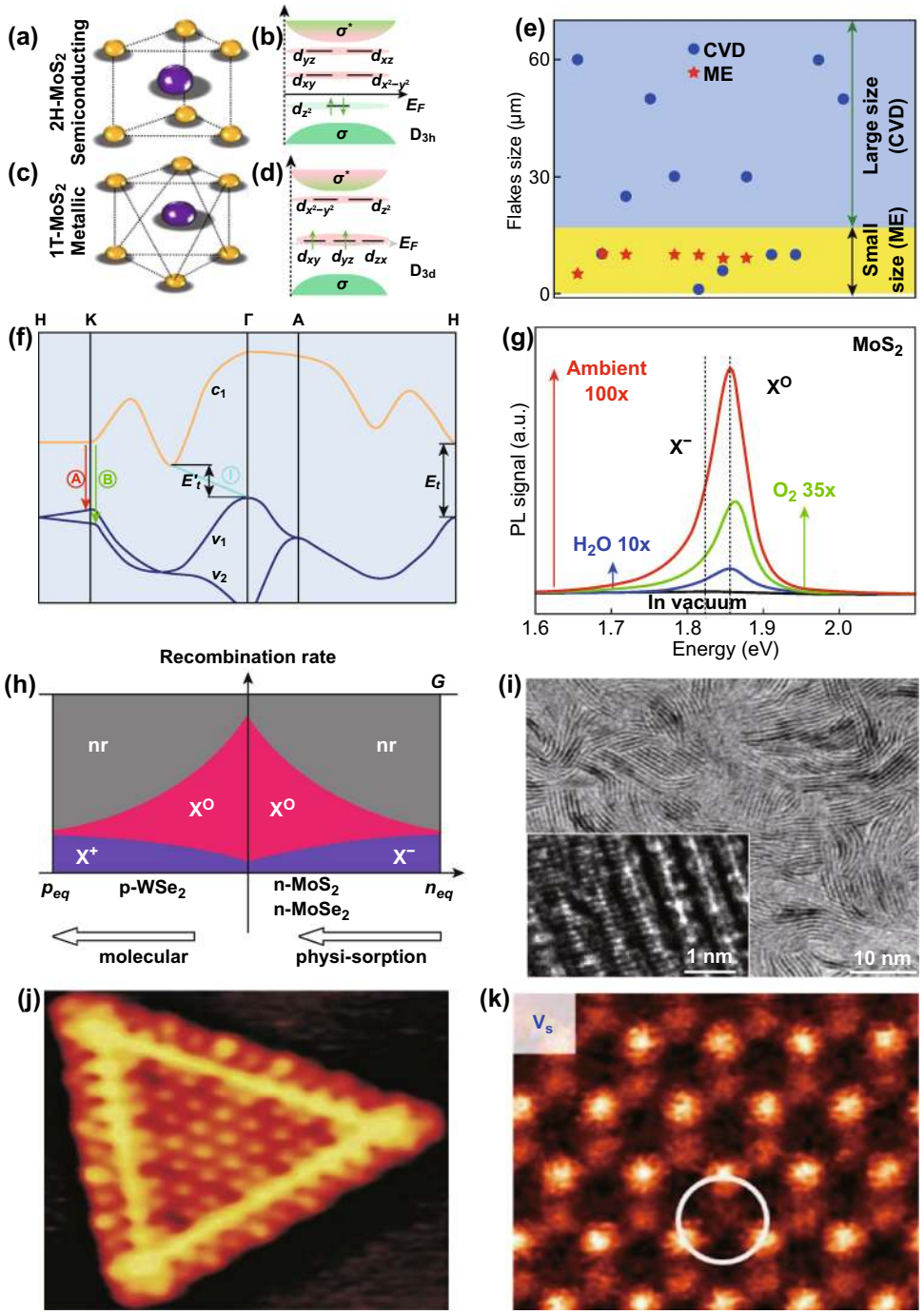

Fig. 4 **a** Schematic structure of 2H-MoS_2. **b** *d*-orbital filling of the semiconducting 2H-MoS_2. **c** Schematic structure of 1T-MoS_2. **d** *d*-orbital filling of the semiconducting 1T-MoS_2. **e** The reported domain size of individual monolayer MoS_2 flakes from the ME and CVD technique. CVD provides a larger flake size compared to the ME technique. The data of MoS_2 flakes size has been taken from Refs. [50, 107, 220, 222–239]. **f** Band structure of MoS_2. The 'A' and 'B' PL peaks are corresponding to the direct bandgap (E_g) transition of MoS_2. Reproduced with permission from Ref. [50]. Copyright (2010) American Physical Society. **g** Spectral change in PL due to exposure of O_2 alone, H_2O alone and with both. O_2 and H_2O incorporate p-type doping which contribute to a blue shift in the peaks. **h** Rate of recombination with neutral exciton and charge trion as a function of charge density in n-type MoS_2 and p-type $MoSe_2$. Reproduced with permission from Ref. [219]. Copyright (2013) American Chemical Society. **i** TEM image of the as grown vertical aligned MoS_2 flakes. The edges have high catalytic activity than the basal plane and enhance the reactivity of the gas molecules. Reproduced with permission from Ref. [240]. Copyright (2013) American Chemical Society. **j** STM image of the triangular MoS_2 flakes where yellow perimeters were showing the presence of the metallic states at the edges. Reproduced with permission from Ref. [241]. Copyright (2001) American Physical Society. **k** ADF images of monovacancy S intrinsic defects. Reproduced with permission from Ref. [242]. Copyright (2013) American Chemical Society

 https://doi.org/10.1007/s40820-020-00558-3

vertical MoS_2 flakes of 1×2 cm^2 size on SiO_2/Si substrate. Furthermore, Lin et al. synthesized large size MoS_2 flakes of 308 μm [220]. Zhan et al. synthesized the centimeter size MoS_2 layer by CVD method [221]. The nucleation rate, supply of precursors, S and MoO_3 powder, temperature and the carrier gas flow rate, by CVD is mainly responsible for large area MoS_2 growth [221, 222]. CVD provides great control on the nucleation rate and mass transport. MoS_2 flakes size is increased with time as the more and more nucleation center and sites grow over substrate. Hence, CVD is the better option to grow the large area MoS_2 flakes and to fabricate the gas-sensing devices.

2.3 Impact of Gas Adsorption on Optical Properties of MoS_2

The photoluminescence (PL) is an essential characterizations to detect changed in the electron concentration of a 2D material-based gas sensor. Gas-sensing ability of 2D materials is governed by either electron depletion or accumulation that depend on the doping behavior of the exposed gas molecules.

The nature of dopants critically affect the PL spectra of MoS_2. MoS_2 has two well-reported PL peaks 'A' and 'B'. These PL peaks are emerged due to the splitting of the valence band in v_1 and v_2 [50]. The valence band splitting at the K-point is the collective effect of interlayer spacing and spin–orbit coupling. Figure 4f displays the direct bandgap transition peaks (A and B) and indirect bandgap transition (I) in the MoS_2 crystal structure. The spectral weight of exciton and trions can be significantly tuned by the electrical gating, n-type or p-type molecular adsorption (e.g. H_2O, TCNQ) doping, and defects present at the cracks [219, 243–245].

Nan et al. studied the role of molecular adsorption on the PL through oxygen exposure [246]. Micro PL analysis revealed the enhancement in PL intensity due to molecules adsorption by MoS_2 surface at moderate temperatures in high vacuum ambient. The PL spectroscopy was performed over the as prepared monolayer MoS_2 films, which were annealed for 1 h in vacuum at 350 and 500 °C. It was observed that the PL intensity was increased sixfold after annealing at 350 °C with the blue shift in energy (from 1.79 to 1.81 eV). Moreover, the PL intensity in sample annealed at 500 °C was erratic at different locations. When the MoS_2 film was annealed at 350 °C, the MoS_2 film was uniform and environmental O_2 and H_2O physically got adsorbed by MoS_2 flakes. Both O_2 and H_2O introduced p-type doping in MoS_2. When the flakes annealed at 500 °C, cracks were formed in the film with the generation of defects. At these defects' sites O_2 and H_2O adsorbed chemically and introduced heavy *p* doping. DFT calculations were also performed and calculated charge transfer between the O_2 and pristine MoS_2 was 0.021e, while at the defects site, the charge transfer was 0.997e. Thus, higher charge transfers at the defective sites introduced heavy p-type doping. Tongay et al. also studied the modulation in the PL due to the physisorption of O_2 and H_2O molecules. Physiosorbed O_2 and H_2O molecules bonded weakly with MoS_2 but introduced significant p doping. The variation in PL intensity due to exposure of O_2 alone (green), H_2O alone (blue) and with both (red) shown in Fig. 4g [247]. The 0.04e and 0.01e times charges were transferred from MoS_2 to O_2 and H_2O molecules, respectively. The O_2 and H_2O molecules adsorption modulate the charge concentration in the MoS_2. The electrons of the n-type MoS_2 flakes are depleted by both molecules. Here, the focus has been given on the low energy exciton peak which is the combination of the neutral exciton (X^0) and charge trions (X^+/X^-). In actual, the MoS_2 layer has high sheet charge density $\left(n_{eq}\right)$. The high n_{eq}, destabilizes the neutral exciton X^0 due to electrostatic screening between the holes and free electrons while the X^- stabilizes due to high recombination rate of X^- trions [248]. Hence, with high n_{eq}, the overall PL intensity becomes low. With physisorption and chemisorption of molecules such as O_2 and H_2O, the n_{eq} gets reduced. Hence, the number of electrons available in MoS_2 for trions formation is decreased. Thus, the intensity of X^- decreased and X^0 enhanced with more stabilization, as can be seen from Fig. 4g, h. Moreover, it has been reported that the electronic gating and molecular doping can dramatically tune the PL [219, 244, 245, 249]. As the gas molecule adsorption introduces n or p doping, the study of PL with adsorption of molecules to MoS_2 is an important aspect to understand the nature of the gas molecules.

2.4 High Catalytic Nature and Presence of Metallic States

Another essential feature of MoS_2 is the presence of a large number of active sites for promoting the chemical reactions. Jaramillo et al. identified the active sites on the MoS_2 through

scanning tunneling microscopy (STM) [250]. The MoS_2 samples were synthesized on the Au substrate and STM imaging was performed in the ultra-high vacuum. The STM measurements confirmed that flat MoS_2 edges have bright rims which appeared as bright lines along the flakes perimeter. To validate the high activity of the edges, the hydrogen evolution reactions (HER) activity was investigated which also confirmed the high reactivity of edges. Kong et al. synthesized MoS_2 by the sulfurization of Mo film deposited by e-beam lithography. The tunneling electron microscopy (TEM) image of vertical aligned MoS_2 flakes is shown in Fig. 4i and in inset. It is evident from these studies that edges have highly active site. Thermodynamically, the growth of in-plane MoS_2 is highly probable than the edge oriented MoS_2 flakes. The high activity of the edges boosts the motivation to grow edge-enriched film by forming the various morphology of MoS_2 nanoflakes such as vertical aligned MoS_2, MoS_2 nanowires, MoS_2 spheres etc. Kim et al. fabricated 2D SnS_2 and develop NO_2 sensor by enhancing the active sites [251]. The vertically aligned SnS_2 showed high NO_2 reactivity due to the presence of a large number of active sites in comparison to the basal plane SnS_2. Shim et al. synthesized SiO_2 nanorods (NRs) and decorated them with MoS_2 flakes [252]. These SiO_2 NRs enhanced the catalytic activity of MoS_2 flakes by exposing more edges of MoS_2 flakes [251]. Hence, the NO_2 detection ability of SiO_2 NRs encapsulated with MoS_2 is increased. The MoS_2 surface has maximum number of active sites which enhance the chemical activity of MoS_2 film [240, 253, 254]. Another important feature of MoS_2 flakes is the presence of metallic states at the edges [241]. The MoS_2 edges behaved as the one-dimensional metallic wires and appeared as the bright brim of high conductance, as shown in Fig. 4j. The attention here is given to Mo edges having S dimers. The Mo edges have two metallic wave functions and generate metallic states in MoS_2. Therefore, the presence of metallic edges will be helpful in the fast transfer of generated electron and holes. The generated charge can be rapidly transferred along the edges in edge-enriched MoS_2 and will be helpful in developing the fast responsive and recoverable gas sensors [255].

2.5 Impact of Gas Molecules Adsorption on Schottky Barrier Height

The gas-sensing performance of 2D materials based on chemiresistance gas sensors is critically influenced by the metal contacts [256–259]. In 2D materials, the gas molecule adsorption affects the charge concentrations and carrier density. Depending on the nature of the gas molecules, the charge carrier density either increases or reduces and Fermi level of 2D materials is modulated with gas molecule adsorption. The equilibrium Fermi level of metal and semiconductor before and after exposure to the gas molecule will be different due to variation in the charge carrier density in the sensing film. In chemiresistance sensors, the Schottky barrier height between the metal contact and the 2D material surface can alter the surface charge transfer mechanism. Various studies have been reported to understand the role of Schottky barrier height (SBH) and Schottky barrier modulation (SBM) with gas molecule exposure in traditional gas sensors as well as in 2D material-based gas sensors [260, 261]. The band structure of metal and semiconductor can be divided into two regions: (1) alignment of the energy levels of the metal and semiconductor for charge carrier injection and (2) band bending at the space charge region for charge carrier separation [262]. If the metal and semiconductor work functions are $\emptyset_M$ and $\emptyset_S$ respectively, the SBH determined by the Mott–Schottky rule is given by Eq. (1):

$$\emptyset_b = \emptyset_M - \chi_S \quad (1)$$

Depending on the type of the semiconductor (n-type or p-type), the Schottky or ohmic contact nature of the junction is decided. In 2D materials, ohmic contacts are of great importance due to their low resistance and high charge transfer in terms of high mobility and current on/off ratio [104, 263, 264]. However, the ohmic contacts are not beneficial for gas-sensing point of view. The reason for this is the interaction of gas molecules with sensing film and their effect on the Schottky barrier modulation (SBM) [36, 72]. The importance of the Schottky contact is well established in the metal oxide sensors. Zhou et al. demonstrated the remarkable performance of the ZnO sensors by utilizing the Schottky contact in comparison to the ohmic contact [265]. Similarly, Wei et al. fabricated the ZnO NW-based CO sensor in such a way that one end behaved as the Schottky contact, while the other end behaved as the ohmic contact [266]. Schottky end behaves like a gate terminal and the Schottky barrier height (SBH) was tuned. Nearly 4 times enhanced sensor response with seven times reduce response and recovery time were observed. In all these reports, SBM provides an efficient and enhanced charge transport. Hence, gas-sensing performance is high in the Schottky contacted devices.

 https://doi.org/10.1007/s40820-020-00558-3

2.6 Role of Defects in Gas Molecule Adsorption

In case of MoS_2, defects can be generated during the synthesis or transfer of MoS_2 due to synthesis imperfections [267–270]. In addition, these defects are susceptible to ambient environments conditions [271, 272]. Defects can also be created through the irradiations, metal doping and functionalization [273, 274]. Thus, MoS_2 structures unavoidably have various defects in terms of vacancies, dopants, adsorbates, adatoms, and impurities. On the contrary, the pristine MoS_2 is assumed to have defect free surfaces. However, the synthesis of defect free MoS_2 flakes is quite difficult and convoluted. Defects are easily produced during the synthesis process. Defects crucially affect various mechanical, electronic, optical and catalytic properties. Zhou et al. fabricated MoS_2 and studied the possible structural defects [242]. The authors studied atomic-resolution annular dark field (ADF) images of CVD-grown MoS_2 flakes. The defects were classified into six types (i) mono-sulfur Vacancies (V_S), (ii) di-sulfur vacancies (V_{S2}), (iii) Mo atom with three nearby sulfur (V_{MoS3}), (iv) Mo atom with three di sulfur pairs (V_{MoS6}), (v–vi) Antisite defects, Mo atom at S vacancy site (Mo_{S2}) and S atom at Mo vacancy site ($S2_{Mo}$). The formation energy of these vacancies is studied in term of S chemical potential. The formation energy plot revealed that mono S vacancies are most probable and need lowest formation energies. The ADF image of S vacancy site is shown in Fig. 4k. These defects could play a crucial role in the gas molecule adsorption. The benefits of defects in graphene have already received great attention [275, 276]. The findings of the reports revealed that the sensing mechanism in pristine and defective graphene is completely different. The defective graphene has higher interaction with gas molecules due to the presence of the defects. Interestingly in MoS_2, defects can greatly influence the gas-sensing properties [86, 277]. Moreover, doping defects with substitutional impurities atoms can greatly improve the MoS_2 sensing performances. The effect of dopant and impurities is also well established in graphene. Zhang et al. studied the sensing performance of graphene-doped B, N, Si, Ca, Co and Fe, defective graphene and on pristine graphene [278]. The defective graphene doped with Ca, Co and Fe showed the highest interaction with H_2S molecules. In metal-doped graphene, mixing of the graphene orbitals and metals orbitals is enhanced with H_2S orbitals which leads to the strong interaction.

3 Charge Transfer Mechanism Between NO_2 and MoS_2: Effect on Electronic Properties, Optical Properties, and Metal Contacts/MoS_2 Interface

In the present section, the nature and effect of NO_2 gas molecules on electrical conductivity, PL and MoS_2 band alignment will be addressed. NO_2 is a secondary product generated from the primary NO source as shown by Eq. (2) [279].

$$2NO + O_2 \rightarrow 2NO_2 \quad (2)$$

NO_2 has the electron acceptor nature and behaves as a strong oxidizing agent due to the unpaired electrons of nitrogen atom. NO_2 molecules take the electrons from the sensing materials. Generally, a chemiresistance gas sensor has a sensing layer that detects the presence of interacting gas molecules. The electrical and optical properties changes depending on the nature of interacting gas molecules and the type of semiconducting film. The gas molecules that interact can either behave like a reduction gas (electron donor) or an oxidizing gas (electron acceptor). Similarly, the semiconductor film may also have an n-type or a p-type nature.

In the case of TMDCs materials, gas molecules interaction depends on the nature of TMDC film and gas molecules. The interaction of gas molecules with TMDC film is governed via the physisorption or chemisorption process. The physisorption process occurs with pristine TMDC film while the chemisorption process happens with defective TMDC layers and on the defect sites.

In the case of pristine TMDC films, the gas molecules and TMDC films interact through the physisorption process. The gas molecules have weak adsorption energy and long adsorption distance with pristine TMDC film. Moreover, there is a less charge transfer between the gas molecules and TMDC film with an almost unchanged electronic structure. Hence, gas sensors based on pristine TMDC films have fast recovery but with low sensor response. The physisorption-based gas sensing reported in SnS_2 [175]. The SnS_2 showed a highly selective nature for NO_2 molecules due to the physisorption process. Furthermore, the positive binding energy of O_2 molecules with the SnS_2 surface indicated high surface resistance for oxygen molecules and supported that NO_2 sensing response in SnS_2 was through the physisorption process [175].

In the case of the chemisorption process, defects induce during the synthesis of MoS_2. The gas molecules interact chemically with MoS_2. The chemical interactions of gas molecules enhance gas-sensing performances of sensing material. The adsorption distance between the gas molecules and the adsorption sites is minimal in case of the chemisorption process. Hence, high charge transfer, strong adsorption energy, and significant change in the electronic states have been observed. The charge transfer schematic of NO_2 with the MoS_2 film (n-type or p-type) is shown in Fig. 5a and Eq. (3).

$$NO_2 + e^- \rightarrow NO_2^- \tag{3}$$

Cho et al. experimentally verified the charge transfer mechanism between the MoS_2 and NO_2 gas molecules using PL spectroscopy [32]. The authors synthesized n-type MoS_2 film by the chemical vapor deposition technique. The authors exposed NO_2 gas to MoS_2 film and investigated the charge transfer mechanism using photoluminescence (PL) spectroscopy. The authors observed that with NO_2 exposure, the resistance of the n-type MoS_2 film increased (positive sensor response). The increment in the resistance confirmed that NO_2 withdraws the electrons from the n-type MoS_2 film. NO_2 gas molecules exposure modulates the electron concentration in MoS_2. The change in the electron concentrations dramatically affects the PL. The MoS_2 has two main PL exciton peaks named as 'A' and 'B' [50]. The intensities of these two PL peaks can either decreased or increased with a change in the electron concentrations [243, 244]. The low energy PL peak 'A' can be expanded into a charged trions ($A^{+/-}$) and in neutral exciton (A^0). The MoS_2 flakes grown on the SiO_2 substrate showed dominated behavior of A^+ peak over A^0. Hence, the authors considered the positively charge trion peak (A^+) and neutral exciton peak (A^0). As NO_2 has an electron acceptor nature, it takes the electron from the MoS_2 and intensity of the (A^+) enhanced due to conversion of neutral exciton in (A^+). Actually, the numerous number of holes generated in MoS_2 due to depletion of electrons by NO_2. Therefore, intensity of A^+ trions enhanced and neutral exciton suppressed. Similar behavior is observed in the PL spectroscopy, shown in Fig. 5b. The effect of NO_2 exposure

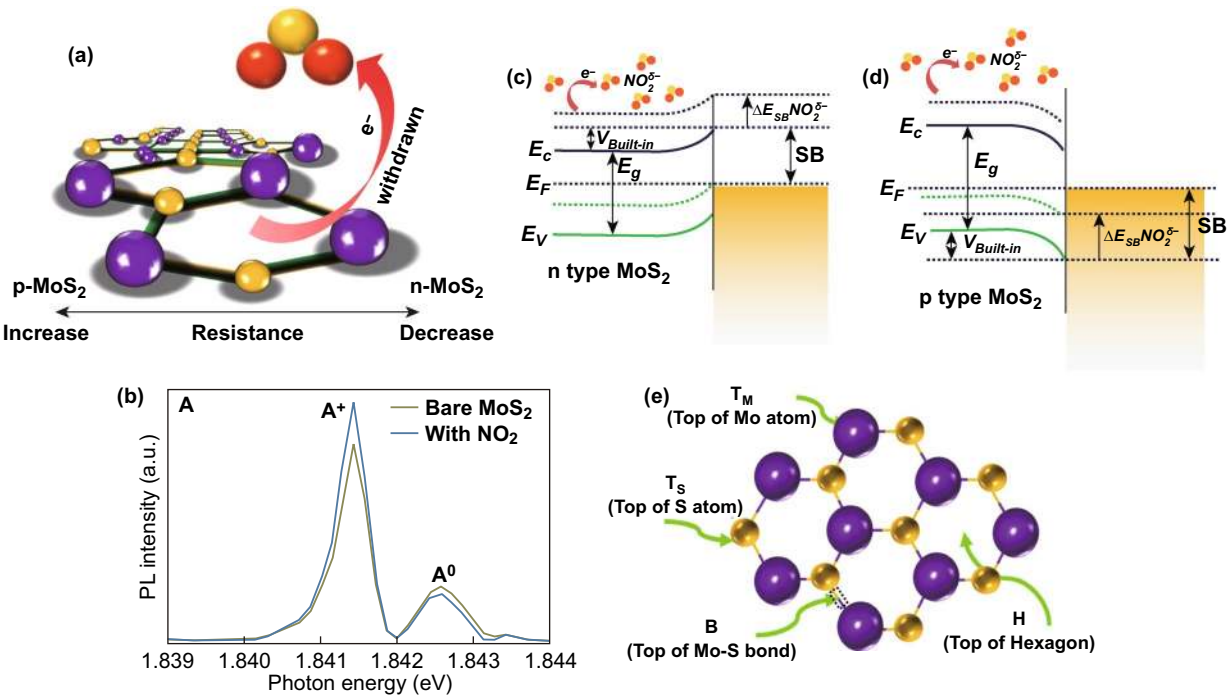

Fig. 5 **a** Schematic interaction of NO_2 gas molecules with the n-type or p-type MoS_2 layer. NO_2 captures the electrons from MoS_2 layer. **b** Effect of NO_2 molecules adsorption on PL spectra. The spectral weight of positively charged trions is increased on the cost of excitons spectral weight in n-type MoS_2. Reproduced with permission from Ref. [32]. Copyright (2015) American Chemical Society. Schottky barrier height modulation after NO_2 molecules adsorption in **c** n-type MoS_2 **d** p-type MoS_2. **e** Four possible NO_2 adsorption sites on MoS_2. Reproduced with permission from Ref. [255]. Copyright (2017) AIP Publishing

https://doi.org/10.1007/s40820-020-00558-3

on the Fermi level of n-type and p-type MoS_2 flakes is shown in Fig. 5c, d. MoS_2 can have both types of semiconducting nature. In both cases, NO_2 exposure depletes the electrons from the MoS_2 and manipulate the charge density in the conduction band. Due to electron extraction, the Fermi level in the n-type MoS_2 film moves downward toward the valence band and correspondingly the SBH and resistance increased. When MoS_2 film has the p-type nature, holes majority increased with NO_2 exposure. The Fermi level move toward the conduction band and SBH and resistance decreased. Thus, NO_2 adsorption critically affects the electronic as well as the optical properties of MoS_2.

Yue et al. theoretically investigated the adsorption of several molecules using DFT on MoS_2 such as H_2, O_2, H_2O, NH_3, NO, NO_2, and CO [117]. Theoretically, gas adsorption behavior is determined by the few terms namely: favorable adsorption sites on MoS_2 for particular gas molecule, distance between the gas molecule and the MoS_2 layer, the binding energy of gas molecule on the MoS_2 layer, charge transfer between the gas molecules and MoS_2 layer, and direction of charge transfer. For adsorption of any gas molecule on a sensing surface, there should be a strong favorable interaction between the gas molecules and MoS_2 flakes, and it should be adsorbed physically or chemically. This interaction is determined in terms of adsorption energy, calculated by Eq. (4):

$$E_a = E_{MoS_2+molecule} - \left(E_{MoS_2} + E_{molecule}\right) \quad (4)$$

where E_a is the adsorption energy, $E_{MoS_2+molecule}$ is the total energy of MoS_2 and the adsorbed gas molecule.E_{MoS_2} and $E_{molecule}$ are the energy of the MoS_2 film and single gas molecule, respectively. For a strong interaction, the adsorption energy should be negative and the interaction process should be exothermic. Another term is the charge transfer process. The charge transfer process depends on the relative position of the highest occupied molecular orbitals (HOMO) and lowest unoccupied molecular orbitals (LUMO). If the Fermi level is below the HOMO, then charge transfer from molecule to sensing surface and gas is called the electron donor, and if the Fermi level is above the LUMO, then the charge transfer from sensing surface to molecule and gas called is the electron acceptor [280].

As mentioned above, the adsorption of the gas molecule is determined in terms of favorable adsorption sites. The gas molecules adsorption are highly position dependent in the case of MoS_2 due to the difference in the adsorption energy and charge transfer for gas molecules at different adsorption sites on MoS_2. The monolayer of MoS_2 has a hexagonally packed structure where Mo atoms are sandwiched between the two layers of S atoms. There are four possible adsorption sites, the H sites (Top of the hexagon), T_S (top of S atom), T_M (top of Mo atom), and B (top of Mo and S bond). The possible sites configurations are shown in Fig. 5e. In the case of NO_2, three different NO_2 molecules orientations have been considered with these four sites, starting from one N atom with N–O bonds parallel to monolayer, two with NO-bonds pointing up or down to monolayer. After the gas molecule adsorption on MoS_2, MoS_2 structure with adsorbed gas molecules is reached to the equilibrium state with the highest adsorption energy.

The minimum distance between the adsorbed gas molecule and the relaxed MoS_2 surface is called as equilibrium height. The importance of distance between the NO_2 and top S layer of MoS_2 is also studied and investigated by Yue et al. The highest adsorption energy was found at an equilibrium height of 2.71 Å. It has to be noted that the highest adsorption energy is negative for adsorption of NO_2 on MoS_2, confirming the favorable adsorption of NO_2 on MoS_2. Among all, depending on the charge transfer and adsorption energy, the most favorable NO_2 orientation was estimated. The H, T_S, and B sites (− 276, − 249, and − 249 meV, respectively) found favorable for NO_2 adsorption while no adsorption on T_M site was observed. The high adsorption energy was attributed to polarization produced in the MoS_2 sheet during NO_2 adsorption. Hence, the interaction was determined by the electrostatic force and lead to strong adsorption energy. From the adsorption energy calculations, the highest favorable NO_2 adsorption site is at the H site. The charge transfer from MoS_2 to NO_2 was found to vary from 0.1e to 0.119e. The positive charge transfer value implies the transfer of charge from MoS_2 to NO_2. The difference in the charge density due to NO_2 exposure further confirmed the charge accumulation and depletion profile. The effect of NO_2 molecule on energy band structure is also studied and it has been found that the adsorbed NO_2 molecule introduces an unoccupied flat impurity state at 0.31 eV above the Fermi level in the conduction band of MoS_2. The used method, supercell size, lattice parameters and available favorable adsorption sites for NO_2 molecules adsorption on MoS_2 by Yue et al., are tabulated in Table 1. Another important aspect of the work is the study of the applied electric field on the NO_2 adsorption on MoS_2. The charge transfer mechanism

Table 1 Method, supercell size (S.S), lattice parameter (L.P) and favorable adsorption sites on MoS_2 calculated by Yue et al. using DFT [117]

Method	S. S (L.P)	H-site			T_S-site			B-site			Reference
		d	E_a	ΔQ	d	E_a	ΔQ	d	E_a	ΔQ	
VASP (LDA)	4×4 (3.12)	2.65	−276	0.1	2.71	−249	0.119	2.62	−249	0.114	[117]

between the adsorbents and absorber is the key to the gas molecule adsorption.

The amount of charge transfer is very sensitive to the electric field. The applied electric field is considered in two perpendicular directions (i) MoS_2 to NO_2 molecule (+E) and (ii) NO_2 to MoS_2 molecule (−E). The charge transfers from MoS_2 to NO_2 increase with an increase in the positive electric field and it tends to decrease when the direction of the field is reversed. The negative electric field forces the electrons to transfer from NO_2 to MoS_2. The external electric field and dipole moment direction are well correlated with each other. Hence the direction of the electric field is greatly affected by the charge transfer values.

4 Theoretical Investigations of NO_2 Adsorption on MoS_2

Here, we discuss the reports where the interaction of NO_2 on MoS_2, the role of MoS_2 polytype and metal doping investigated theoretically.

4.1 Adsorption of NO_2 Gas Molecules on Defective MoS_2

In the present section, we will discuss some theoretical reports in which adsorption of NO_2 is studied on the defective MoS_2. The two types of defects are considered mainly in MoS_2 the monosulfur vacancies and the Mo-doped S vacancy sites.

Owing to the chemical interaction of NO_2 with MoS_2, the adsorption mechanism is governed by the chemisorption mechanism. Li et al. used DFT to study the adsorption of NO_2 molecule on the single S vacancy site [281]. Initially, the effect of vacancies on the electronic structures was studied. The schematic of a MoS_2 unit cell is shown in Fig. 6a. The bandgap with a single S vacancy in MoS_2 was decreased up to 1.07 eV [282, 283]. The S vacancies in 2D materials create midgap states which reduce the bandgap of MoS_2. These states arise due to the unsaturated Mo atoms near the vacant S sites [284]. When NO_2 molecules are adsorbed to the MoS_2 surface, the NO_2 molecule dissociates at the S vacancy sites into NO and O. The dissociated NO has a bond length equivalent to the free NO molecule. Hence, the dissociated O atom is adsorbed on the single S vacancy site and the other part NO is physiosorbed on the O-doped MoS_2. The activation barrier energy and transition states were also calculated. The activation energy of NO_2 dissociation was 0.21 eV and the reaction energy was 2.30 eV, as shown in Fig. 6b. This energetically favored the NO_2 dissociation process. Furthermore, adsorption energy of physiosorbed NO was 0.44 eV which is minimal and facilitates desorption of NO_2 molecules from MoS_2.

Sahoo et al. doped Mo atoms on S vacancy sites, and enhanced adsorption of NO_2, as shown in Fig. 6c, d with a red circle [285]. This type of doping is termed as antisite defects (Mo_S) in MoS_2 (A-MoS_2). The insertion of Mo atoms at the S defects sites are highly probable with physical vapor deposition techniques. A-MoS_2 may be an innovative method to improve the sensor response, selectivity, and sensing performance of the MoS_2 sensor. The insertion of Mo atom at the S vacancy site generates the three midgap states, two states are at -0.02 and -0.11 eV below the Fermi level and the third state above the Fermi level at 0.28 eV. Actually, 4d orbitals of antisite Mo atom is splitted into three states; a (d_z^2) state lies above the fermi level, twofold degenerate $e_1(d_{xy}, d_{x^2-y^2})$, and $e_2\left(d_{yz}, d_{zx}\right)$ due to the C_{3v} symmetry, lies below the Fermi level. It is worth to note that e_1 state splits into $e_1^{'}$ and $e_1^{''}$ levels due to the John Teller distortion while e_2 lies well below the valence band. The corresponding density of states (DOS) and partial density of states (PDOS) of Mo antisite-doped MoS_2 without NO_2 and with NO_2 exposure are shown in Fig. 6e. Finally, when NO_2 gas molecules are exposed to A-MoS_2, the NO_2 interaction process is highly exothermic and higher charge transfer takes place in A-MoS_2 in comparison to the pristine MoS_2. The paramagnetic NO_2 molecules are adsorbed in the tilted configuration. The strong mixing of antisite defect Mo_S and of NO_2 orbitals are

 https://doi.org/10.1007/s40820-020-00558-3

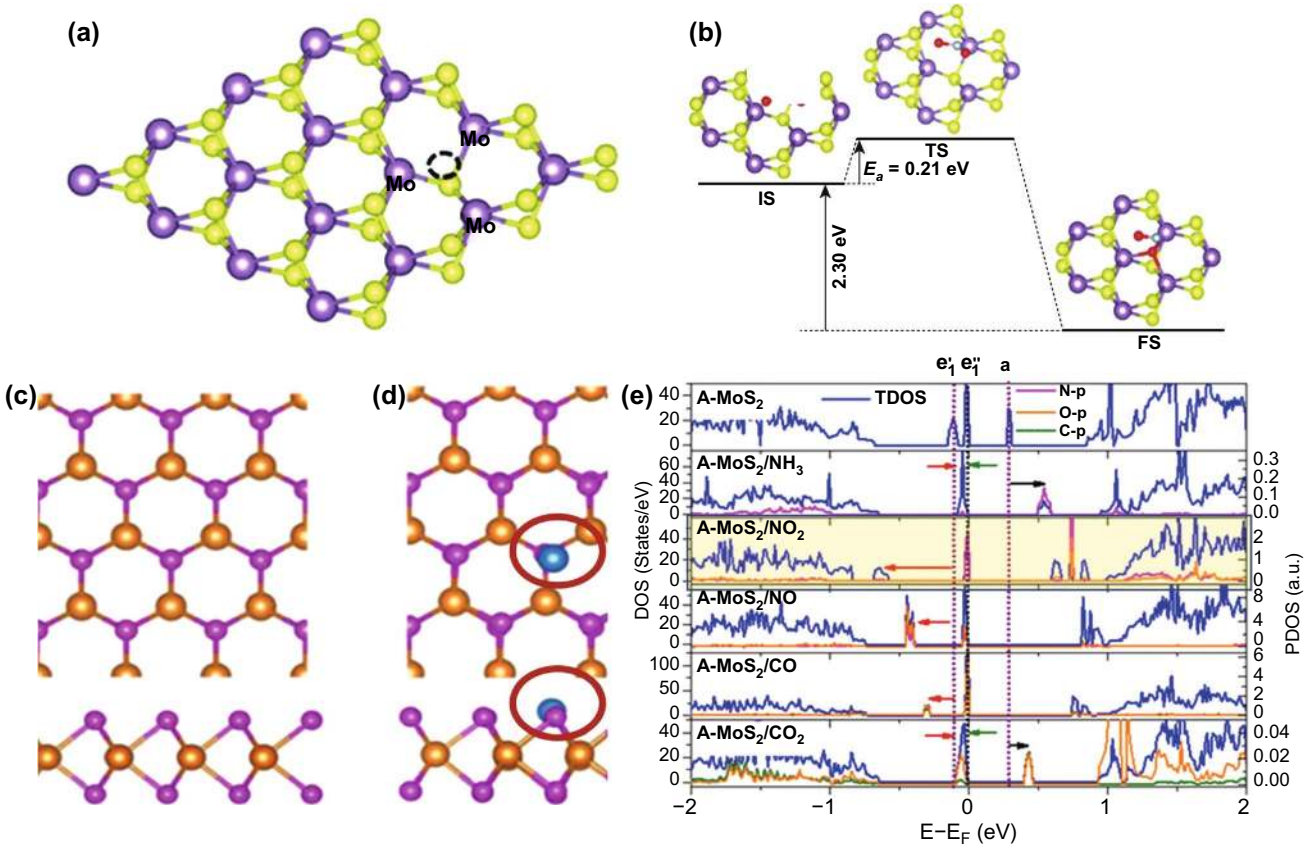

Fig. 6 **a** Structure of defected MoS_2. Black circles represent the S vacancy sites. **b** Dissociation of NO_2 onto the S vacant MoS_2. Mo_S. Reproduced with permission from Ref. [281]. Copyright (2016) The Royal society of chemistry. **c** Top view of pristine MoS_2 **d** Mo-doped S Antisite defects (Mo_S) **e** DOS and PDOS of monolayer MoS_2 with Antisite defect-doped MoS_2 with gas molecules exposure. Reproduced with permission from Ref. [285]. Copyright (2016) American Chemical Society

responsible for high charge transfer and strong adsorption energy. The p orbitals of N and O atom of NO_2 molecules are strongly hybridize with the three new mid gap states generated due to the antisites Mo_S defects. The DOS and PDOS states of A-MoS_2 confirmed this behavior. The strong hybridization occurred between the NO_2 molecule and with three new mid gap states which enhanced the charge transfer.

4.2 Adsorption of NO_2 Gas Molecules on 2H-MoS_2 and 1T-MoS_2 Polytype

The two polytype of MoS_2, 2H-MoS_2, and 1T-MoS_2 have their own advantages in NO_2 sensing. Both polytypes have distinct electronic nature of semiconductors (2H-MoS_2) and metallic (1T-MoS_2). Here, in this section, we will enlighten the role of both pristine phases and defective phases MoS_2 in NO_2 sensing. Linghu et al. has compared the NO_2 sensing performance of pristine 2H-MoS_2 and pristine 1T-MoS_2 [286]. The 1T-MoS_2 has shown promising sensing performances in comparison to the 2H-MoS_2. The geometric optimization revealed that NO_2 has a closer and stronger interaction with the 1T-MoS_2 phase than the 2H-MoS_2. The calculated adsorption energies for the 2H-MoS_2 and 1T-MoS_2 phases are -0.21 eV and −0.25 eV, respectively, reasonable to assume the higher NO_2 interaction with the 1T phase. The higher adsorption energy comparative to 2H -MoS_2 confirmed the higher and closer interaction in 1T MoS_2.

Taking a step further, Linghu et al. studied the role of defects in both 2H and 1T polytype and found again that defective 1T-MoS_2 is superior in NO_2 adsorption [287]. The single S vacancy defects are considered in both phases due to their low formation energy requirement.

Figure 7a, b demonstrates the geometric perspective structure with S vacancy of 2H and 1T MoS_2. The S

vacancies in both 2H and 1T phase affect the electronic structure of the MoS_2. S vacancies introduced mid gaps states and further reduced the MoS_2 bandgap. Moreover, the metallic behavior of 1T-MoS_2 is increased due to these mid gap states. The band structure of 2H and 1T MoS_2 of pristine and defective MoS_2 are shown in Fig. 7c–f. When NO_2 is exposed to these polytypes, it dissociates in NO and O, as shown in Fig. 7g, h. The O atom tri-coordinated with the neighboring three Mo atom and occupied the S vacancy site and NO gets physisorbed on MoS_2. The variation of adsorption energy with different molecules is shown in Fig. 7i. The red encircled values depict the NO_2 adsorption energies.

4.3 *Theoretical Adsorption of NO_2 Gas Molecules on Metal-Functionalized MoS_2*

The absence of dangling bonds makes the pristine monolayer MoS_2 surface defects free. However, the defects are highly probable and S vacancies are the most favorable defect due to the less energy required for their formation [102, 288–290]. There are various experimental reports in which S defects have been controlled by using the argon and electron irradiation. Filling these mono vacancy sites with substitutional atoms can be a promising way to enhance the chemical, electrical and optical properties of MoS_2 layers [289, 291]. These vacancy sites have been filled with various metal atoms such as Cr, Nb, V, and N, experimentally and the electronic and chemical activities of MoS_2 layers changed dramatically [291–293]. Yuan et al. doped graphene with Al, Si, Cr, and Mn and studied the oxygen adsorption on the metal-doped graphene using DFT. The metal doping tuned the adsorption interaction of oxygen with carbon atoms of graphene. The bonding of the metal atom with the carbon atom is a responsible factor for enhance oxygen adsorption on the doped graphene [294]. Lu et al. embedded the graphene with Au and investigated the CO oxidation using DFT [295]. Au embedding reduces the reaction barrier and increases the oxidation rate of the CO on Au embedded graphene. Similarly, the inert 2D materials surface can be changed to a highly active surface for gas interaction due to the bonding of 2D materials with metal atoms.

Therefore, metal doping has a great impact on the electronic and gas-sensing properties such as adsorption energy, charge transfer, the direction of charge transfer and interaction of gas molecules with the MoS_2 surface. The choice of appropriate metal for a particular gas will strongly modulate the chemical activity, selectivity and sensor response of the MoS_2 surface.

Fan et al. investigated the effect of transition metals (Fe, Co, Ni, Cu, Ag, Au, Rh, Pd, Pt, and Ir) doping on MoS_2 flakes for various gas molecules adsorption (CO, NO, O_2, NO_2, and NH_3). The effect of transition metal doping in the absence of the gas molecules has been systematically studied. All the mentioned metals have been doped on the mono-sulfur vacancy site due to the low formation energy of S vacancies in comparison to other vacancies such as Mo vacancy, dia Mo vacancy and antisite vacancies [102, 288–290]. The equilibrium height (M-Mo) is taken from the metal atom and S atom plane. The stability of the metal embedded MoS_2 in terms of binding energy and charge transfer was tested to have a better grasp. The binding energy (E_b) between the metal atom and unexposed MoS_2 is calculated by Eq. (5):

$$E_b = E_{MoS_2} + E_{metal} - E_{MoS_2+metal} \quad (5)$$

The highest binding energy (energy required to bind the metal atom on the S vacant MoS_2) was found 5.21 eV for Pt metal atoms and the lowest for 1.98 eV for the Ag atoms. The maximum charge 0.36e was transferred from Fe metal to MoS_2 and the lowest − 0.34e to Pt metal atom from MoS_2. The negative charge value means transition metals obtain the electrons from the MoS_2 and vice versa for positive charge value. The binding energy and charge transfer values mentioned above are without NO_2 exposure. The charge depletion and accumulation between the metals and MoS_2 are due to the Pauling electronegativity. For the case of NO_2 adsorption on the metal-doped MoS_2 sheet, two different modes were obtained after the relaxation of the exposed MoS_2 system. One mode is with Fe, Co, Cu, Ag, and Au embedded MoS_2 system via bonding of two O atoms with transition metals forming TM–O–N–O (four membered ring). The other mode is the bonding of NO_2 with Ni-, Rh-, Pd-, Pt-, and Ir-doped MoS_2 in which N-atom bonded with the transition metal. The adsorption energies and charge transfer in case of NO_2 adsorbed on the metal-doped MoS_2 are tabulated in

 https://doi.org/10.1007/s40820-020-00558-3

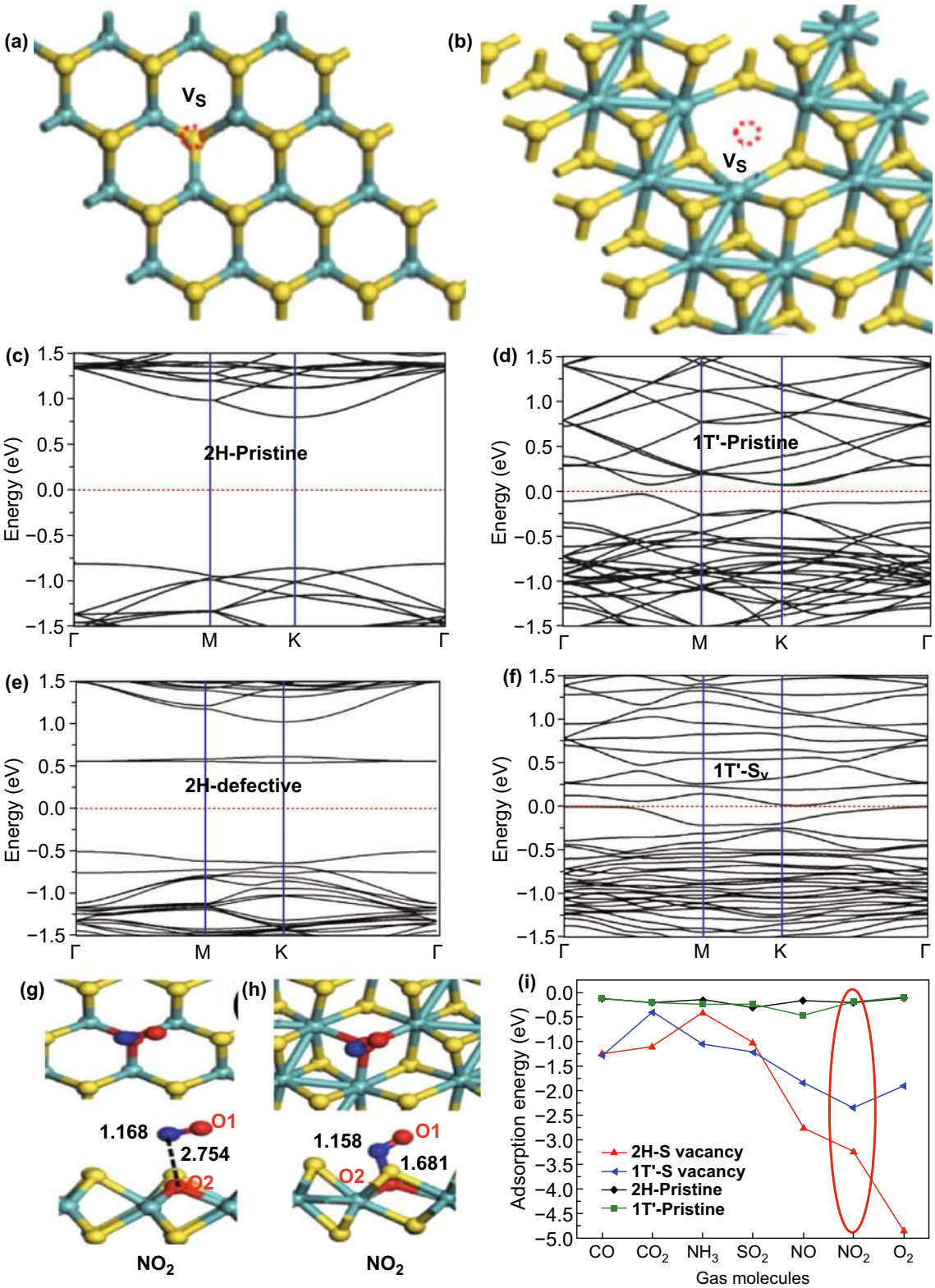

Fig. 7 **a** S vacancy in 2H-MoS_2. **b** S vacancy in 1T-MoS_2. Band structure of **c** pristine 2H-MoS_2, **d** pristine 1T-MoS_2, **e** S vacant 2H-MoS_2, **f** S vacant 1T-MoS_2. Adsorption of NO_2 on **g** defective 2H-MoS_2, **h** defective 1T-MoS_2. **i** Variation of adsorption energy for different molecules. Reproduced from Ref. [286]. Copyright (2019) American Chemical Society

Table 2. Fan et al. calculated the adsorption energy of gas molecules by Eq. (6):

$$E_a = E_{\text{free molecule}} + E_{\text{free sheet}} - E_{\text{adsorbed sheet}} \quad (6)$$

The Fe metal-embedded MoS_2 has shown promising NO_2 adsorption properties with charge transfer value − 0.66e and adsorption energies of 210 meV. The negative values indicate that charge transferred from metal embedded MoS_2 to NO_2 than pristine MoS_2. These extra electrons are obtained from the embedded transition metals, which reflect the importance of the transition metals. The electronic structure with NO_2 and metal embedded MoS_2 was studied deeply. The higher interaction of NO_2 is due to the mixing of Fe 3d states and 6a1, 1a2, and 4b1 orbitals of NO_2 over a wide range of energy, as shown in the Fig. 8a, b. These mixing or hybridization resulted in enhanced NO_2 interaction with charge transfer of − 0.66e. A similar behavior is observed with other metal-doped MoS_2.

Luo et al. doped Al, Si, and P metal atoms at the S vacancy site [297]. These metals were chosen because of their exactness and closeness of covalent radii to the radius of the S atom. The NO_2 and NH_3 adsorption were studied at five adsorption sites on MoS_2. The five adsorption sites are T_x (gas molecule on top of doped metal), H_x (gas molecule on top of hexagon near to doped metal), T_S (gas molecule on top of S atom near to doped metal), T_{Mo} (gas molecule on top Mo atom near to doped metal). Among all five sites, the most stable site for NO_2 adsorption was H_x after a complete structure relaxation. The doping of Al, Si, and P generates impurities in the Mo 4d state which create strong hybridization coupling between the Al-3p, Si-3p, and P-3p. Therefore a strong charge is transferred between the atoms and monolayer MoS_2. Si-doped MoS_2 was found most suitable for NO_2 adsorption due to the highest charge transfer between them. PDOS calculation was performed to investigate the NO_2 adsorption on undoped MoS_2 and doped MoS_2, and

Table 2 Summary of the adsorption energy, charge transfer, and method utilized for the calculating the NO_2 adsorption on the various metal-doped

Metal	Supercell Size (lattice parameter in Å)	Method	E_{ads} (eV)	Charge transfer (e)	References
Fe	4×4 (3.18) $E_a = E_{\text{free molecule}} + E_{\text{free sheet}} - E_{\text{adsorbed sheet}}$	PBE*	1.92	− 0.66	[296]
Co			1.45	− 0.61	
Ni			0.84	− 0.42	
Cu			1.02	− 0.64	
Ag			0.54	0.60	
Au			0.65	− 0.54	
Rh			1.13	− 0.31	
Pd			0.29	− 0.34	
Pt			0.37	− 0.34	
Ir			1.49	− 0.39	
MoS_2	4×4 (3.17) $E_a = E_{MoS_2+\text{molecule}} - (E_{MoS_2} + E_{\text{molecule}})$	PBE	− 0.07	− 0.02	[297]
Al			− 3.02	− 0.50	
Si			− 2.58	− 0.52	
P			− 2.134	− 0.48	
V	4×4 (3.17) $E_a = E_{\text{free molecule}} + E_{\text{free sheet}} - E_{\text{adsorbed sheet}}$	PBE	2.59	− 0.66	[298]
Nb			3.88	− 0.69	
Ta			3.64	− 0.72	
Ag	4×4 (3.18) $E_a = E_{MoS_2+\text{molecule}} - (E_{MoS_2} + E_{\text{molecule}})$	PBE	− 2.83	− 0.61	[299]
Cu	5×5 (3.18) $E_a = E_{\text{free molecule}} + E_{\text{free sheet}} - E_{\text{adsorbed sheet}}$	PBE	1.66	0.64	[25]

*Perdew–Bruke–Ernzerh (PBE); The negative value means charge transfers from MoS_2 to gas molecules; the doping site is at S vacancies for all the reports

https://doi.org/10.1007/s40820-020-00558-3

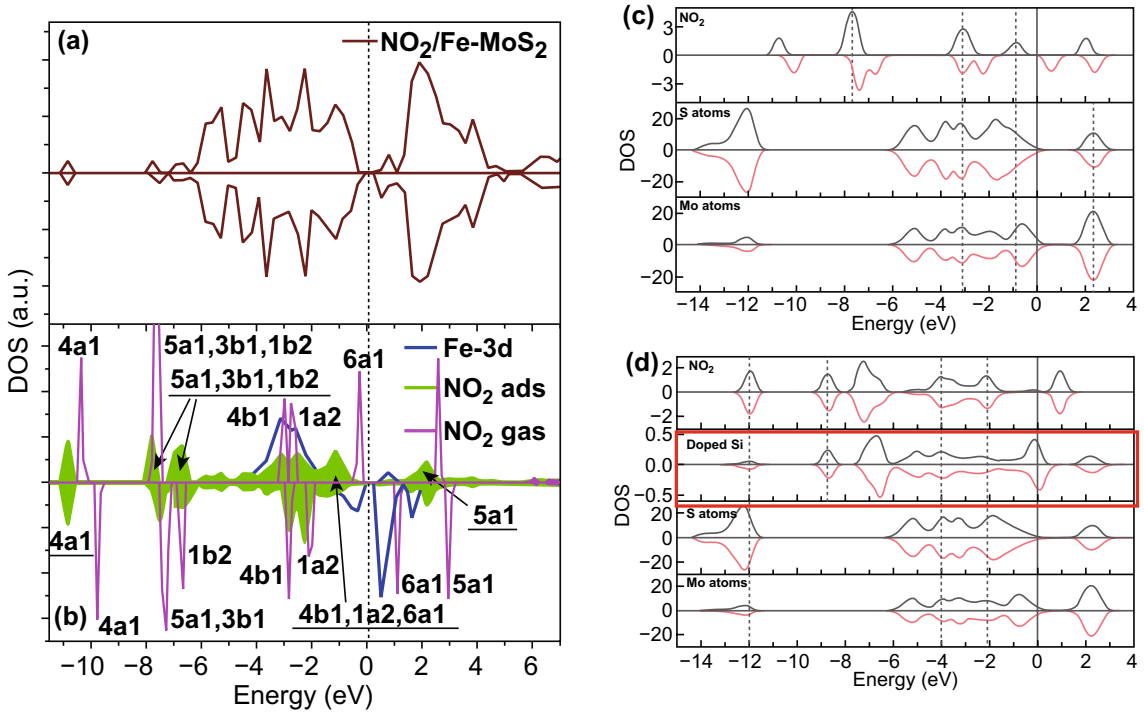

Fig. 8 **a, b** Total density of states and density of states for Fe-embedded NO_2 molecule. Reproduced with permission from Ref. [296]. Copyright (2017) Elsevier; Calculated projected density of states **c** with NO_2 adsorbed on monolayer MoS_2, **d** Si-doped MoS_2. Reproduced with permission from Ref. [297]. Copyright (2016) Elsevier

shown in Fig. 8c, d. In the case of undoped MoS_2, the NO_2 peaks were situated at − 7.7 and − 3.09 eV while the PDOS peak of bare MoS_2 was situated at 2.33, − 12.04 and between − 1.5 and − 5 eV. Hence the weak interaction occurs between NO_2 and MoS_2. However, when Al was doped in MoS_2, there is more orbital coupling at − 1.35 and − 3.31 eV not only with Al orbitals but also with S and Mo orbitals. Hence, the interaction and charge transfer increased with Al doping. NO_2 molecules partially obtained electrons from the doped Al. With Si atom, the hybridization of orbitals is further increased and a higher number of electrons, i.e., 0.52e transfer to MoS_2. Similar behavior was observed with the P atom.

Zhu et al. studied the doping of V, Tb, and Ta on the S vacancy site [298]. It is important to note that the size of these metal atoms is large in comparison to the S atom. These atoms are thus situated outside the S plane. Among all, the high binding energy suggested that Ta atoms bound firmly with MoS_2. The NO_2 gas molecules prefer to make bond on metal atoms. The two oxygen atoms form bond with the metal atom and N atom, and form a four-membered ring like structure M–O–N–O, shown in Fig. 9a–c. The calculated adsorption energies were 2.59, 3.88, and 3.64 eV for V, Nb, and Ta atoms, respectively. The Bader charge analysis revealed that charge transferred from MoS_2 to NO_2 and with V, Nb, and Ta atoms metals doping. NO_2 has shown strong oxidizing behavior. The charge density differences are shown in Fig. 9d–f. The NO_2 adsorption with monolayer MoS_2 were further calculated with NO_2 exposure.

However, the charge transfer and adsorption energies are comparatively smaller than metal-doped V, Nb, and Ta. Moreover, NO_2 as a paramagnetic molecule is critically affected by the bond length [300]. The bond length was 1.21 Å in the case of pristine MoS_2 while NO_2 bond length was elongated from 0.07 to − 0.11 Å with metal-doped MoS_2. Thus, the NO_2 activation on metal-doped MoS_2 is enhanced. Further electronic properties of MoS_2 after NO_2 doping was analyzed in terms of DOS, shown in Fig. 9g–i. The metal orbitals and NO_2 orbitals have a strong hybridization between their orbitals. The d orbitals of metals especially for Nb atoms get mixed with NO_2 orbitals over a wide range of energy. Hence, doping of MoS_2 with V, Nb, and Ta improves the electronic and chemical performance of the NO_2 molecule. The supercell

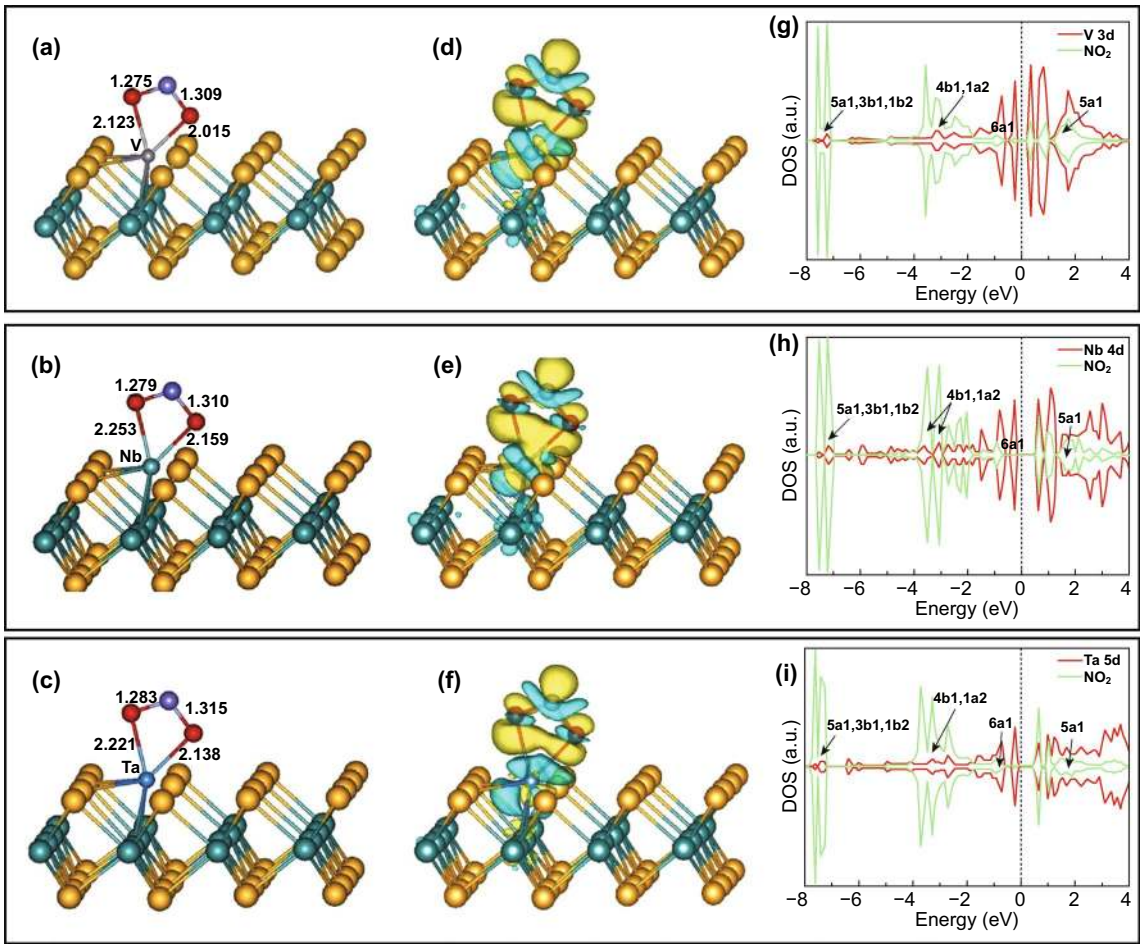

Fig. 9 **a, d, g** NO_2 molecule adsorbed on V metal: optimized geometry after NO_2 adsorption (**a**), charge density difference (**d**), spin-polarized density of state with V 3d and NO_2 (**g**). **b, e, h** NO_2 molecule adsorbed on Nb metal: optimized geometry after NO_2 adsorption (**b**), charge density difference (**e**), spin-polarized density of state with Nb 4d and NO_2 (**h**). **c, f, i** NO_2 molecule adsorbed on Ta metal: optimized geometry after NO_2 adsorption (**c**), charge density difference (**f**), spin-polarized density of state with Ta 5d and NO_2 (**i**). Reproduced with permission from Ref. [298]. Copyright (2017) Elsevier

size, lattice parameter, occupied method, adsorption energy, and charge transfer are summarized in Table 2.

5 Experimental Investigations of NO_2 Adsorption on MoS_2

In this section, we discuss various experimental approaches employed to develop the NO_2 sensors. This section has been divided into five sub-section in which we summarize the various experimental approaches adopted in terms of bare MoS_2, morphology-driven MoS_2, metal-doped MoS_2, vacancy-driven MoS_2, and finally light-assisted MoS_2-based NO_2 sensors.

5.1 Bare MoS_2 NO_2 Sensor

Here, we addressed several efforts and experimental reports where NO_2 sensors were fabricated with single and multilayered MoS_2 flakes. The reports include the impact of NO_2 adsorption on the single and multilayer MoS_2 and as well as the on the SBH. Li et al. developed the first NO_x gas sensor using an n-type MoS_2 flakes-based FET device [34]. The schematic of fabricated device is shown in Fig. 10a. The monolayer (1L) to quadrilayer (4L) MoS_2 flakes were synthesized by the mechanical exfoliation technique and had the detection limit of 0.8 ppm. The thickness of the MoS_2 layers was confirmed by the atomic force microscopy (AFM) technique. The current versus voltage

 https://doi.org/10.1007/s40820-020-00558-3

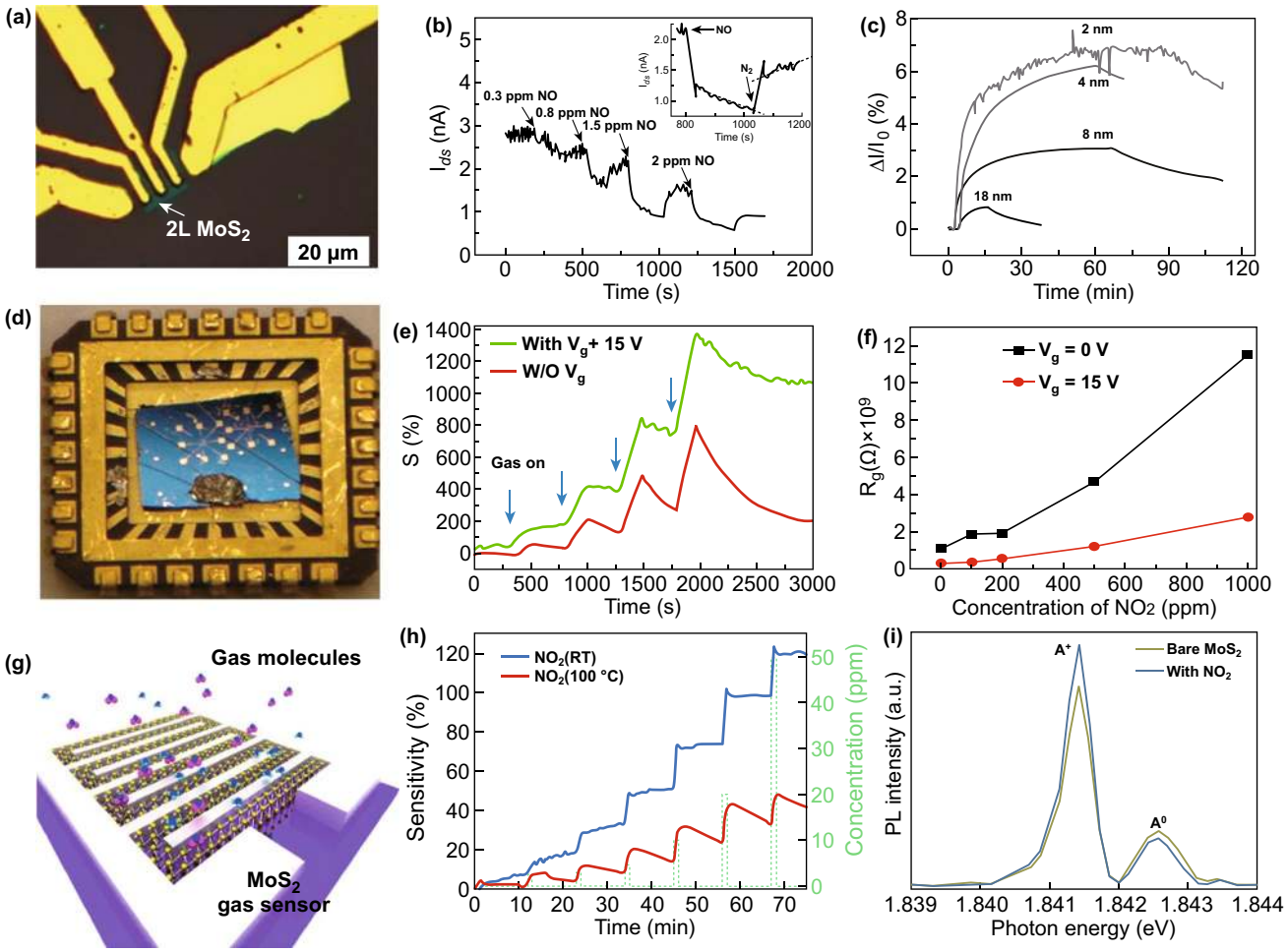

Fig. 10 **a** Optical image of bilayer MoS_2-based FET NO sensor. **b** MoS_2 FET response to different concentrations NO. The inset showed the typical response and recovery of the MoS_2 FET device. Reproduced with permission from Ref. [34]. Copyright (2012) Wiley-VCH. **c** MoS_2 TFT NO_2 sensor with different thickness MoS_2 flakes. Reproduced with permission from Ref. [42]. Copyright (2012) Wiley-VCH; **d** optical image of MoS_2 device mounted on a chip. **e** NO_2 response for the bi and five-layer MoS_2 devices at different gate voltages. **f** Theoretically calculated resistance variation with different gate voltages. Reproduced with permission from Ref. [17]. Copyright (2013) American Chemical Society. **g** Device schematic of atomic layer MoS_2-based sensing device. **h** Response of NO_2 at RT and at moderate temperature of 100 °C. **i** Change in the low energy PL peak due to NO_2 adsorption. Reproduced with permission from Ref. [32]. Copyright (2015) Springer Nature

characteristics measurements of the device with varied layers were performed. The single layer device showed unstable behavior while bi- to quadrilayer film-based devices demonstrated better sensing performance. The NO gas exposure to bilayer MoS_2 film showed a decrease in the current, which confirm the p-type doping due to the electron acceptor nature of the NO gas [57, 301]. Figure 10b displays the gas-sensing performance of the MoS_2 device with different NO concentrations. The adsorption and desorption rate of NO was a two-step process: fast rate and slower rate. The fast reduction in current confirmed the presence of a large number of NO adsorption sites and slow reduction confirmed saturation of MoS_2 film in NO exposure. Another significant aspect of the different thickness of MoS_2 film was the quick response to NO exposure. The single layer MoS_2 film showed a 50% response within 5 s while multilayer MoS_2 showed a 50% response in 30 s. However, the disadvantage with single-layer MoS_2 film was its instability.

He et al. developed a flexible MoS_2 thin film transistor (TFT) arrays for the NO_2 sensing [42]. The single layer MoS_2 film suspension was drop cast over patterned rGO electrodes covered with Ag pads. The Ag pads had only been used to improve the robustness of the rGO electrodes.

The MoS_2 area and thickness for NO_2 sensing were 1.5 mm^2 and 2, 4, 8, and 18 nm, respectively. It is worth to note that the deposited MoS_2 film showed p-type behavior attributing to the structural changes caused by the lithium intercalation process. The structural changes in the MoS_2 lead to a change in the band structures. During distortion from the octahedral system to zigzag chain, the system was filled up to d^{2+n} states. Hence, residual negative charges semi filled the bands and contributed to p-type conductivity [302]. The NO_2 gas exposed to the various thickness of MoS_2 film and the highest change in the sensor response was occurred for the thinnest MoS_2 film. The NO_2 exposure increased the conductance of the film due to its electron acceptor nature. The high NO_2 detection ability of thin MoS_2 film was attributed to the increased surface area available in 2 nm film. The sensor response of different thickness of MoS_2 film is shown in Fig. 10c. Late et al. studied the NO_2 sensing behavior of single and multiple layer MoS_2 film synthesized by the mechanical exfoliation method [17]. A detailed gas-sensing performance with and without applying the bias voltage was presented. A detailed AFM, Raman, and TEM characterization were performed to understand the thickness, expansion, crystallographic orientation, and structure of MoS_2. The device schematic with Ti/Au contact is shown in Fig. 10d. The *I–V* characteristic of single layer MoS_2 device was unstable while multilayer MoS_2 showed stable *I–V* characteristics. Few layers (single and five layers) MoS_2 device demonstrated good behavior. The three and four-layer MoS_2 flakes device showed identical behavior to two layer and five-layer devices. The NO_2 sensing for five-layer MoS_2 device is shown in Fig. 10e. However, this higher performance was due to the redox potential that greatly influences the sensing behavior of MoS_2 flakes. Once again, the NO_2 interaction with MoS_2 revealed that the NO_2 has an electron acceptor nature. The influence of the external electric field in terms of bias voltage on the NO_2 sensing was further studied. When a positive back gate biasing voltage + 15 V was applied to two and five layers of MoS_2 flakes, the sensor response was improved in comparison to zero bias voltage. A larger number of electrons were collected at the MoS_2 and SiO_2 interface under positive back gate voltage. Therefore, NO_2 has a higher number of electrons to detach from the MoS_2. With positive gate biasing voltage, the NO_2 sensor response was thus increased. In addition, Ti/Au electrode played a vital role under positive gate voltage. Under positive gate voltage, electrons get accumulated in MoS_2 film and the barrier between the electrode and MoS_2 film is reduced. Thus, the charge transfer in MoS_2 film facilitated further. The device resistance in the presence of NO_2 gas is shown in Fig. 10f at different biasing voltages.

Cho et al. synthesized the atomic layered MoS_2 flakes by the CVD technique and performed the NO_2 gas sensing [32]. The resistance of the n-type MoS_2 film increased due to the electron-accepting nature of NO_2. The interdigitated electrodes of Ag metal were fabricated on the MoS_2 film. The NO_2 sensing performance was studied at RT and at a moderate temperature of 100 °C.

The device schematic and NO_2 sensor response versus time profile at each temperature are shown in Fig. 10g, h. It can be seen clearly that the RT sensor response was quite high in comparison to 100 °C, while the sensor showed rapid recovery at 100 °C and no recovery was obtained at RT. The NO_2 gas strongly adsorbed on MoS_2 and hence at RT the desorption rate is quite low. However, thermal energy greatly impacts the adsorption of NO_2 at a higher temperature. The thermal energy accelerates the NO_2 desorption rate than the adsorption rate. As a result, the NO_2 gas interaction decreases at a higher temperature at the sensor response cost. The NO_2 sensing mechanism based on the charge transfer process, confirmed by the change in the peaks of PL spectra is shown by Fig. 10i, as we discussed in Fig. 5b of Sect. 3.

These all layer-dependent studies show that the single layer MoS_2-based gas sensors suffered from unstable current, but they have a quick response with NO_2 exposure. The few layer MoS_2 flakes-based gas sensors show a good response with the stable current. Moreover, the MoS_2 FET gas sensors are very sensitive to the applied bias voltage. However, the MoS_2 gas sensors have an incomplete recovery at RT. So, operating sensors at a higher temperature may be a good option to achieve full recovery but it will reduce the sensor response. The summary of the results for bare MoS_2-based NO_2 gas sensors by various groups are tabulated in Table 3.

Liu et al. studied the NO_2 sensing efficiency of monolayer MoS_2 flakes grown by CVD [36, 303]. The effect of gas molecules adsorption on the Schottky barrier height (SBH) between the MoS_2 and metal electrodes was studied. The sensing device area was 1 μm^2 and film showed the 3 $cm^2\ V^{-1}\ s^{-1}$ mobility with Ti/Au electrodes, shown in Fig. 11a. The Ti was used for improving the electrode adhesion with MoS_2 film. The device showed highly rectifying behavior with a positive and negative drain to source voltage

 https://doi.org/10.1007/s40820-020-00558-3

Table 3 Summary of the reported NO_2 sensor based on the MoS_2

Sensing film	Type	Method	Def.	Electrodes	Device	Conc. (ppm)	Tem. (°C)	S (%)	Res time	Rec time	References
1L MoS_2	n	M.E.	$\left(\frac{(I_{gas}-I_{air})}{I_{air}}\right)$	Ti/Au	FET	2	RT	80	–	–	[34]
MoS_2 sheets	p	E.L.	$\left(\frac{(R_{gas}-R_{air})}{R_{air}}\right)$	rGO	TFT	1.2	RT	7	–	–	[42]
5L MoS_2	n	M.E.	$\left(\frac{(R_{gas}-R_{air})}{R_{air}}\right)$	Ti/Au	FET	1000	RT	1372	300	600	[17]
1L MoS_2	n	CVD	$\left(\frac{(G_{gas}-G_{air})}{G_{air}}\right)$	Ti/Au	FET	.02	RT	> 20	300	–	[36]
3L MoS_2	p	CVD	$\left(\frac{(I_{gas}-I_{air})}{I_{air}}\right)$	Al	Resistor	10	RT	80	–	–	[303]
2L MoS_2	p	CVD	$\left(\frac{(I_{gas}-I_{air})}{I_{air}}\right)$	Ag	Resistor	10	RT	98	–	–	[303]
4L MoS_2	p	CVD	$\left(\frac{(I_{gas}-I_{air})}{I_{air}}\right)$	Au	Resistor	10	RT	60	–	–	[303]
Atomic layered MoS_2	n	CVD	$\left(\frac{(R_{gas}-R_{air})}{R_{air}}\right)$	Ag	Resistor	50	RT	~ 120	–	–	[32]
Atomic layered MoS_2	n	CVD	$\left(\frac{(R_{gas}-R_{air})}{R_{air}}\right)$	Ag	Resistor	50	100	> 40	–	–	[32]
Few layer MoS_2	p	L.E.	$\frac{R_{gas}}{R_{air}}$	Pt	Resistor	1	200	1.15	660	720	[31]
Few layer MoS_2	n	L.E.	$\frac{R_{gas}}{R_{air}}$	Pt	Resistor	1	200	5.80	2460	2340	[31]
Vertical MoS_2	p	CVD	$\left(\frac{(R_{gas}-R_{air})}{R_{air}}\right)$	Ti/Au	Resistor	100	RT	> 10	–	–	[35]
Vertical MoS_2	n	CVD	$\left(\frac{(R_{gas}-R_{air})}{R_{air}}\right)$	Au/Cr	Resistor	50	RT	48.32	98	–	[304]
Vertical MoS_2	n	CVD	$\left(\frac{(R_{gas}-R_{air})}{R_{air}}\right)$	Au/Cr	Resistor	50	RT	24.26	34	132	[304]
2L MoS_2	p	CVD	$\left(\frac{(R_{gas}-R_{air})}{R_{air}}\right)$	Au	Resistor	1	RT	2.6	678	318	[305]
Mixed MoS_2	p	CVD	$\left(\frac{(R_{gas}-R_{air})}{R_{air}}\right)$	Au/Cr	Resistor	10	RT	10.36	8.51	–	[120]
Mixed MoS_2	p	CVD	$\left(\frac{(R_{gas}-R_{air})}{R_{air}}\right)$	Au/Cr	Resistor	10	125	7.79	4.44	19.6	[120]
MoS_2 NWs	n	CVD	$\left(\frac{(R_{air}-R_{gas})}{R_{air}}\right)$	Au	Resistor	5	60	18.1	16	172	[214]
MoS_2 nanoflower	p	Hyd.	$\frac{R_{gas}}{R_{air}}$	Au	Resistor	50	150	78	–	–	[33]
MoS_2 nanosphere/CTAB	n	Hyd.	$\left(\frac{(R_{air}-R_{gas})}{R_{air}}\right)$	Ag/Pd	Resistor	50	150	60	15	12	[306]

Table 3 (continued)

Sensing film	Type	Method	Def.	Electrodes	Device	Conc. (ppm)	Tem. (°C)	S (%)	Res time	Rec time	References
MoS_2 hollow microsphere	p	Hyd.	$\left(\frac{(R_{air}-R_{gas})}{R_{air}}\right)$	Au/Cr	Resistor	100	150	40.3	79	225	[307]
MoS_2 Nanoflowers	p	Hyd.	$\left(\frac{(R_{air}-R_{gas})}{R_{air}}\right)$	Pt	Resistor	5	RT	67.4	125	485	[308]
MoS_2 Nanoflowers	p	Hyd.	$\left(\frac{(R_{air}-R_{gas})}{R_{air}}\right)$	Pt	Resistor	5	150	22	95	320	[308]
MoS_2 Aerogel	p	T.D.	$\left(\frac{(R_{gas}-R_{air})}{R_{air}}\right)$	Pt/Ti	Resistor	0.5	200	11	33	107	[24]
MoS_2 Nanosheets	p	M.E.	$\frac{R_{gas}}{R_{air}}$	Ag/Pd	Resistor	100	RT	29	42	2	[309]
MoS_2-W	n	Hyd.	$\left(\frac{(R_{air}-R_{gas})}{R_{air}}\right)$	Ag/Pd	Resistor	20	RT	171	41	39	[121]
MoS_2-Au	p	S.P.	$\left(\frac{(R_{gas}-R_{air})}{R_{air}}\right)$	Au	Resistor	2.5	RT	30	240	840	[121]
rGO/Sv-MoS_2	p	CVD	$\left(\frac{(R_{gas}-R_{air})}{R_{air}}\right)$	Au	Resistor	50	50	72	56	328	[310]
MoS_2	n	CVD	$\left(\frac{(R_{gas}-R_{air})}{R_{air}}\right)$	Au	Resistor	50	50	27	142	–	[310]
Multi MoS_2	n	CVD	$\left(\frac{(R_{gas}-R_{air})}{R_{air}}\right)$	Au/Cr	Resistor	100	RT	27.92	249	–	[119]
Multi MoS_2	n	CVD	$\left(\frac{(R_{gas}-R_{air})}{R_{air}}\right)$	Au/Cr	Resistor	100	100	21.56	71	310	[119]
MoS_2-Au NPs	p	Redox	$\left(\frac{(R_{gas}-R_{air})}{R_{air}}\right)$	Au	Resistor	2.5	RT	30	240	840	[121]

Mechanical exfoliation (M.E.); liquid exfoliation (L.E.); electrochemical lithiation (E.L.); hydrothermal (Hyd.); thermal decomposition (T.D.); solution processed (S.P.)

https://doi.org/10.1007/s40820-020-00558-3

(V_{DS}) with 400 ppb NO_2 exposure, as shown in Fig. 11b. The device showed an excellent sensor response of 174% with back gate voltage 30 V. The response time was 300 to 540 s with the full recovery in 12 h. To confirm the NO_2 gas-sensing mechanism via the charge transfer process, the back gate voltage was fixed at 5 V and gas concentration was varied from 20 to 400 ppb. The threshold voltage for the NO_2 sensing received a monotonic shift in the positive V_{DS} direction. The resistance modulation in the device due to gas exposure is the sum of channel resistance ($R_{channel}$) and $R_{contact}$ determined by Eq. (7):

$$R = \left(R_{\text{channel}} \propto {}^{1}/_{n}\right) + \left(R_{\text{contact}} \propto \frac{1}{n} e^{\frac{\varphi_{SB}}{kT}}\right) \quad (7)$$

where n is the electron concentration, φ_{SB} is the Schottky barrier height between the MoS_2 and metal electrodes. The SBH is greatly influenced by the above equation when the electron concentration in the device is changed. Figure 11c, d indicates the transfer characteristics at a fixed back gate voltage of 5 V. An increment in the threshold voltage with higher gas concentration is observed. NO_2 is strong oxidizing gas and has an electron acceptor nature. More number of electrons withdraw from MoS_2 film as the gas concentration is increased. Thus, a monotonic shift in the positive V_{DS} direction was observed. Considering the effect of the NO_2 adsorption on SBH, the proposed band alignment before and after exposure to NO_2 is shown in Fig. 11e, f. NO_2 gas captured the electrons from the conduction band and the electron concentration in MoS_2 film was decreased. The decrease in electron concentration shifts the Fermi level towards the valence band which increases the SBH. Hence, the conductance is decreased.

Kim et al. recently fabricated the MoS_2 gas sensor with different metal contacts of different work functions [303]. The sensor response of the MoS_2 sensor was different with different metals. First, the effect of the layer thickness from single to four layers with Au electrodes was studied. The I–V characteristic is shown in Fig. 11h revealed a linear behavior and a decrease in resistance with an increase in layer observed. The work-function was increased with the number of layers, shown in Fig. 11g. Hence, for a higher number of layers, the SBH is decreased and according to Eq. 11, the resistance is also decreased. Further, NO_2 exposure on different thickness layer devices is also displayed in Fig. 11i. The device showed p-type behavior to NO_2 exposure. Further, the bilayer MoS_2 device showed the highest sensor response for 10 ppm NO_2 concentration up to 60%. Finally, for bilayer and trilayer MoS_2, the Au ($\emptyset_M = 5.1$ eV), Al ($\emptyset_M = 4.06$ eV), and Ag ($\emptyset_M = 4.26$ eV) electrodes were used. Among all, aluminum electrode-based sensing device showed promising sensor response, 80% for bilayer and 98% for trilayer MoS_2-based device. Conclusively, the device with lower work function metal electrodes showed better performance. The band alignment between the aluminum (lower work function metal) and MoS_2 is responsible for high performance as shown in Fig. 11l–o. The SBH is higher for Al electrodes than the Au electrodes. Under positive biasing, a higher number of holes are transferred from Au electrode due to the low SBH. When NO_2 gas is exposed, the SBH decreases with a decrease in electron depletion due to the p-type nature. Relatively, the ratio of charge transferred in Al/MoS_2 device is higher than the Au/MoS_2. Hence, better performance is observed.

These reports confirmed that sensing response is critically affected by the SBH. In chemiresistance gas sensors, the SBH is modulated with gas molecules adsorption due to charge transfer between the molecules and sensing film. Thus, Schottky contacted devices are a good candidate for fabricating gas sensors. Hence, the choice of metal contacts played an important role in gas sensing.

5.2 Morphology-Driven NO_2 Sensors

In the 2D materials, especially in MoS_2, morphology plays a vital role in determining the optical, electrical, and catalytic properties. The NO_2 molecule adsorption in MoS_2 is position-dependent and there are specific NO_2 favourable sites for molecules adsorption in MoS_2. These favourable NO_2 adsorption sites can be controlled by synthesizing various MoS_2 film surface morphology. In this section, we will discuss various reports where morphology-dependent NO_2 sensors based on MoS_2 developed.

Cho et al. studied the role of MoS_2 edges in NO_2 gas molecules adsorption [35]. The orientation of the MoS_2 film greatly affects the adsorption of NO_2 molecules. Authors varied the orientation of the MoS_2 film from horizontal to vertical align by depositing different thickness Mo films. The surface topography is shown in Fig. 12a. The inset of the Fig. 12a showed the schematic of the sensing device with an active area of 100μm^2. The NO_2 gas molecule adsorption enhanced up to fivefold in vertical aligned MoS_2 flakes

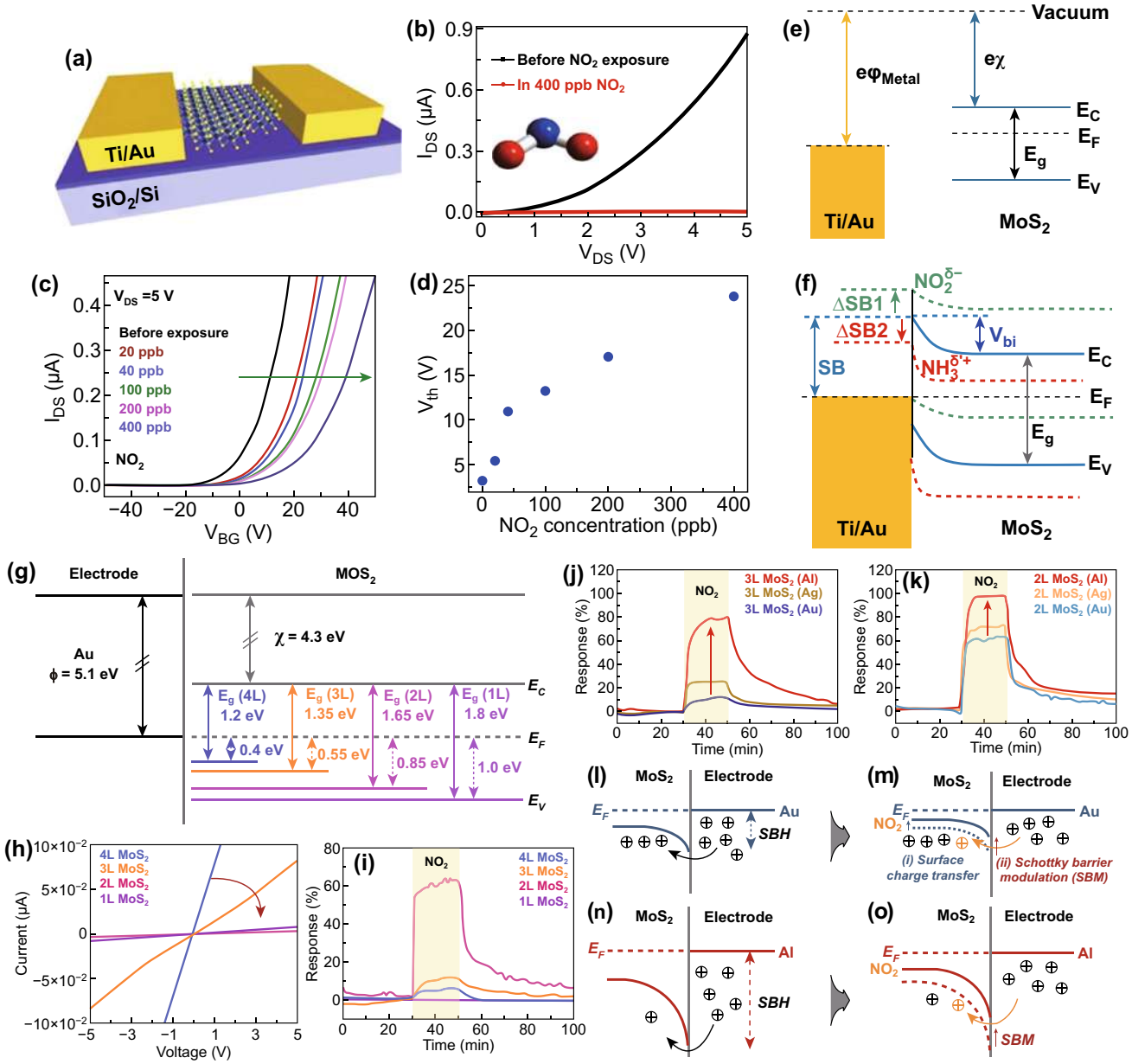

Fig. 11 **a** Schematic of the monolayer MoS_2 device. **b** Change in current after 400 ppb NO_2 exposure. **c** *I–V* characteristics after the NO_2 exposure of different concentration. **d** A monotonic shift in threshold voltage towards the positive side of applied voltage. **e, f** Energy band alignment before and after NO_2 exposure. The blue solid lines are corresponding to the band alignment of MoS_2 and Ti/Au contact in the absence of NO_2 while the green dotted lines are corresponding to NO_2 exposure. Reproduced with permission from Ref. [36]. Copyright (2014) American Chemical Society. **g** Band alignment of MoS_2 with Au metal contact. **h** Current versus voltage characteristics with gold contact. **i** NO_2 response with MOS_2-Au device. Sensor response for NO_2 with different metal contacts Al, Ag, and Au electrodes: **j** 3L MoS_2 film, **k** 2L MoS_2 film. Proposed band alignment of MoS_2-Au device: **l** before, **m** after NO_2 exposure. Proposed band alignment of MoS_2-Al device: **n** before, **o** after NO_2 exposure. Reproduced with permission from Ref. [303]. Copyright (2019) American Chemical Society. (Color figure online)

compared to the horizontal MoS_2 film, as shown in Fig. 12b. The Mo film was deposited through an electron beam evaporator and was sulfurized in the CVD. The orientation of the MoS_2 film was determined through the FESEM, XRD, TEM, and Raman spectra. The MoS_2 films (horizontal, mixed, and vertical MoS_2) showed a p-type nature. The p-type behavior was verified through the positive increase in the resistance due to the exposure of oxidizing NO_2 gas. Interestingly, vertical aligned MoS_2 flakes faced the highest change in the sensor response to the NO_2 gas, which means that

 https://doi.org/10.1007/s40820-020-00558-3

the morphology of MoS_2 flakes crucially regulates the gas-sensing behavior. The reason is the presence of numerous active sites at the edges.

As we discussed in Sect. 3, the horizontal (basal plane) and vertical aligned MoS_2 flakes have different adsorption sites (H site, T_S site, and T_M site) for NO_2 molecules with different adsorption energy and charge transfer. Moreover, the edges of vertical aligned MoS_2 flakes have high catalytic properties in comparison with the basal plane, which enhanced the NO_2 reactivity of the edges. The vertical aligned MoS_2 flakes thus displayed the great potential to communicate with NO_2. The adsorption of NO_2 on the basal plane MoS_2 and at the edges is shown in Fig. 12c.

Kumar et al. synthesized the horizontally aligned MoS_2 (HA-MoS_2) and vertically aligned (VA-MoS_2) by the CVD method [304]. The NO_2 sensing behavior for each structure was determined in the operating temperature range from RT to 150 °C. The VA-MoS_2 flakes showed better NO_2 sensing performance in all temperature range. Moreover, the VA MoS_2 film quickly detected 1 ppm NO_2 concentration. However, the sensor response for 1 ppm NO_2 concentration with HA MoS_2 flakes could not be achieved. These results revealed the high NO_2 detection ability of VA MoS_2 flakes even for the low concentration also. Another fascinating aspect of VA-MoS_2 is the sensor recovery after NO_2 exposure which didn't occur with the HA-MoS_2 flakes. The recovery of the VA and HA-MoS_2 flakes was substantially improved by operating devices at high temperatures but again at the expense of sensor response. Notably, the NO_2 selectivity of the VA-MoS_2 device was also high. The high sensor response of VA-MoS_2 flakes is due to the high adsorption sites and the higher number of charge transfer at the edges of the VA-MoS_2 flakes in comparison with HA-MoS_2 flakes.

Agrawal et al. synthesized a combination of vertical aligned MoS_2 flakes and in-plane MoS_2 flakes (mixed MoS_2 flakes) by a modified CVD technique. The surface morphology is shown in Fig. 12d. The black region is the in-plane MoS_2 flakes while the white region is the vertical MoS_2 flakes. The fabricated sensing system suggested the existence of the p-type nature of MoS_2 film. The resistance of the device was decreased with the exposure of oxidizing NO_2 gas which means there is a decrease in the electron concentration and simultaneously an increase in the hole concentrations. The transient response curve with NO_2 exposure at 125 °C is shown in Fig. 12e. The NO_2 detection at RT was also studied. However, full recovery could not be achieved. The sensing mechanism of NO_2 interaction is based on the favorable adsorption sites available on the MoS_2 flakes, shown in Fig. 12f. MoS_2 has four adsorption sites as we discussed in Sect. 3, H site, B site, T_M, and T_S site. Yue et al. theoretically showed that the H site, T_M site, and B site are the most favorable sites for the NO_2 adsorption. The maximum combination of these sites was synthesized to obtain the selective, highly responsive and recoverable NO_2 sensor.

Kumar et al. synthesized the MoS_2 nanowire through the controlled turbulent vapor flow, shown in Fig. 12g. The NO_2 sensing behavior of the n-type MoS_2 NWs was investigated at the RT, 60 °C, and 120 °C for NO_2 concentrations of 1, 2, 3, and 5 ppm, shown in Fig. 12h. The MoS_2 NWs showed a high sensor response with an incomplete recovery due to the strong bonding of NO_2 molecules with NWs. A moderate temperature of 60 °C helped the MoS_2 NWs to obtain a recovery. The MoS_2 NWs showed good response time (16 s) and recovery time (172 s) for the 5 ppm NO_2 concentration with sensor response 18% at 60 °C. The NO_2 sensing mechanism proposed in MoS_2 NWs is based on the physisorption and chemisorption of gas molecules, as shown in Fig. 12i. The humidity and environmental oxygen get adsorbed on the surface of the NWs and reduced the detection of the NO_2 gas molecule at the RT. However, at 60 °C, the humidity and adsorbed oxygen were removed and generated new active sites for the NO_2 adsorption. Hence, NO_2 detection was high at a moderate temperature. Moreover, the high temperature generates thermal energy which also helps in the recovery.

Yu et al. adopted the facile hydrothermal method and fabricated the edge-enriched flower-like MoS_2 spheres [33]. The diameter of the structure estimated through the SEM was 1–2 μm displayed in Fig. 13a. These nanospheres exhibited a large surface area with edge-enriched MoS_2 flakes. Also, the flakes were interconnected with each other and provided a quick path for the diffusion of gas molecules and charge transfer. The inset of Fig. 13a showed the high magnification FESEM image. These unique structures showed excellent sensor response, cyclability, and selectivity. The 50 ppm NO_2 concentration is discussed here. The device was operated at different operating temperatures from 100 to 250 °C, displayed in Fig. 13b. The highest sensor response for the 50 ppm NO_2 concentration was 78% at 150 °C. The resistance versus time profile is shown in the inset of Fig. 13c, confirming the p-type nature of MoS_2 due to a decrease in the resistance of the sensor device.

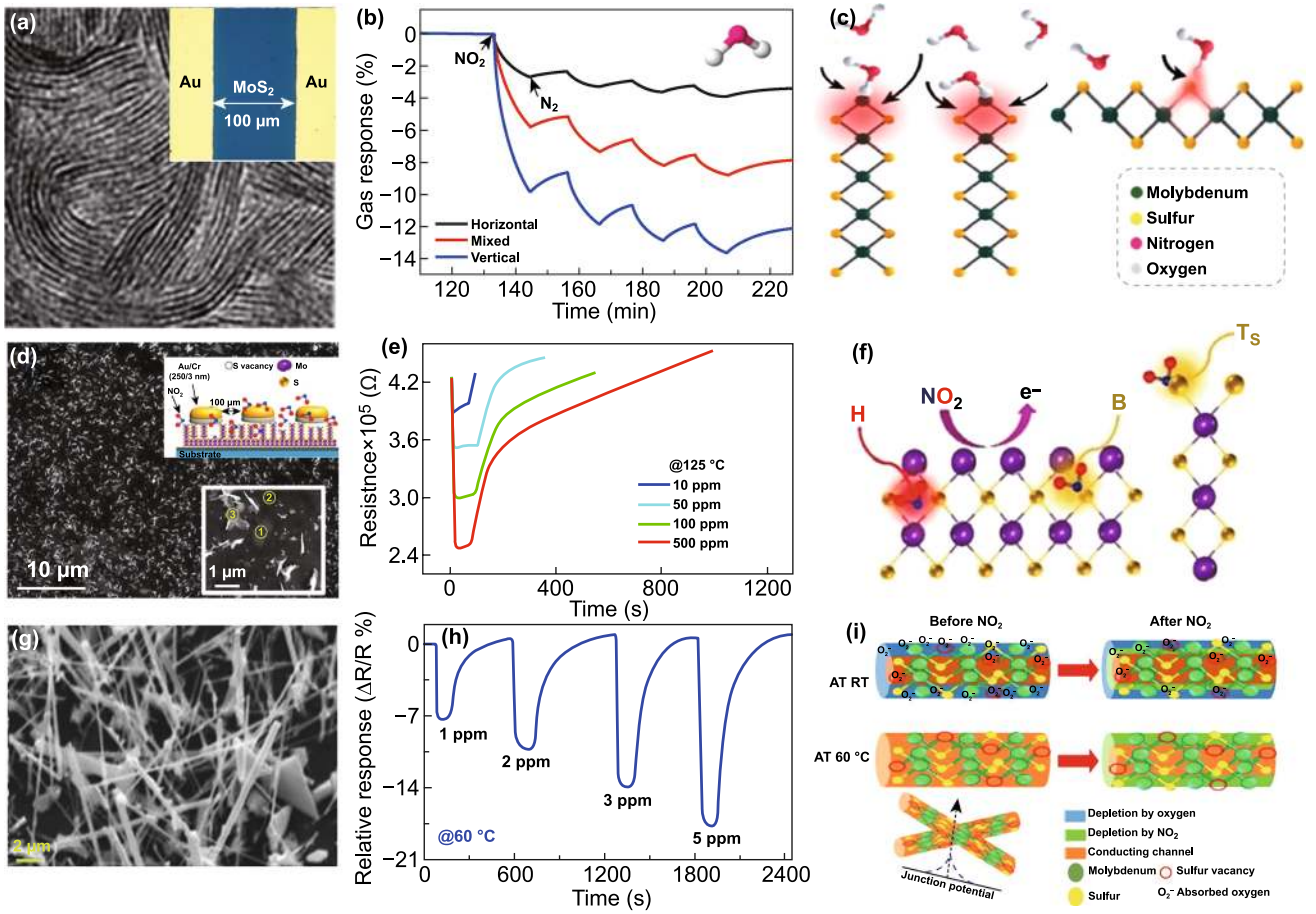

Fig. 12 **a** TEM image of the vertically grown MoS_2. **b** Response of various morphology MoS_2 flakes with NO_2 gas. **c** DFT calculated NO_2 adsorption profile on the edges and basal plane MoS_2. Edges have high adsorption of MoS_2 flakes. Reproduced with permission from Ref. [35]. Copyright (2015) American Chemical Society. **d** FESEM image of mixed MoS_2 flakes and inset showed the high-resolution image of MoS_2 flakes and the device schematic. **e** The response of mixed MoS_2 flakes with NO_2 gas at 125 °C. **f** Schematic of favorable adsorption sites on the MoS_2 flakes. Reproduced with permission from Ref. [120]. Copyright (2018) American Chemical Society. **g** FESEM image of the grown MoS_2 NWs. **h** Response of MoS_2 NWs with NO_2 exposure. **i** Proposed a mechanism of NO_2 adsorption on the MoS_2 NWs. Reproduced with permission from Ref. [214]. Copyright (2018) AIP Publishing

Zhang et al. proposed the controlled growth of 3D flower-like MoS_2 nanospheres assisted with cetyltrimethyl ammonium bromide (CTAB) [306]. CTAB played a crucial role in determining the morphology of the MoS_2 spheres. The average size of the synthesized nanospheres was 300 nm, displayed in Fig. 13d. This SEM revealed that these MoS_2 nanospheres were formed due to the bending of the randomly assembled MoS_2 sheets. These structures provide the path for the diffusion of the gas. The NO_2 sensing performance was studied in the operating temperature range from RT to 130 °C as shown in Fig. 13e. The highest reported sensor response was 60% observed for the 100 °C temperature. The MoS_2 nanospheres behaved as the n-type semiconductor. The response and recovery time profile was 15 and 12 s for 50 ppm NO_2 at 100 °C shown in Fig. 13f.

Li et al. followed a new step and prepared the hollow, solid and smooth MoS_2 nanospheres by the hydrothermal methods [307]. The hydrothermal process reaction time was maintained at 2-h, 5-h, 18-h in the presence of polyvinyl pyrrolidone (PVP) to synthesize the various morphology MoS_2 flakes. The polystyrene template (PS) spheres are the platform for the nucleation of MoS_2 nanosheets. The SEM images of a fully prepared solid sphere and hollow spheres (inset) are shown in Fig. 13g. The 500 ppm NO_2 concentration is tested in the temperature range from 25 to 250 °C. Hollow spheres have shown the remarkably high sensor response with p-type nature, as shown in Fig. 13h,

 https://doi.org/10.1007/s40820-020-00558-3

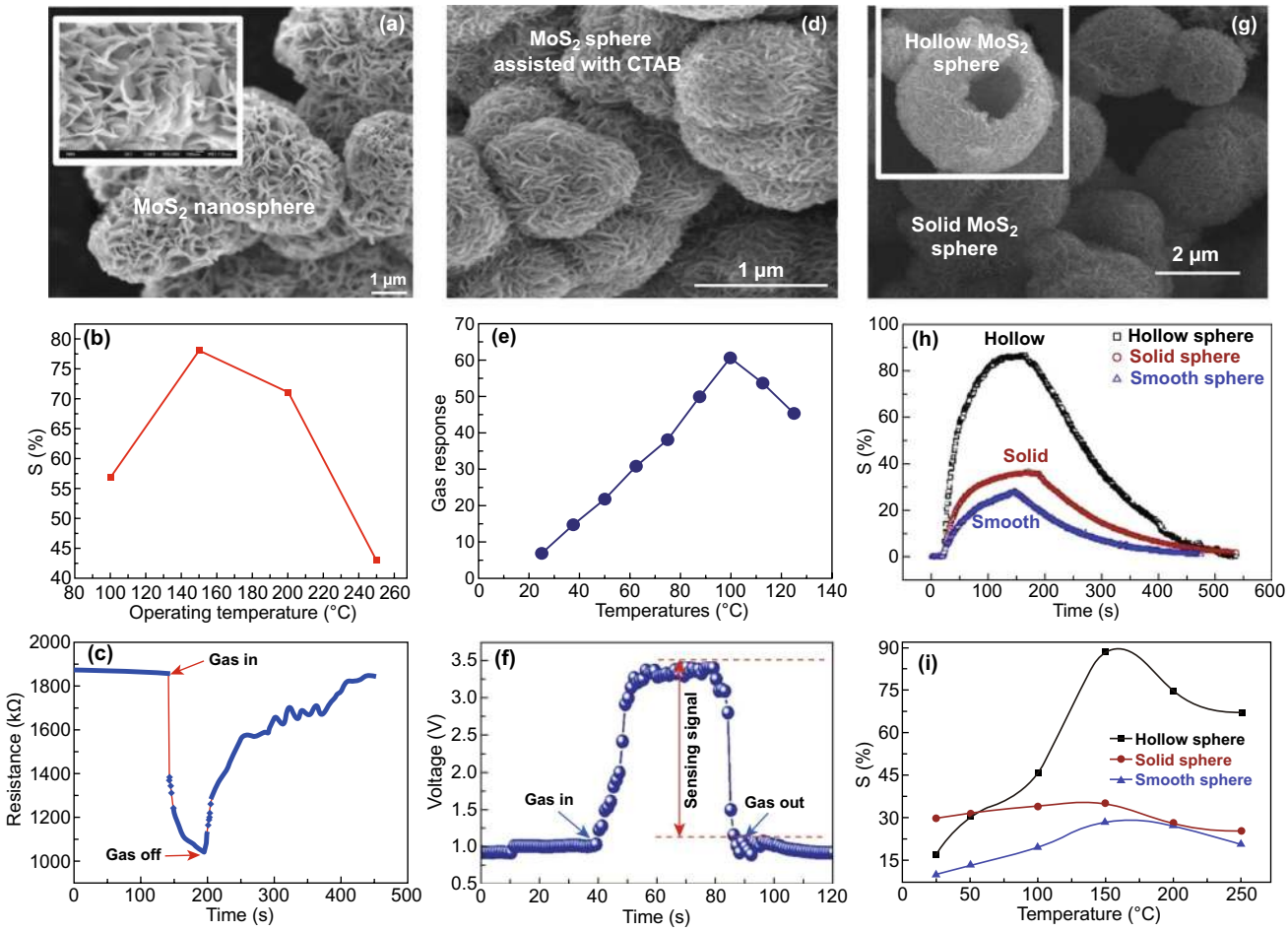

Fig. 13 **a** FESEM image of the MoS_2 nanosphere. **b** Sensor response profile. **c** Transient resistance profile. Reproduced with permission from Ref. [33]. Copyright (2016) from Elsevier. **d** FESEM image of the CTAB-assisted MoS_2 sphere. **e** Gas response obtained at different temperature range. **f** Time response profile of NO_2 sensing. Reproduced with permission from Ref. [306]. Copyright (2018) from Elsevier. **g** FESEM image of solid MoS_2 sphere and hollow sphere. **h** Obtained sensor response for hollow, solid and smooth spheres. **i** Sensor response at different temperatures. The highest sensor response obtained for the hollow spheres. Reproduced with permission from Ref. [307]. Copyright (2019) from Elsevier

i. About 2.5-fold enhancement is observed in the hollow spheres compared to solid spheres observed.

Nanospheres improved NO_2 sensing due to the large surface area of the spheres. The sensing mechanism between the MoS_2 and NO_2 is based on the transfer of charge carrier concentration between them. The oxygen gas is adsorbed on the MoS_2 and introduced p-type doping in MoS_2. When NO_2 gas exposed to MoS_2 spheres, the NO_2 accepts the electrons from MoS_2 and gets adsorbed as NO_2^- on MoS_2. Moreover, NO_2 also reacts with adsorbed O_2^- and gets adsorbed as NO_2^-. The possible reactions of adsorbed oxygen and with NO_2 are as follows [311]:

$$O_2(g) \rightarrow O_2(ads) \tag{8}$$

$$O_2(ads) + e^- \rightarrow O_2^-(ads) \tag{9}$$

$$O_2(ads) + e^- \rightarrow 2O_2^-(ads) \tag{10}$$

$$O^-(ads) + e^- \rightarrow O_2^-(ads) \tag{11}$$

$$NO_2 + e^- \rightarrow NO_2^- \tag{12}$$

$$NO_2(gas) + e^- \rightarrow NO_2^-(ads) \tag{13}$$

$$NO_2(gas) + O_2^-(ads) + 2e^- \rightarrow 2NO_2^-(ads) + 2O_2^-(ads) \quad (14)$$

$$NO_2^-(ads) + O_2^-(ads) \rightarrow 2O^-(ads) + NO_2 \quad (15)$$

The above discussion clearly shows that different MoS_2 morphologies could boost the efficiency of gas sensors such as high sensor response, speed (response and recovery time), and selectivity. By choosing the different synthesis modes such as mechanical exfoliation, chemical exfoliation and CVD techniques, various MoS_2 morphologies can be synthesized ranging from in-plane MoS_2, flower like MoS_2, MoS_2 NWs, vertical MoS_2 flakes. Different MoS_2 morphologies like vertical aligned, nanowires, solid and hollow spheres provide the path for the diffusion of gas molecules into the nanostructures so that gas molecules interacts more efficiently. Each morphologies have its own advantage and contributes in improving gas sensing. The MoS_2 flowers have a high surface area and provide higher adsorption sites for gas molecule adsorption. The hollow microspheres offer a larger surface area (inner and outer surface for molecule adsorption) than the solid spheres. The one-dimensional MoS_2 NWs provides a combination of high surface area and active sites which will be further increased at moderate temperature.

5.3 Experimental Investigation of Metal Nanoparticle Doping of MoS_2

In Sect. 4.4, we already discussed various theoretical reports where MoS_2 was doped with different metal atoms and the advantage of metal doping in MoS_2 predicted for NO_2 sensing. Here, we addressed the experimental picture of metal doping in MoS_2 for NO_2 sensing. MoS_2 has a large surface to volume ratio which provides unique opportunities to surface functionalization with metal nanoparticles (NPs) such as Ag, Au, Pt, Pd, and Rh and many more. The incorporation of MoS_2 surface with metal NPs could be an efficient way to improve the electronic, optical, energy storage and catalytic properties [312–316]. Undoubtedly, functionalizing the MoS_2 film with metal NPs could open up a new era in the gas-sensing applications.

He et al. used metal nanoparticles to fabricate NO_2 gas sensor based on MoS_2 flakes. The 4-nm-thick MoS_2 film was functionalized with Pt NPs [42]. The FESEM image of Pt-doped MoS_2 film is shown in Fig. 14a. The comparative sensing performance of Pt NP-doped MoS_2, rGO-MoS_2, bare rGO, and bare MoS_2 is shown in Fig. 14b. The highest sensor response was achieved with Pt-doped MoS_2. The modulated Schottky barrier height and spillover effect was responsible for enhanced NO_2 sensing of Pt-doped MoS_2 [317–319]. The Pt NPs formed nano-Schottky barriers at different places with MoS_2. Pt extracted the electrons from the MoS_2 film and introduced p-type doping in MoS_2. Moreover, due to the spillover effect, the catalytic reactivity of NO_2 molecules was also increased. Hence, the high sensor response with Pt-doped MoS_2 was achieved. The selectivity of the Pt-doped MoS_2 is shown in Fig. 14c.

Zhou et al. decorated Au nanoparticles on MoS_2 film and performed the NO_2 detection stability of the MoS_2-Au composite [121]. The gold NPs of 50 nm diameter formed a strong bond with defects present on the edges. The Au NPs adsorbed at the edges can be seen in Fig. 14d. The NO_2 sensing ability in the dark and with the UV light exposure was also performed. The MoS_2 and MoS_2-Au composites exhibited p-type nature. The full recovery with bare MoS_2 and Au decorated MoS_2 in the dark did not be achieve. However, when sensors were illuminated with UV light, fast response with a complete recovery and a three-time greater sensor response was achieved. Figure 14e shows all sensor responses. The band diagram between MoS_2 and gold NPs are shown in Fig. 14f. It revealed that electrons were transferred from gold NPs to MoS_2 due to the difference in work function. Au NPs increased MoS_2 activity and catalytic reactivity [321]. Under UV illumination, charge transfer between the MoS_2 and Au NPs rapidly increased and led to a fast recovery. The physiosorbed O_2 and chemically adsorbed O_2 also produce a hole accumulation (HAL) layer in the MoS_2 surface similar to the metal oxides. Under NO_2 exposure, the width of the HAL layer increases and the resistance of MoS_2-Au decreases.

Liu et al. doped MoS_2 with different ratios of W metal [320]. The W metal atoms were doped in the following ratio Mo: W: 1:0, 1:1, 1:2, and 1:3 and nominated as W_0, W_1, W_2, and W_3. The FESEM images of all the four samples are shown in Fig. 14g. The average crystallite size of the W metals was 52, 45, 29, and 32 nm. When NO_2 gas exposed to W-doped MoS_2 film, sample W_2 showed the highest sensor response among all with the fastest response and recovery time.

The undoped MoS_2 has the numerous number of defects. NO_2 gas molecules adsorbed on these defective sites through the chemisorption process which leads to strong adsorption

 https://doi.org/10.1007/s40820-020-00558-3

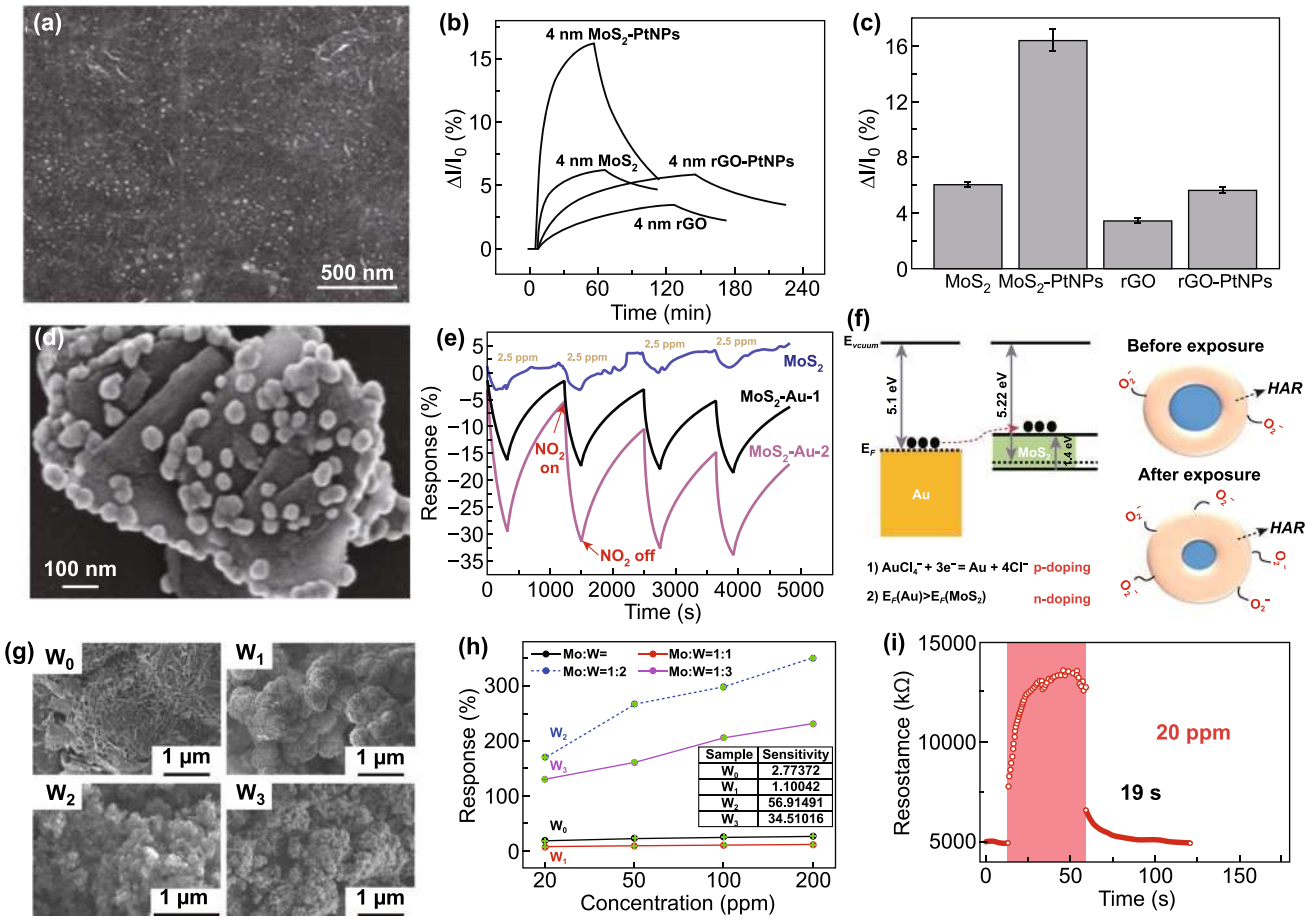

Fig. 14 **a** Pt-doped 4-nm-thick MoS_2. **b** Response of the Pt NP-doped MoS_2, MoS_2-rGo and of bare rGO. Pt NP-doped MoS_2 showed the highest response for the NO_2 adsorption. **c** Selectivity profile. Reproduced with permission from Ref. [42]. Copyright (2012) Wiley-VCH. **d** Au NP-doped MoS_2. **e** Response profile with different concentrations of Au decorated MoS_2 and with UV light exposure. **f** Band alignment of MoS_2 and Au NPs and mechanism of NO_2 adsorption. Reproduced with permission from Ref. [121]. Copyright (2018) AIP Publishing. **g** Different concentration W metal loaded MoS_2. **h** Sensor response profiles of W loaded MoS_2. **i** Response and recovery profile for 20 ppm NO_2 exposure. Reproduced with permission from Ref. [320]. Copyright (2020) Elsevier

between the MoS_2 and NO_2 molecules. Hence, NO_2 desorption is difficult from MoS_2, which leads to the sluggish recovery. Metal doping is an efficient way to improve the sensing performance. Here, authors doped MoS_2 with atoms of W metal which have close radii to Mo atoms. There are no additional defects produced in MoS_2 due to comparable radii of the Mo and W atoms. Thus the defects in MoS_2 are significantly suppressed with W metals, and NO_2 sensing performance is enhanced. The highest sensor response achieved was 56.91% in W_2 sample, can be seen from Fig. 14h. Interestingly, the response and recovery were the fastest for the sample W_2. The observed response and recovery time were 24 and 19 s, shown in Fig. 14i.

It is clear from the proposed discussion that metal NPs doping is an efficient way to enhance the gas-sensing performances of MoS_2 gas sensors. Metal (NPs) doping not only improved the chemical and catalytic reactivity in MoS_2 but also affected the electronic properties. Metal NPs formed nano-Schottky barriers in different regions of the MoS_2, which greatly increases the transfer of charges in MoS_2. Thus, metal (NPs) doping also helps in full recovery of the MoS_2-based NO_2 sensors with improved sensor response, selectivity and long term stability. In addition, illuminating the metal (NPs)-doped MoS_2 sensors could improve the sensing characteristics. However, some more rigorous efforts are still needed to completely explore the effect of light illumination on metal-doped MoS_2.

5.4 Vacancy-Driven NO_2 Sensors

Vacancies in MoS_2 played a key role and contributed to increased efficiency in gas sensing. Long et al. synthesized 3D MoS_2 aerogel by the thermal decomposition technique [24]. A two-step sulfur treatment method was employed to fabricate the NO_2 gas sensor. Figure 15a and its inset shows surface morphology without treatment and with treatment. The MoS_2 aerogel became more pours after the sulfur treatment. The MoS_2 aerogel showed a high sensor response to NO_2 gas at RT, and a rapid response and full recovery with the sulfur treatment device. The as prepared MoS_2 aerogels showed a good sensor response. However, due to the strong bonding of NO_2 with MoS_2, it suffered from slow response and recovery. The sulfur treatment in the H_2 ambient produces new sulfur vacancies. The elevated temperature generally removes the S atoms from MoS_2 and increases the vacancies in sensing film. Figure 15b, c displays the resistance versus time profile for 50 ppb NO_2 concentration at 200 °C. Furthermore, the response and recovery time were further improved with the temperature attributed to the fast desorption of NO_2 molecule at high temperature. Donarelli et al. reported the formation of n and p-type MoS_2 flakes annealed at 250 and 150 °C [31]. The SEM image of MoS_2 flakes deposited onto the Si_3N_4 with Pt electrodes is shown in Fig. 15d. Figure 15e, f shows the relative response of MoS_2 flakes to 150 and 250 °C. With the electron acceptor nature of NO_2, the resistance of the MoS_2 device annealed at 150 °C was decreased while resistance was increased at 250 °C. The device annealed at 150 °C did not respond at RT but a high sensor response was obtained at RT when the device was annealed at 250 °C. Moreover, the sensor showed better sensing performances with 250 °C annealed devices. The n-type and p-type behavior of different devices can be understood in terms of used synthesis method. The NMP was used for the synthesis of MoS_2. The NMP intercalate in between the MoS_2 layers at 150 °C. The NMP degraded and introduced the N atom at the S vacancy sites. N atom is an electron acceptor and responsible for p-type behavior [322]. In addition, MoS_2 surface was partially reduced to MoO_3 layers and more S and O vacancies were created when MoS_2 flakes are annealed at 250 °C [323]. The interaction between NO_2 sensing and n-type MoS_2 is crucially dependent on the S and O vacancies [324]. Equations 16 and 17 demonstrate the possible reaction mechanism between p-type MoS_2 and NO_2.

$$MoS_2 + V_S + NO_2 + e^-_{CB} \rightarrow MoS_2 + (NO^-_2 + V_S) \quad (16)$$

$$MoO_3 + V_O + NO_2 + e^-_{CB} \rightarrow MoO_3 + (NO^-_2 + V_O) \quad (17)$$

where $(NO^-_2 + V_O)$ and $(NO_2 + e^-)$ are the adsorbed NO_2 on the oxygen and S vacancies. e^-_{CB} is the electron in the conduction band. Hence, NO_2 interacts with e^-_{CB} and leads to a decrease in the conduction band electrons with an increase in the resistance of the electrons.

Kumar et al. annealed the vertical aligned MoS_2 flakes at 600 °C to obtain vacancy-enriched MoS_2 flakes. The S atom has low binding energy of (2.12 eV). Hence annealing the MoS_2 flakes at higher temperatures could be useful to create the S vacancies. Further, the MoS_2 flakes were decorated with the crumpled rGO. The FESEM image of vertical aligned MoS_2 flakes is shown in Fig. 15g and rGO decorated flakes showed in the inset of Fig. 15g. The dynamic sensing response of pristine MoS_2, Sv-MoS_2, rGO-MoS_2, and rGO/Sv-MoS_2 investigated at 50 °C with 50 ppm NO_2 concentration and showed in Fig. 15h.

The NO_2 sensor response was 27%, 34%, and 39% for pristine MoS_2, Sv-MoS_2, and rGO-MoS_2, respectively. However, the full recovery and high sensor response of 72% was achieved with rGO/Sv-MoS_2. The oxygen present in rGO formed strong bonds with S vacancies of MoS_2 and attracted 0.997 electrons from MoS_2/rGO. Therefore, there was sufficient transfer of charge between the MoS_2 and rGO which modified the nature of MoS_2 from n-type to p-type. S vacancies specifically play a major role in the charge transfer between MoS_2 and rGO. When NO_2 molecules were exposed to rGO/Sv-MoS_2, electrons were depleted from rGO to MoS_2 and the Fermi level of rGO shifted towards the valence band. Hence, a large number of electrons transferred from the MoS_2 to rGO. Also, further NO_2 exposure enhances the holes in MoS_2 and therefore MoS_2 behaves as a p-type. The schematic of the proposed mechanism is shown in Fig. 15i.

The role of vacancies in gas sensing has been cleared from the above discussion. The vacancies can change the electronic, optical, and chemical activity of the MoS_2. The gas molecules interaction at these vacancies sites

 https://doi.org/10.1007/s40820-020-00558-3

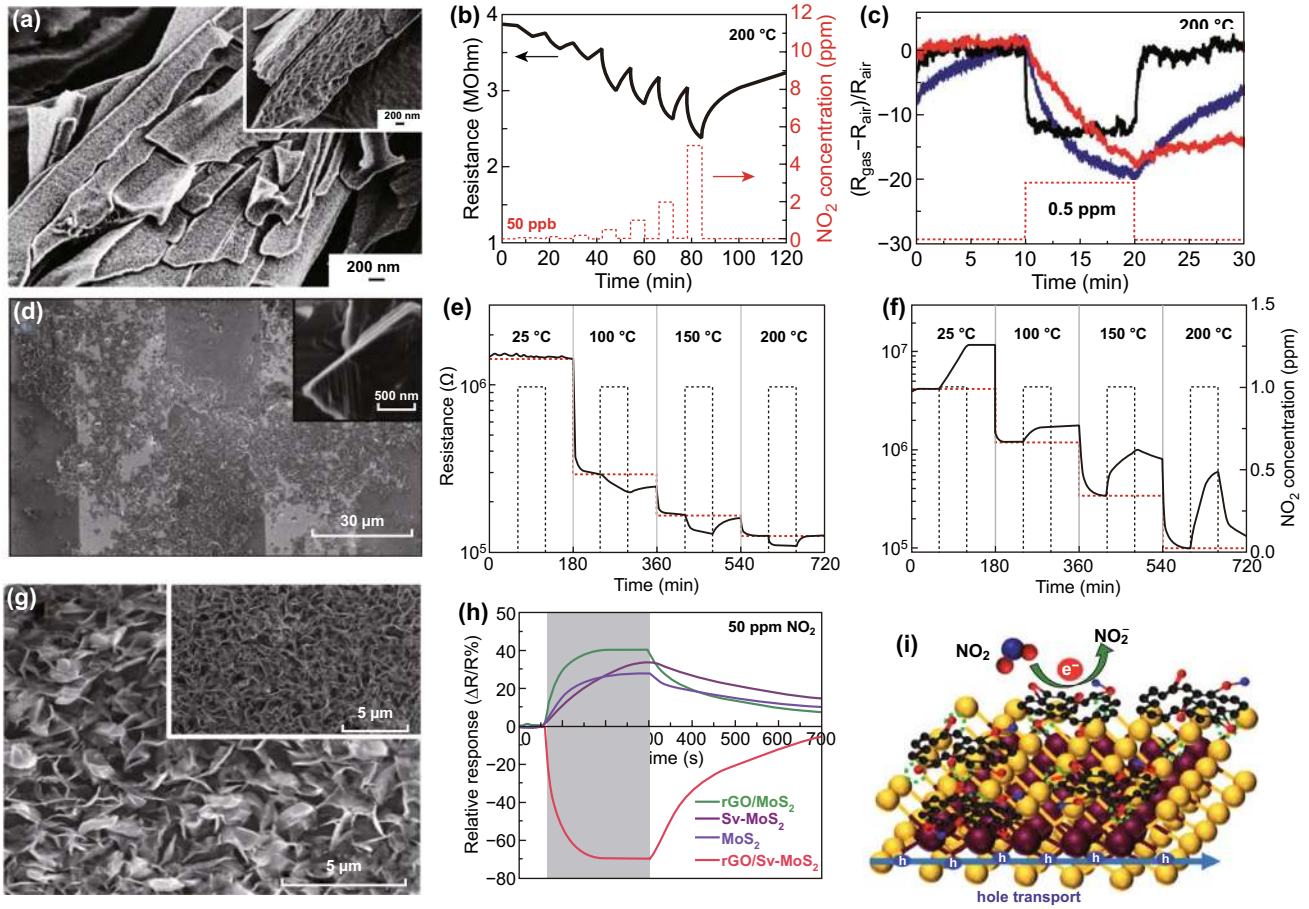

Fig. 15 **a** FESEM image of 3D MoS_2 aerogels. **b** Response of MoS_2 aerogel with NO_2 at 200 °C. **c** Device response to NO_2 at different temperatures. Reproduced with permission from Ref. [24]. Copyright (2017) Wiley-VCH. **d** FESEM image of MoS_2 flakes distributed on the Pt electrodes. NO_2 response of the MoS_2 flakes: **e** annealed at 150 °C showed p-type behavior; **f** annealed at 250 °C showed n-type behavior. Reproduced with permission from Ref. [31]. Copyright (2015) Elsevier. **g** FESEM image of sulfur vacancy-enriched MoS_2 flakes. **h** Response of 50 ppm NO_2 with MoS_2, rGO/MoS_2, Sv-MoS_2, rGO/Sv-MoS_2. rGO deposited Sv-MoS_2 shown p-type behavior. **i** Mechanism of NO_2 interaction with rGO deposited Sv-MoS_2. Reproduced with permission from Ref. [310]. Copyright (2019) IEEE

is governed by the chemisorption process. Thus, the vacancy-enriched MoS_2 has enhanced NO_2 sensing performance in terms of sensor response and speed. The vacancies can be tailored through morphology and these vacancies work as the active sites to enhance the gas molecules adsorption. Moreover, the functionalization of vacancies with substitutional atoms can change their electronic nature from n-type to p-type such as N, B, O, and Ni. Another important aspect on the vacancies is the effect of the high temperature annealing of the MoS_2 film. The high temperature ~ 500–600 °C annealing can generate the more vacancies in MoS_2 which will be helpful in designing the high-performance NO_2 sensors based on MoS_2.

5.5 Light-Assisted NO_2 Sensors

The MoS_2 has shown high adsorption energy for NO_2 molecules at RT. NO_2 is adsorbed through the chemisorption and physisorption process on the MoS_2 surface. This high adsorption energy causes difficulty in the full recovery of MoS_2. MoS_2 requires additional efforts to remove adsorbed NO_2 molecules for complete recovery at RT. The one possible solution is to isolate the device temporarily from the toxic environment for complete recovery at high temperatures. However, to develop real time NO_2 sensor, this method is not feasible. Moreover, it demands necessary engineering efforts which will raise

the cost of the sensor and time consuming process. In order to accelerate the desorption rate of NO_2 molecules from the MoS_2 surface, researchers used thermal energy to achieve the fast and full recovery of MoS_2-based NO_2 sensors. However, there are certain disadvantages of running sensors at elevated temperatures. The speedy recovery is achieved at the cost of the lower sensor response. In addition, it also deteriorates the sensor's long term stability, which raises the complexity and cost of manufacturing sensing devices. Thus, it is not an effective way to run the NO_2 sensor at high temperatures. The light illumination could be an effective way to enhance the sensing performance of MoS_2-based sensors while keeping the sensor at RT. The light illumination greatly influences the adsorption, desorption and the adsorption energy. Here, we will focus on the impact of light illumination on the NO_2 sensing in this section. We have divided the light illumination into three parts UV light illumination, visible light illumination and finally in the NIR illumination.

5.5.1 Ultraviolet-Activated NO_2 Sensor

Kumar et al. studied the role of the UV light in developing the RT NO_2 sensor [119]. The CVD grown in-plane MoS_2 flakes was utilized for NO_2 gas sensing. The device schematic is shown in Fig. 16a. The NO_2 sensing was carried out at RT, 100 °C, and with UV illumination at RT (Fig. 16b, c). Among them, the highest sensor response with full recovery was found with the UV light illumination at RT (Fig. 16c). The sensor did not recover fully at RT without UV lighting. The sensor response under tunable UV light intensities from 0.3 to 2 mW cm^{-2} was tested. The sensor response was lowest at 2 mW cm^{-2} and the highest sensor response was recorded at 1.2 mW cm^{-2}. The high light intensity allows NO_2 molecules to desorb easily than their adsorption. Thus, NO_2 sensor response was lowest at a high light intensity.

Agrawal et al. utilized mixed MoS_2 flakes for NO_2 sensing [120]. The NO_2 sensing at RT, 125 °C, and with UV light illumination at RT was explored. The highest sensor response, fast and full recovery were obtained with UV light illumination at RT. The schematic of the mixed MoS_2 flakes with possible NO_2 adsorption sites, the response of mixed MoS_2 flakes and comparative sensor response under UV light is shown in Fig. 16e–g. The gas-sensing mechanism for both the studies is discussed as follows. The sensing behavior of MoS_2 flakes is highly dependent on the surface morphology, the number of active sites and notably on the defects in the form of vacancies. The environmental impurities such as oxygen and humidity get adsorbed on these defects. The adsorbed oxygen takes the electrons from the MoS_2 flakes and introduces p-type doping. At RT without UV light illumination, a high amount of oxygen is adsorbed on the MoS_2 flakes and a large number of electrons are extracted from MoS_2 flakes. Owing to the electron acceptor, NO_2 withdrawn electrons from the MoS_2. However, the desorption rate is not fast due to the strong bonding of NO_2 and led to incomplete recovery. Moreover, when thermal energy is added in MoS_2 from external sources, some oxygen in the MoS_2 flake is desorbed and more fresh active sites in the form of defects are formed. In addition, thermal energy speeds up the desorption process that causes the sensor response to decrease. The desorption rate of oxygen molecules was highest under UV illumination. UV light illumination generates new electron and hole pairs. The photogenerated holes react with adsorbed oxygen and adsorbed oxygen gets released from the MoS_2 surface. The UV light illumination creates more fresh active sites. On these fresh active sites, the NO_2 molecules get adsorbed and increase sensor response. Moreover, when NO_2 gas turned off, the adsorbed oxygen reacted with the photogenerated electrons and desorbed easily from the MoS_2 surface. The recovery rate therefore improves under UV lighting. The proposed sensing mechanism for both the reports is shown in Fig. 16d, h.

Zhou et al. fabricated an ultrasensitive, fast UV assisted, RT NO_2 sensor [325]. The detection limit of the fabricated MoS_2/ZnO NO_2 was very low (50 ppb). The n-type ZnO NWs were synthesized using the hydrothermal process, while the ultrasonic method was used to synthesize the p-type MoS_2. Two types of sensors were fabricated with different composites amount of MoS_2 and ZnO such as MoS_2/ZnO (0.5:0.25) and MoS_2/ZnO (0.25:0.25). The device schematic is shown in Fig. 16i. The bare MoS_2 device did not show any NO_2 sensing capability which may be due to the low conductivity of the flakes. However, both devices exhibited significant sensor response under UV exposure. Moreover, devices with equal MoS_2 and ZnO composites showed better NO_2 sensing performance under UV light illumination, can be seen from Fig. 16j. The gas-sensing mechanism was proposed based on the band alignment as shown in Fig. 16k, l. MoS_2 has p-type nature and electrons transferred from the MoS_2 conduction

 https://doi.org/10.1007/s40820-020-00558-3

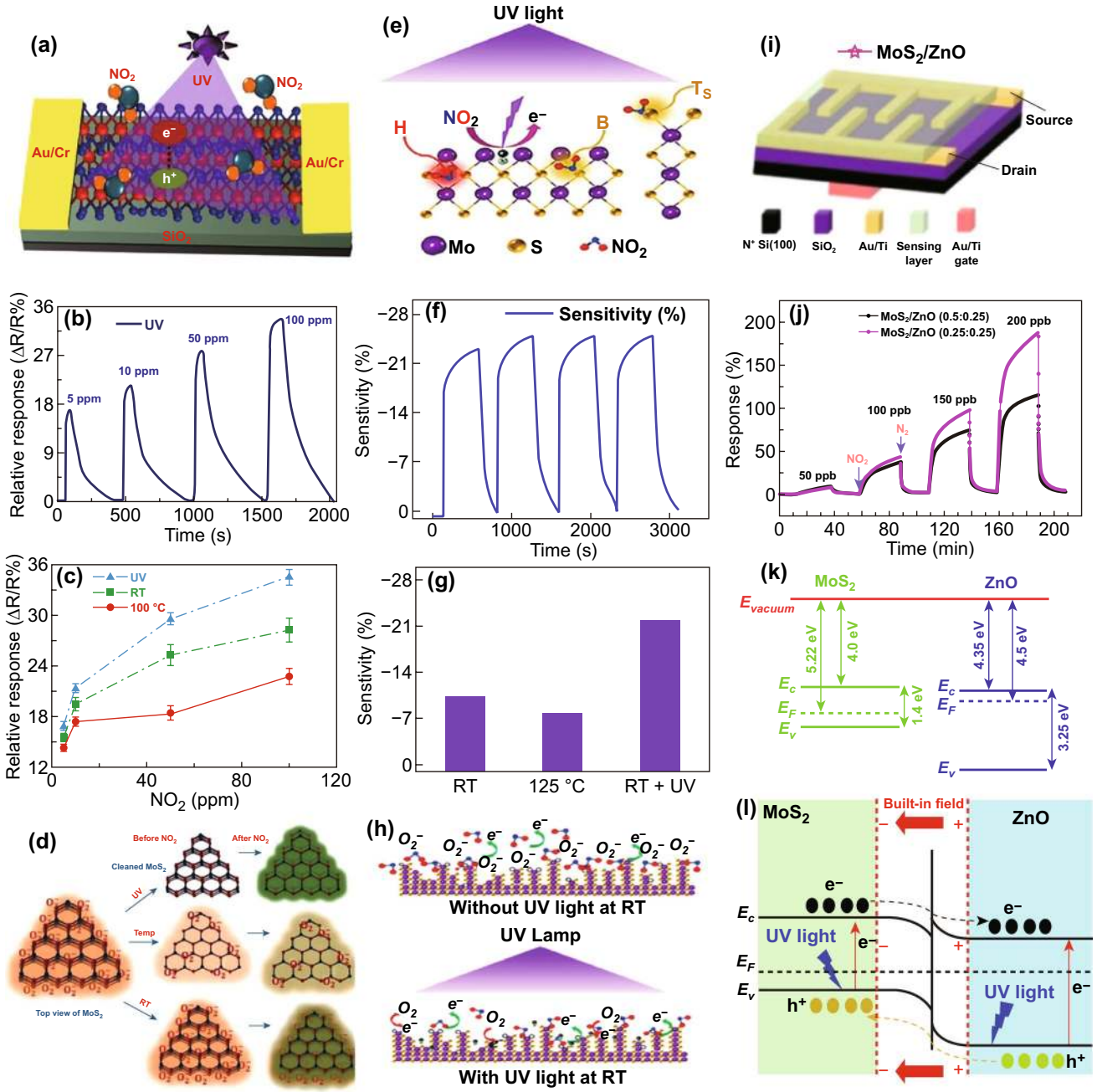

Fig. 16 **a** Schematic view of the proposed device under UV illumination. **b** NO_2 response under UV light, **c** comparative performance under UV at RT, RT, and at higher temperature. **d** Working mechanism. Reproduced with permission from Ref. [119]. Copyright (2017) American Chemical Society. **e** Proposed working mechanism under UV light. **f** Sensor response profile under UV light. **g** Comparative NO_2 sensing bar profile. **h** Working mechanism under UV illumination. Reproduced with permission from Ref. [120]. Copyright (2018) American Chemical Society. **i** Device schematic for NO_2 sensing. **j** NO_2 response with different concentration MoS_2/ZnO composite device. **k**, **l** Band alignment before the junction and after the formation of contact with NO_2 exposure. Reproduced with permission from Ref. [325]. Copyright (2018) The Royal Society of Chemistry

band to the ZnO conduction band under UV illumination. Thus, the photogenerated charge carriers were segregated efficiently and prevent further recombination.

5.5.2 Visible Light-assisted NO_2 Sensors

The UV light illumination has evidently proved its significance and its critical role in achieving the fast recoverable NO_2 sensors for the RT. However, the UV illumination has certain disadvantages as well. Practically, the use of UV light is still a vivid challenge. UV radiation is harmful to human wellbeing. World cancer research agency identified that the continuous use of UV radiation is harmful to humans. Continuous exposure of UV light can cause premature aging of the skin in terms of wrinkles, leathery skin and solar elastosis. UV radiation is therefore particularly harmful to human vision. UV radiation can easily damage the corona of the eyes. The UV rays can significantly affect the immune system. Furthermore, the cost of UV lamps is very high. Therefore, it is essential to study the role of visible light on the gas sensing.

Late et al. studied the role of light exposure in NO_2 gas sensing. Traditionally, the UV light is the most adopted light source for sensing measurements. However, continuous UV light exposure may degrade the sensing performance of the device and harmful to humans [327]. Thus, the authors used safe green light of 532 nm to perform the NO_2 gas-sensing measurements.

The irradiated green light has tunable power densities from 4 to 50 mW cm^{-2}. The highest resistance change has been observed with higher incident power, which is attributed to the higher number of photogenerated electrons and holes with higher incident light power. The change in the resistance with incident light power density is shown in Fig. 17a. With light illumination, the desorption rate of NO_2 gas molecule is relatively high in comparison with the adsorption rate. Moreover, a small fraction of electrons reacts with NO_2 gas due to the high power density of incident light. Therefore, the NO_2 sensor response is reduced

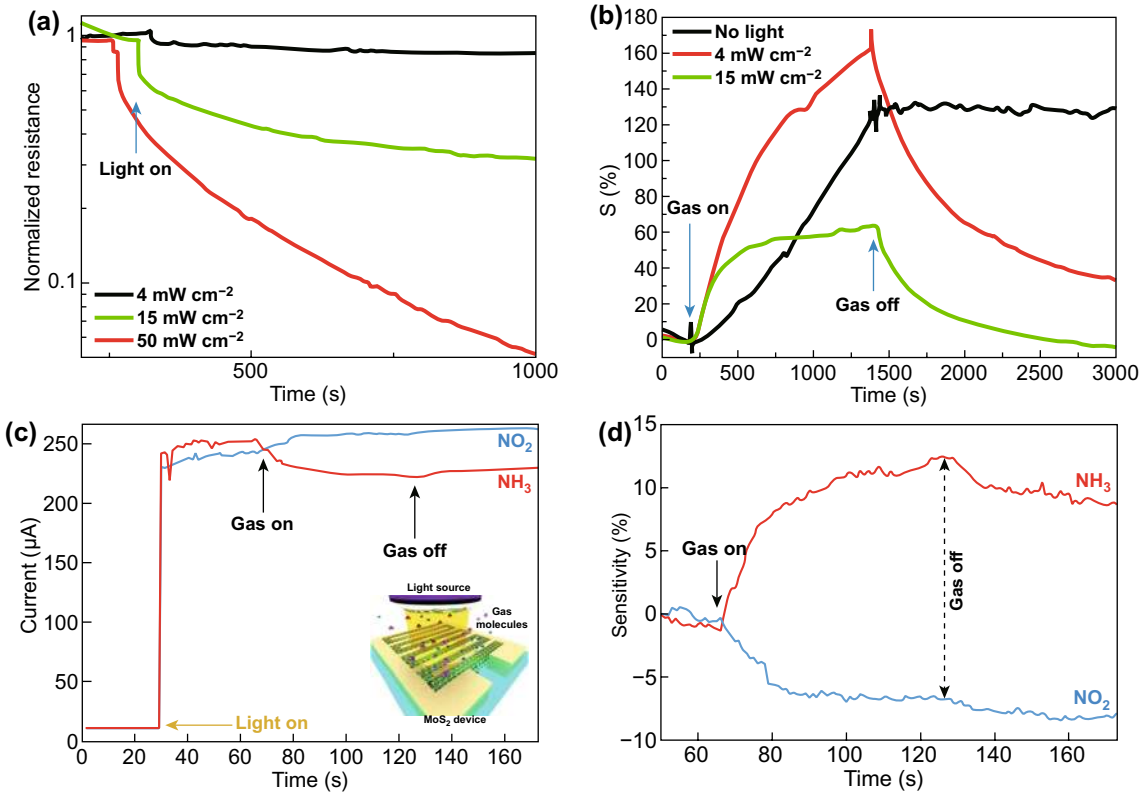

Fig. 17 **a** Effect of power density on the resistance. **b** Effect of power density on the NO_2 response. Reproduced with permission from Ref. [17]. Copyright (2013) American Chemical Society. **c** Detection of the NO_2 and NH_3 exposure with 650 nm wavelength exposure. **d** Change in the sensor response under light illumination. Reproduced with permission from Ref. [326]. Copyright (2015) American Chemical Society

https://doi.org/10.1007/s40820-020-00558-3

with a high incident power density as shown in Fig. 17b. The full recovery is obtained with green light illumination. Similarly, Cho et al. synthesized atomic layered MoS_2 and illuminated device with 650 nm red light [326]. The schematic of the device is shown in the inset of Fig. 17c. The photogenerated current increased rapidly when the red light was turned on after 30 s. NO_2 gas was turned on after 60 s. The current increased further implying the p-type characteristic of the MoS_2 flakes. The calculated sensor response with red light illumination is shown in Fig. 17d.

5.5.3 Near-Infrared (NIR)-Assisted NO_2 Sensor

Xia et al. recently used NIR light to develop sensitive fast NO_2 sensor with sulfur vacancy-enriched MoS_2 flakes [123]. The conventional MoS_2 (C-MoS_2) and sulfur vacancy-enriched MoS_2 (S-MoS_2) flakes were synthesized by the traditional microwave-hydrothermal method. The sulfur vacancies were investigated by the electron paramagnetic resonance (EPR), XPS, and XRD. The schematic structure of C-MoS_2 and Sv-MoS_2 is shown in Fig. 18a. Further, the absorption spectroscopy has been performed for both the C-MoS_2 and Sv-MoS_2 which revealed the high absorption of NIR light by Sv-MoS_2. The NO_2 sensing ability of the C-MoS_2 and Sv-MoS_2 is shown in Fig. 18b, c. Interestingly, the observed sensor response with Sv-MoS_2 was high in the presence and in the absence of NIR light. The presence of S vacancies modulated the band structure of MoS_2 flakes and generated three additional localized states in MoS_2 bandgap, i.e., two unoccupied states at 0.63 eV below the conduction band and one shallow state near the valence band (Fig. 18d, e). Both additional states narrow down the MoS_2 bandgap in contrast with the pure MoS_2 bandgap. Hence, Sv-MoS_2 showed a high NIR photoresponse.

The S vacancies quickly reduced the Gibbs free energy of adsorbed gas molecules and increased the electron transfer rate from MoS_2 to NO_2. The Sv-MoS_2, therefore provides enhanced sensing efficiency not only in the dark but also with NIR lighting. The gas sensing performances of light driven MoS_2-based NO_2 sensors summarized in Table 4.

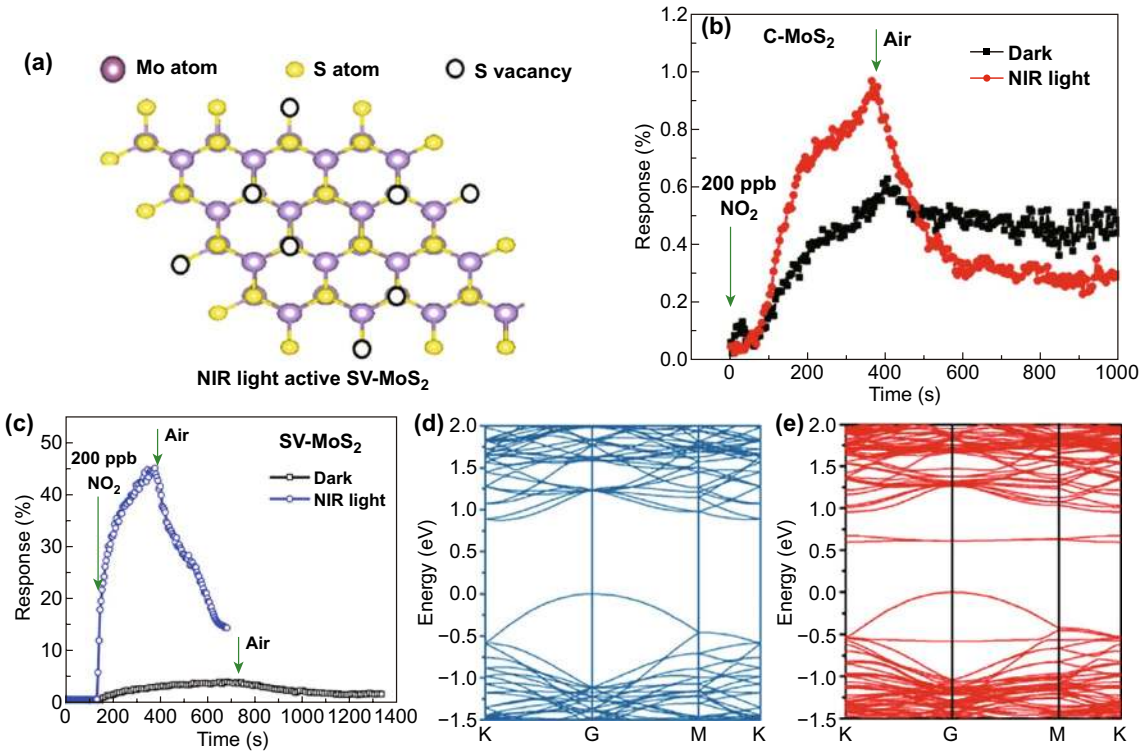

Fig. 18 **a** Schematic of NIR light-activated sulfur vacancy-enriched MoS_2 (Sv-MoS_2). **b** Response of C-MoS_2 in dark and NIR with NO_2 exposure. **c** Response of Sv-MoS_2 in dark and NIR with NO_2 exposure. Band structure of **d** C-MoS_2 (blue) and **e** Sv-MoS_2 (red). Reproduced with permission from Ref. [123]. Copyright (2019) American Chemical Society. (Color figure online)

Table 4 Summary of the light-driven NO_2 sensor of MoS_2

Sensing film	Method	Electrodes	Def.	Device	Conc. (ppm)	P/λ (mW/cm^2/nm)	T (°C)	S (%)	Res time	Rec. time	References
Multi MoS_2	CVD	Au/Cr	$\frac{(R_{gas}-R_{air})}{R_{air}}$	Resistor	100	1.2/365	RT + UV	35.16	29	350	[119]
Mix MoS_2	CVD	Au/Cr	$\frac{(R_{gas}-R_{air})}{R_{air}}$	Resistor	10	3/365	RT + UV	21.78	6.1	146.5	[120]
MoS_2/ZnO	Hydrothermal	Au/Ti	$\frac{(R_{gas}-R_{air})}{R_{air}}$	FET	50	1/365	RT + UV	188	60	60	[325]
MoS_2	CVD	Pt	$\frac{R_{gas}}{R_{air}}$	Resistor	10	0.29/365	RT + UV	25.3	–	63.9	[328]
ZnO/MoS_2	Ultrasonication	ITO	$\frac{(R_{gas}-R_{air})}{R_{air}}$	Resistor	10	360	RT + UV	293	258	72	[329]
1L MoS_2	CVD	Cr/Pd/Au	$\frac{(R_{gas}-R_{air})}{R_{air}}$	Resistor	0.4	4/625	RT + 625	670	16	65	[122]

These studies revealed that under light illumination gas-sensing performance of MoS_2 is critically affected. Light illumination is a promising approach to enhance the sensor response of MoS_2 in comparison with providing thermal activation. The electrons and holes pairs generated due to light illumination provide a sufficient number of charge carriers to increase the gas-sensing response of the MoS_2 sensors. Traditionally, UV light is the most verified technique to enhance the sensor response of gas sensors and also with MoS_2. UV illumination provides better treatment of adsorbed ambient oxygen than thermal energy. UV illumination significantly cleans environmental oxygen from the MoS_2 surface without any structural loss than the thermal energy. But, long term exposure of UV is not good for living cells.

Furthermore, the integration of MoS_2 with NO_2 sensitive materials could be helpful in developing ultrasensitive NO_2 sensors at RT with light. MoS_2-Heterojunctions rapidly separate the generated electron and holes pairs due to light and NO_2 exposure, which will improve the gas-sensing performance.

MoS_2 has a high absorption coefficient in the visible region of spectrum of spectrum. Thus, a large number of electrons generate in MoS_2 in visible region and NO_2 has high number of electron available to withdraw from MoS_2 surface. However, with UV light, the number of generated electrons holes pairs are not so high. So, utilizing the visible spectra in gas sensing could be a better and safe approach to fabricate the high-performance gas sensors. To further utilize the NIR spectra, some engineering efforts may be needed to enhance the absorption of MoS_2 in NIR. Use of NIR light sources will reduce the high cost of the sensors in comparison with UV and visible light sources.

6 MoS_2-Heterostructure NO_2 Sensor

Advancement in MoS_2 gas sensors can be achieved by forming the heterostructures. The production of single or few layer MoS_2 is considered not an easy approach and limits the high throughput of gas sensor. Ambiguity in the gas-sensing mechanism of MoS_2 with NO_2 gas has also been a topic of debate. Integration of MoS_2 with other materials such as graphene derivative, metal oxides and carbon materials create heterostructure at the junction. The formation of heterostructure affects the gas-sensing properties in both positive and

https://doi.org/10.1007/s40820-020-00558-3

negative aspects. Forming a heterojunction can improve the intrinsic electronic properties of MoS_2 that tends to improve the sensor response and recovery time. However, the integration of heterostructure also puts a bit of complexity in the gas-sensing mechanism. Here, in this section, we tend to summarize the advancement in the material of different dimensions with MoS_2 equipped gas sensor over time.

Despite showing high sensor response by few layer MoS_2-based TFT sensor, their low conductivity limits the performance of device [34, 218]. The high surface to volume ratio of graphene and its derivatives opened up possibilities of hybrid gas sensors, where graphene and its derivative provided better electrical conductivity to the device. Theoretical calculations done using DFT have expounded that pollutant gases, like NO_2, NO, and SO_2, firmly interact with MoS_2 surfaces. Numerous experimental confirmations of these theoretical results have been reported. A three-layer-grown MoS_2-based resistive sensor showed a NO_2 detection limit of 120 ppb in dark conditions [326].

In order to improve the sensing behavior, the blending of MoS_2 with graphene nanosheet was adopted [42, 330, 331]. To enhance the sensor response and selectivity to NO_2 more, a composite of reduced graphene oxide (rGO) and MoS_2 was prepared [332]. The p-type nature of rGO, due to oxygen and water doping and n-type nature of MoS_2 make p–n junction. MoS_2 provided selectivity and sensibility, while rGO had provided betterment in electronic properties. Zhou et al. also fabricated rGO/MoS_2 gas sensor for NO_2 detection [333]. The fabricated composite structure showed 200% enhanced performance than the bare rGO sensor. The device showed sensing response of 59.8% towards 2 ppm NO_2 at 60 °C.

On the contrary, Long et al., fabricated gas sensor using MoS_2/graphene hybrid aerogel for NO_2 detection [118]. The MoS_2/graphene-based sensor showed ultralow detection limit of 50 ppb NO_2. The hybrid was integrated over low power micro heater for temperature-dependent gas detection measurement and on heating at 200 °C sensor show improved recovery and response time of less than 1 min compared to RT measurements. The schematic and optical image of the device with microheater is shown in Fig. 19.

Many other works have been reported where the sensing performance was improvised by using graphene over MoS_2 [334, 335]. Despite the good selectivity of the MoS_2/rGO sensor, the MoS_2 has serious issues like agglomeration on the substrate. Therefore, the fabrication of MoS_2 gas sensor with enhanced sensing activity was a challenge. CdS was used as sensing material and assumed to provide good electron transfers between heterostructure [336].

Tabata et al., fabricated gate tunable MoS_2/graphene NO_2 sensor [29]. To understand the role of only heterojunction, the other gas-sensing parts were passivated by the gas barrier layer. Poly methyl methacrylate (PMMA) was used as gas barrier layer. The device showed the strong dependencies on the type of bias (forward or reverse) and back gate voltage. With an increase in reverse bias and negative gate voltage device showed better performance. Jung et al. also fabricated the flexible gas sensor by transferring the MoS_2/rGO on the PET substrate that showed optical transmittance ~ 93% [337]. The flexible MoS_2/rGO showed good performance at a bending radius of 14 mm and detection as low as 0.15 ppm of NO_2.

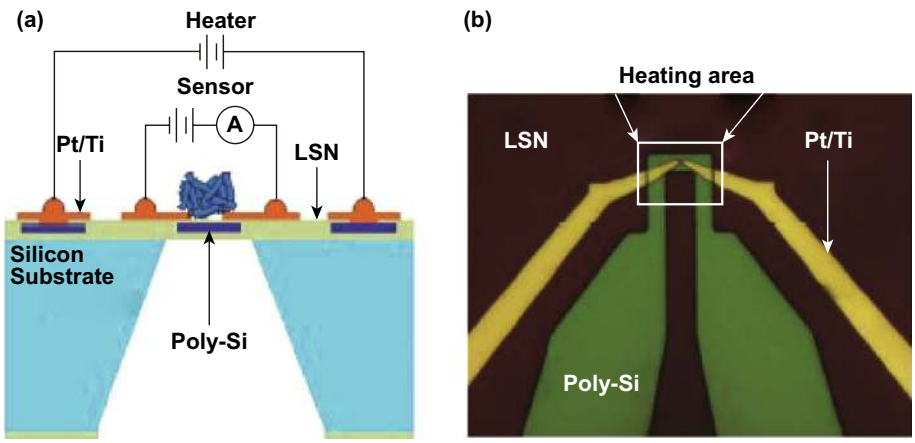

Fig. 19 **a** Schematic diagram of NO_2 gas sensor with microheater sensor. **b** Optical image of poly-silicon microheater with Pt/Ti electrodes. Reproduced with permission from Ref. [118]. Copyright (2016) Wiley-VCH

On the contrary, Ikram et al. used a thin layer of $In(OH)_3$ on the MoS_2 nanosheets to improve the performance of NO_2 gas sensor [338]. The presence of point and line defects in $MoS_2/In(OH)_3$ improves the electrical conductivity and provides the accessibility of active sites for target gas. The ease of fabrication of MoS_2/MoO_3 composites in one step has also grabbed attention and the sensor showed a remarkable sensor response of ~ 33.6% with complete recovery to 10 ppm NO_2 at RT [339]. The sensor response of 2D materials to the surrounding critically affect the long-term reliability of the sensing device. Therefore, Shi et al. fabricated a layered device using black phosphorus (BP) as the top gate, Boron nitride as a dielectric layer and MoS_2 as conduction channel [340]. The gas adsorption ability of BP makes it a gas-sensing material and BN isolates the conduction channel of MoS_2 from ambient. The multilayered gas sensor showed a detection limit of 3.3 ppb to NO_2. The SnS_2 nanosheets were also used to fabricate the sensor due to their high adsorption sites availability and showed response 22.3 times higher than pristine SnS_2 sensor [341].

Apart from the integration of 2D nanostructure with MoS_2, integration of 1D also offers enhancement in gas-sensing properties. Deokar et al. fabricated CNT/MoS_2-based hybrid NO_2 gas sensor [342]. Hexagonal shaped MoS_2 nanoplates were grown on vertical aligned CNTs. Few tens (25, 50, 100) of ppm to hundreds (25, 100) of ppb of NO_2 at RT was monitored. An illustration of the gas-sensing mechanism of 2D/1D heterostructure is depicted in Fig. 20.

Zhao et al. fabricated a hybrid of MoS_2/porous Si nanowire [343]. The MoS_2 nanosheets were grown by sulfurization of Mo thin film deposited using DC magnetic sputtering. The hybrid device showed better performance than bare MoS_2 and porous Si NW with low detection concentration of 1 ppm. Keeping the success of MoS_2 and porous Si NW in attention, ZnO nanowires were also used in forming the heterostructure [344]. MoS_2 was grown by the same sulfurization of Mo thin films deposited by DC magnetic sputtering. The MoS_2 on ZnO NW showed an excellent sensor response, recovery, repeatability and selectivity up to low detection of 200 ppb. MoS_2, that naturally act as n-type semiconductor forms heterostructure with n-type ZnO NW and charge interfacial charge separation takes place. The electron in the CB of MoS_2 flows to the CB of ZnO NWs till their Fermi level gets aligned. The type of heterostructure (type I and type II) can be decided by the band gap and the work function of the two materials. Similarly, other reports were also reported where ZnO nanowires were used with p-type MoS_2 nanosheets to improve the sensors performance [345].

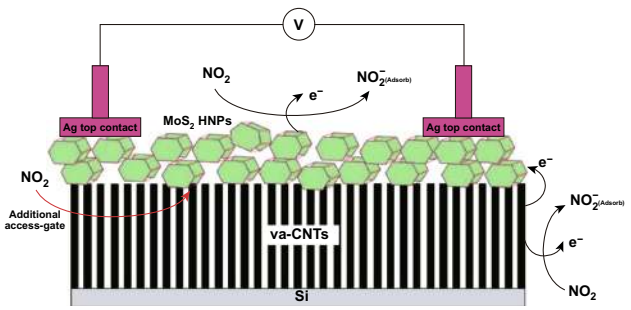

Fig. 20 Schematic of MoS_2 deposited over CNT-based device. Reproduced with permission from Ref. [342]. Copyright (2017) Wiley-VCH

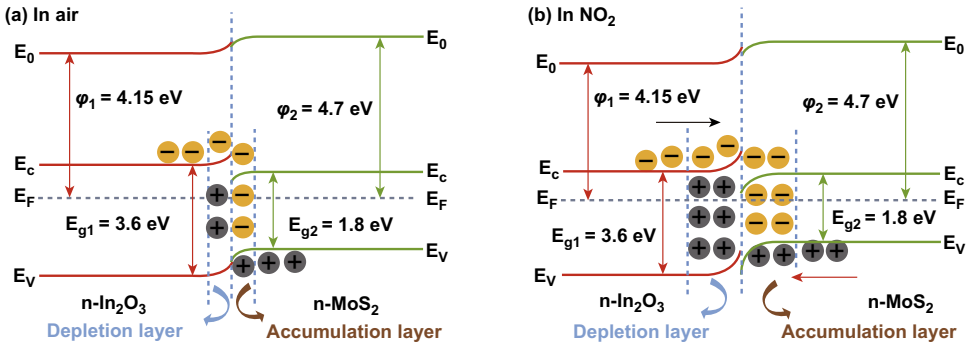

Fig. 21 Energy band diagram of In_2O_3/MoS_2 heterojunction in **a** air and **b** NO_2 ambient. Reproduced with permission from Ref. [346]. Copyright (2019) Elsevier

 https://doi.org/10.1007/s40820-020-00558-3

On the contrary to NW and CNTs, hollow tubes have also been considered and effective 1D nanostructure for enhancing the gas-sensing properties. Yang et al. fabricated NO_2 gas-sensing device using In_2O_3 hollow tube and MoS_2 nanoparticles [346]. The In_2O_3/MoS_2 composite synthesized by layer by layer technology. Both n-type metal oxides nanostructure and n-type MoS_2 form a heterostructure. Depending upon the band gap and work function, the majority carrier flows from CB of MoS_2 to CB of metal oxide (MO) nanostructure and vice versa till their Fermi level gets aligned. When the sensor is exposed in the air ambient, the oxygen molecules capture electrons from MoS_2 and MO nanostructure and forms O_2^- ions. An energy band diagram that explains the sensing mechanism in the air and in NO_2 ambient is shown in Fig. 21. Once the sensor is exposed into NO_2 ambient, the NO_2 molecules capture electrons from the sensing layer and adsorbed O_2^-, hence increase the device resistance.

When the sensor is again released in the air ambient, the electron trapped by NO_2 is again released to CB sensing materials leading to the restoration of device resistance. In band diagram terminology, when the sensor is exposed to the NO_2, the electrophilic nature of NO_2 reduces the carrier concentration in the depletion region resulting an increase in the resistance. Therefore, the quality of the interface between the MoS_2 and MO nanostructure greatly affects the sensing properties.

Among different heterojunctions, 2D/0D offers improved gas-sensing properties (sensor response, recovery time, and improved time) due to the enhanced penetration and diffusion of gas molecules. The first 2D/0D hybrid heterostructure was fabricated and demonstrated by Han et al. for gas NO_2 gas sensing. Han and co-workers fabricated 2D/0D heterojunction using MoS_2 nano-sheets and ZnO NP that exhibited sensor response of 3050% for 5 ppm NO_2 and long term stability of 10 weeks at RT [347].

The gas-sensing mechanism of 2D/0D heterostructure is explained with the help of Fig. 22. The defects on the surface of as deposited p-type MoS_2 act as active sites for gas sensing. NO_2 molecules accept electrons from MoS_2 and change the electronic properties of the sensor. The integration of metal oxide 0D structure (n-type) over p-type forms a p–n junction followed by the formation of the depletion layer. The electron and hole diffusion keep happening from n-type to p-type and p-type to n-type, respectively, till their fermi levels get aligned. A built-in electric field balances the flow of majority carrier. Therefore, in the air, the MoS_2/ZnO junction shows poor conductivity due to the formation of potential barrier. When the sensor is brought in the

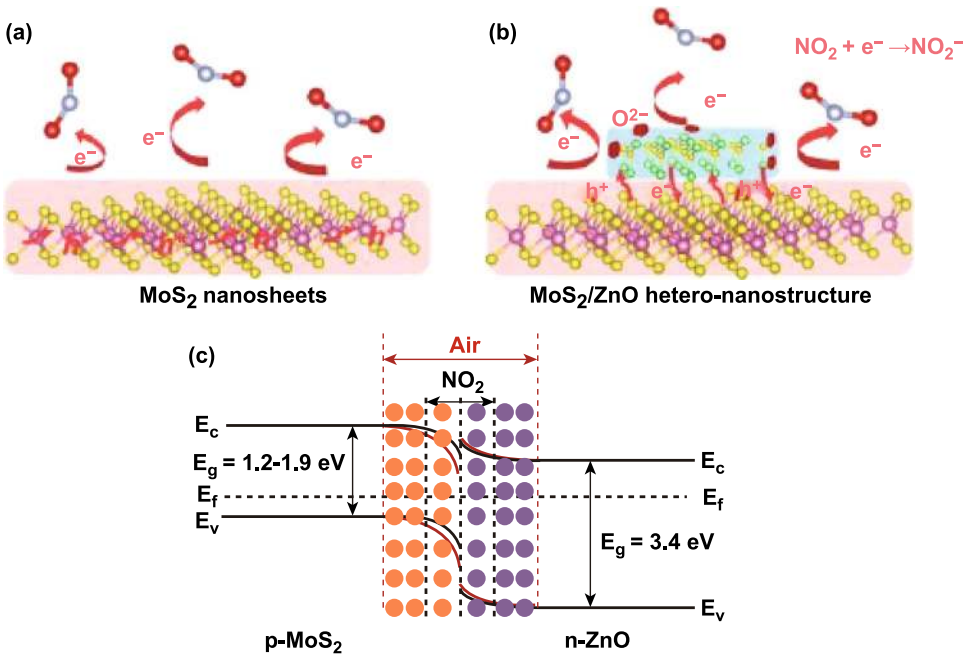

Fig. 22 Schematic of sensing mechanism of **a** pure MoS_2 nanosheets and **b** hybrid mechanism. **c** Band diagram of hybrid 2D/0D heterojunction gas sensor in air ambient and in the NO_2 ambient. Reproduced with permission from Ref. [347]. Copyright (2015) American Chemical Society

ambience of NO_2, the NO_2 molecules take electrons from metal oxide nanoparticle and the equilibrium of electron and hole is broken. The extra holes that were counter balanced by the electrons taken up by the NO_2 molecule migrate to the MoS_2. Therefore, during adsorption of NO_2, holes are accumulated on the MoS_2 surface and the width of depletion layer decreases that leads to the increase in conductivity of MoS_2/ZnO heterostructure. The increase in the conductivity of heterostructure enhances gas-sensing properties.

Another metal oxide nanoparticle that was used for the hybrid MoS_2 sensor was SnO_2 NPs. The MoS_2/SnO_2 NO-based sensor showed a response from 18.7 to 5 ppm NO_2 [348]. Similarly, Xin et al. fabricated device using PbS quantum dots [349].

The MoS_2/PbS QDs showed sensing performance better than bare MoS_2. The response showed by the hybrid device was 50 times higher than pure MoS_2 at 100 ppm with recovery ratio of around 99%. In another report, Ag nanoparticle was used for surface modification of the Fe_2O_3/MoS_2 heterojunction. The modified sensor showed response to 5 ppm NO_2 as high as 202.2% which was 11Times higher than the bare MoS_2 device [27]. On the contrary, n-type MoS_2 was also used for device fabrication. The n-type-CdTe quantum dots also used on n-type MoS_2 nanoworms to enhance the

Table 5 Summary of various MoS_2 heterostructures NO_2 sensors

Sensing film	Electrodes	Conc. (ppm)	Def	T (°C)	S (%)	Res time (s)	Rec time (S)	References
Graphene/MoS_2	Au	50	$\frac{(R_{gas}-R_{air})}{R_{air}}$	RT	83	–	–	[332]
rGO/MoS_2	Au	2	$\frac{(R_{gas}-R_{air})}{R_{air}}$	60	59.8	–	–	[333]
rGO/MoS_2	Au	3	$\frac{R_{gas}}{R_{air}}$	160	1.23	8	20	[351]
Graphene/MoS_2	Pt/Ti	0.5	$\frac{(R_{gas}-R_{air})}{R_{air}}$	200	10	21.6	29.4	[118]
MoS_2/graphene	Au	10	$\frac{(I_{air}-I_{gas})}{I_{air}}$	200	69	0.7	0.9	[334]
Graphene/MoS_2	–	500	$\frac{(R_{gas}-R_{air})}{R_{air}}$	RT	61	22	35	[335]
rGO/MoS_2/CdS	NA	0.2	$\frac{(R_{gas}-R_{air})}{R_{air}}$	75	27.4	25	34	[336]
MoS_2/$In(OH)_3$	NA	100	$\frac{R_{air}}{R_{gas}}$	RT	15.4	1.6	NA	[338]
MoS_2/MoO_3	Au	10	$\frac{(R_{gas}-R_{air})}{R_{air}}$	RT	33.5	19	182	[339]
SnS_2/MoS_2	Au	100	$\frac{R_{air}}{R_{gas}}$	RT	25.9	2	28.2	[341]
MoS_2/CNT	Ag	50	$\frac{R_{gas}}{R_{air}}$	RT	12.6	–	–	[342]
MoS_2/p-Si NWs	Ag	50	$\frac{(R_{gas}-R_{air})}{R_{air}}$	RT	28.4	–	–	[343]
MoS_2/ZnO NW	Silver	50	$\frac{(R_{gas}-R_{air})}{R_{air}}$	200	29.4	300	–	[344]
ZnO NW/MoS_2	Au/Ti	50 ppb	$\frac{(R_{gas}-R_{air})}{R_{air}}$	60	63	–	–	[345]
MoS_2/In_2O_3 NT	–	50	$\frac{R_{air}}{R_{gas}}$	RT	209	–	–	[346]
MoS_2/ZnO	Au	5	$\frac{(I_{gas}-I_{air})}{I_{air}}$	RT	3050	40	1000	[347]
MoS_2/SnO_2 NPs	Au/Ti	5	$\frac{R_{gas}}{R_{air}}$	RT	18.7	74	NA	[348]
Ag-Fe_2O_3/MoS_2	Ag-Pd	5	$\frac{(R_{gas}-R_{air})}{R_{air}}$	120	202.2	81	355	[27]
CdTe/MoS_2	Ag	10	$\frac{(R_{gas}-R_{air})}{R_{air}}$	RT	40	16	114	[350]
MoS_2/SnO_2	Au	10	$\frac{(R_{gas}-R_{air})}{R_{air}}$	RT	28	408	162	[352]

https://doi.org/10.1007/s40820-020-00558-3

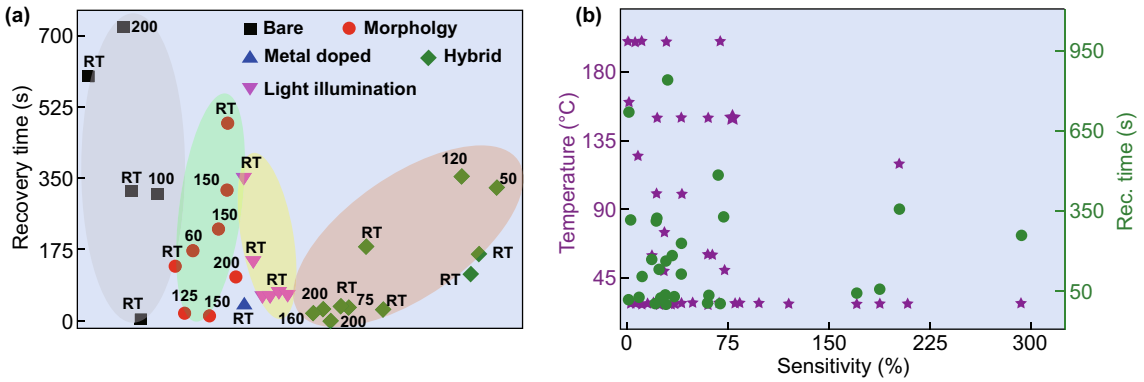

Fig. 23 **a** Summary of the recovery time obtained through various strategies in MoS_2. Bare MoS_2-based NO_2 sensors have highest recovery time followed by the morphology-driven MoS_2. The light-assisted NO_2 sensors have the lowest recovery time and can operate easily at RT. MoS_2 heterostructure-based sensors have mixed recovery time with different operating temperatures. **b** MoS_2-based sensors can operate easily at low temperatures and have low recovery time. Data presented was taken from Refs. [17, 24, 27, 31–36, 118–122, 214, 303–310, 320, 325, 328, 329, 333–336, 338–352]

sensing performance [350]. The device showed an excellent response of 40% over pristine MoS_2. The band bending of n-type MoS_2 and n-type 0D is shown in Fig. 22c. We summarized the gas-sensing performances of various MoS_2 heterostructures in Table 5.

7 Challenges and Future Perspectives

MoS_2 has shown immense gas-sensing capacity without any doubt and also shown great performance in the detection of various gas molecules like NO_2, NH_3, H_2, H_2S etc. However, some major issues still have to be overcome in order to boost the efficiency of MoS_2 gas sensors. There are several crucial challenges to be overcome to build high-performance MoS_2-based NO_2 sensors. Gas-sensing performance depends on certain important parameters including sensor response, recovery time, selectivity, and stability. MoS_2 is extremely susceptible to different gases, and its conductivity varies dramatically under exposure to these gases. A small exposure of any gas to MoS_2 will notably change sensor response. Thus, the detection of target gas molecules is critical by MoS_2.

Theoretically, NO_2 and NH_3 both have almost identical adsorption energy with similar adsorption sites. However, NO_2 has an electron acceptor nature, while NH_3 has an electron donor nature. The synthesis of such morphology which is highly selective for NO_2 molecules is therefore advantageous and can increase NO_2 selectivity. MoS_2 has a high surface to volume ratio, so it is useful to functionalize MoS_2 flakes with NO_2 capturing agents to improve NO_2 adsorption on MoS_2 flakes.

Another benefit of MoS_2 is the effective control on morphology. Morphology influences the gas diffusion in the sensing film. The role of different morphologies in detecting NO_2 has been already studied in detail with various conventional metal oxides, including ZnO, SnO_2 and in TiO_2 etc. So, there is plenty of space for NO_2 gas detection by morphology-driven sensor. In addition, NO_2 molecule adsorption on MoS_2 depends greatly on the position, so any effort to increase the NO_2 adsorption sites can not only enhance the sensor response but also boost the selectivity ability. The RT recovery is yet another big challenge for MoS_2-based NO_2 gas sensors. MoS_2 has strong adsorption energy with NO_2 gas molecules. Currently, bare MoS_2-based NO_2 sensors have experienced incomplete recovery at RT. RT thermal energy is not capable to desorb the adsorb NO_2 gas. This demands the operation of sensors at elevated temperature from RT. However, this will happen at the cost of reduce sensor response performance of the sensor. So thermal treatment for achieving full recovery is not feasible. Recently the light-assisted recovery of the gas sensors is open a new promising way to develop RT gas sensors. Light illumination not only helps in the recovery of the sensors but it also enhances the 3S performance (low response and recovery time and sensor response). Bare MoS_2-based sensors have improved RT recovery under UV light illumination so far.

Very few attempts have been made in recent years to use residual spectrum (visible, NIR, and higher region). Thus,

an intensive approach is still required to explore the wavelength-dependent NO_2 gas-sensing response and to explore light induced carrier generation and adsorption of NO_2 molecules.

Apart from the sensor response and recovery time, fast response of the gas sensor is also an essential parameter. Each sensor's response time depends on how rapidly the gas molecules reacted to sensing film and change their respective parameter. Till now, the reported response time of NO_2 molecules detection by MoS_2 is in few seconds. So, developing NO_2 sensors which can respond in few milliseconds or microseconds is still challenging. The strategy to improve the ultrafast sensors relies primarily on the interaction between gas molecules and MoS_2 and the charge transfer in MoS_2. The fast separation of the charge carriers can be improved by forming MoS_2 heterostructures sensing devices.

In addition, a proper attention is needed to pay on metal electrodes, which collect generated charges. The metal contacts has played a vital role with MoS_2 in gas sensing. Identification of high-performance metal contacts is the perquisite to utilizing the full performance of the MoS_2-based NO_2 sensors. An improved theoretical and experimental efforts with profound insight and understanding is also needed, which will contribute to the development of high-performance NO_2 sensors. Several routes to develop high-performance electrical contact should identify.

The standard air quality guidelines, according to WHO for NO_2 exposure are 82 ppb for an hour and 410 ppb for a year. Exposure to NO_2 for a long time above that level causes health problems. The recorded lower detection limit for MoS_2-based NO_2 sensor has been in the ppb. Thus, a lot of effort is needed to develop ultrasensitive NO_2 sensors, which is a crucial task. It is important to find NO_2 sensitive materials that can be easily integrated with MoS_2, and can identify the lower concentration of NO_2 easily. Furthermore, such materials should also fasten the transfer of charges for rapid sensor response. Recently, the use of spectroscopic techniques such as laser sources and electrical shields have attracted the attention of the scientific community due to their NO_2 trace detection ability. NO_2 molecules have the absorption spectrum in visible region so it offers a great chance to electronic exciton in the visible region of NO_2 molecules. The use of spectroscopic techniques for trace detection of NO_2 with MoS_2 sensors could be a new approach.

Light-assisted NO_2 sensing has attracted the scientific community over the last two years. Metal NP-doped MoS_2 sensors have already proved their importance in gas sensing. Surface plasma resonance (SPR) characteristics of MoS_2 may be a new approach to developing gas sensor-based on MoS_2. New experimental efforts should devote to harnessing the potential of plasmonic in gas sensing. SPR can stimulate the interface of MoS_2 and metal and alter the index refractive. A good choice of metal NPs and appropriate wavelengths will be helpful in designing the high-performance NO_2 sensors.

The MoS_2-based NO_2 sensors are basically chemiresistance sensors in which the change in conductance of MoS_2 film is the parameter. The conductivity of film is significantly influenced by the presence of the environment such as traces of various chemicals, moisture, humidity, corrosion due to toxic vapors, residual charges. These all drastically reduce the reliability, stability and repeatability of gas sensors. Efforts are required to increase the stability of the sensing devices.

8 Conclusions

In this review, we summarized the various theoretical and experimental strategies employed to fabricate MoS_2-based NO_2 gas sensors. We critically discussed the advantages of utilizing the 2D MoS_2 in developing NO_2 sensors. We briefly discussed the noble properties of MoS_2 and established MoS_2 as a potential candidate for the gas sensing. The inherent nonzero bandgap, high carrier mobility, fast charge transport, high reactivity, presence of favorable adsorption sites, large surface to volume ratio, and optical properties make MoS_2 amenable for gas molecule adsorption. Both theoretical and experimental studies have confirmed that NO_2 adsorption in MoS_2 is controlled by the charge transfer process. NO_2 behaves as a strong oxidizing agent and depletes the electrons from MoS_2. Theoretical studies revealed NO_2 adsorption in MoS_2 is position dependent. The 2H and 1T MoS_2 have their importance in NO_2 gas sensing. Although most of the work to fabricate MoS_2-based NO_2 sensor have been carried out with 2H-MoS_2 phase, but the 1T MoS_2 phase is emerged as the potential candidate for NO_2 detection. The aforementioned hypothesis has been verified theoretically and must be taken into account in experiments as well. Theoretical and experimental studies confirmed that

 https://doi.org/10.1007/s40820-020-00558-3

the defective MoS_2 have higher interaction and have high NO_2 detection ability than the pristine MoS_2. Furthermore, metal doping at the vacancy sites is an alternative way to develop highly sensitive, fast response and RT-recoverable NO_2 sensors. Different MoS_2 morphologies have different number of NO_2 adsorption sites. Thus, NO_2 sensing performance of MoS_2 could be further improved and determined by morphology.

The formation of MoS_2 heterostructures can significantly affect the NO_2 sensing performances. MoS_2 heterostructures rapidly separate the charges and could be helpful in developing fast response and recover gas sensors. Among all, light-assisted NO_2 sensors have paved a new path to achieve fast RT-recoverable NO_2 sensors. Finally, we graphically presented the gas-sensing characteristics such as recovery time, temperature, and sensitivity obtained from various reports in Fig. 23 to have an easy catch over the progress. In Fig. 23a, we have summarized the recovery time obtained through various strategies. Many bare MoS_2 NO_2 sensors either have incomplete recovery, or need to operate at high temperature for full recovery. Hence, we have few data points. The data revealed that NO_2 has high adsorption energy with MoS_2 at RT. Due to high adsorption energy, bare MoS_2 NO_2 sensors are suffered from incomplete or long recovery time at RT. The morphology controlled MoS_2 sensors have a good recovery but in a moderate temperature range. External thermal energy is needed to recover the MoS_2 sensors. MoS_2 heterostructures-based sensors have the mixed recovery time with different operating temperature depending on their partner materials and charge transfer mechanism. It is also observed that MoS_2 heterostructures NO_2 sensors have the comparatively less recovery time than the bare MoS_2 and morphology-driven NO_2 sensors due to faster separation of charges at RT and moderate temperature. Interestingly, light-assisted NO_2 sensors have the lowest recovery time with RT operation. Thus, light illumination has played a significant role in improving NO_2 sensors at RT. Photogenerated electrons and holes pairs crucially help in the desorption of the adsorbed NO_2 molecules. In Fig. 23b, we have concluded the various reports and summarize the gas-sensing factors. Graphical representation revealed MoS_2-based NO_2 sensors have a clear advantage over the traditional sensors in terms of temperature, cost and power. The statistics presented in the Fig. 23b has confirmed that NO_2 sensors based on MoS_2 can fill the performance gap shown in the Fig. 3. With traditional metal oxide sensors, we need high operating temperature up to 500 °C while MoS_2 sensors can easily operate at low temperature range with high sensor response and selectivity with low recovery time.

Acknowledgements The authors acknowledge the Department of Atomic Energy (DAE) under Project No. 34/20/09/2015/BRNS and also the Department of Physics, IIT Ropar for providing financial support and the research facility.

References

1. T.W. Ashenden, T.A. Mansfield, Extreme pollution sensitivity of grasses when SO_2 and NO_2 are present in the atmosphere together. Nature **273**(5658), 142–143 (1978). https://doi.org/10.1038/273142a0
2. L. Calderón-Garcidueñas, B. Azzarelli, H. Acuna, R. Garcia, T.M. Gambling et al., Air pollution and brain damage. Toxicol. Pathol. **30**(3), 373–389 (2002). https://doi.org/10.1080/01926230252929954
3. R.J. van der A, H.J. Eskes, K.F. Boersma, T.P.C. van Noije, M. Van Roozendael et al., Trends, seasonal variability and dominant NOx source derived from a ten-year record of NO_2 measured from space. J. Geophys. Res. Atmos. **113**(D4), 302 (2008). https://doi.org/10.1029/2007JD009021
4. J.G. Speight, Chapter one—inorganic chemicals in the environment, in ed. by J. Speight *Environmental Inorganic Chemistry for Engineers* (Butterworth-Heinemann, 2017), pp. 1–49. https://doi.org/10.1016/B978-0-12-849891-0.00001-1
5. D. Fowler, J.N. Cape, I.D. Leith, I.S. Paterson, J.W. Kinnaird et al., Rainfall acidity in northern Britain. Nature **297**(5865), 383–385 (1982). https://doi.org/10.1038/297383a0
6. N.M. Elsayed, Toxicity of nitrogen dioxide: an introduction. Toxicology **89**(3), 161–174 (1994). https://doi.org/10.1016/0300-483X(94)90096-5
7. J.A. Burney, The downstream air pollution impacts of the transition from coal to natural gas in the United States. Nat. Sustain. **3**(2), 152–160 (2020). https://doi.org/10.1038/s41893-019-0453-5
8. L. Meier, P. Tanskanen, L. Heng, G.H. Lee, F. Fraundorfer et al., PIXHAWK: a micro aerial vehicle design for

autonomous flight using onboard computer vision. Auton. Robots **33**(1), 21–39 (2012). https://doi.org/10.1007/s10514-012-9281-4

9. C. Li, L. Yu, W. He, Y. Cheng, G. Song, Development of local emissions rate model for light-duty gasoline vehicles: Beijing field data and patterns of emissions rates in EPA simulator. Transp. Res. Record. **2627**(1), 67–76 (2017). https://doi.org/10.3141/2627-08
10. A. Richter, J.P. Burrows, H. Nüß, C. Granier, U. Niemeier, Increase in tropospheric nitrogen dioxide over China observed from space. Nature **437**(7055), 129–132 (2005). https://doi.org/10.1038/nature04092
11. R.J. van der A, D.H.M.U. Peters, H. Eskes, K.F. Boersma, M. Van Roozendael et al., Detection of the trend and seasonal variation in tropospheric NO_2 over China. J. Geophys. Res. Atmos. **111**(D12), D12317 (2006). https://doi.org/10.1029/2005jd006594
12. P. Castellanos, K.F. Boersma, Reductions in nitrogen oxides over Europe driven by environmental policy and economic recession. Sci. Rep. **2**(1), 265 (2012). https://doi.org/10.1038/srep00265
13. P.K. Hopke, Contemporary threats and air pollution. Atmos. Environ. **43**(1), 87–93 (2009). https://doi.org/10.1016/j.atmosenv.2008.09.053
14. C. Zhang, C. Liu, Q. Hu, Z. Cai, W. Su et al., Satellite UV–Vis spectroscopy: implications for air quality trends and their driving forces in China during 2005–2017. Light Sci. Appl. **8**(1), 100 (2019). https://doi.org/10.1038/s41377-019-0210-6
15. R.G. Derwent, K. Nodopt, Long-range transport and deposition of acidic nitrogen species in north-west Europe. Nature **324**(6095), 356–358 (1986). https://doi.org/10.1038/324356a0
16. J.A. Bernstein, N. Alexis, C. Barnes, I.L. Bernstein, A. Nel et al., Health effects of air pollution. J. Allergy Clin. Immunol. **114**(5), 1116–1123 (2004). https://doi.org/10.1016/j.jaci.2004.08.030
17. D.J. Late, Y.-K. Huang, B. Liu, J. Acharya, S.N. Shirodkar et al., Sensing behavior of atomically thin-layered MoS_2 transistors. ACS Nano **7**(6), 4879–4891 (2013). https://doi.org/10.1021/nn400026u
18. K. Luo, R. Li, W. Li, Z. Wang, X. Ma et al., Acute effects of nitrogen dioxide on cardiovascular mortality in Beijing: an exploration of spatial heterogeneity and the district-specific predictors. Sci. Rep. **6**(1), 38328 (2016). https://doi.org/10.1038/srep38328
19. W.H. Organization, World health statistics 2016: monitoring health for the SDGs sustainable development goals (World Health Organization; 2016)
20. W.H. Organization, Guidelines for drinking-water quality (World Health Organization; 1993)
21. A. Hulanicki, S. Glab, F. Ingman, Chemical sensors: definitions and classification. Pure Appl. Chem. **63**(9), 1247–1250 (1991). https://doi.org/10.1351/pac199163091247
22. G.W. Hunter, L.-Y. Chen, P.G. Neudeck, D. Knight, C.-C. Liu et al, *Chemical Gas Sensors for Aeronautic and Space Applications* 2 (1998)
23. J. Guerrero-Ibáñez, S. Zeadally, J. Contreras-Castillo, Sensor technologies for intelligent transportation systems. Sensors **18**(4), 1212 (2018). https://doi.org/10.3390/s18041212
24. H. Long, L. Chan, A. Harley-Trochimczyk, L.E. Luna, Z. Tang et al., 3D MoS_2 aerogel for ultrasensitive NO_2 detection and its tunable sensing behavior. Adv. Mater. Interface **4**(16), 1700217 (2017). https://doi.org/10.1002/admi.201700217
25. B. Zhao, C.Y. Li, L.L. Liu, B. Zhou, Q.K. Zhang et al., Adsorption of gas molecules on Cu impurities embedded monolayer MoS_2: A first-principles study. Appl. Surf. Sci. **382**, 280–287 (2016). https://doi.org/10.1016/j.apsusc.2016.04.158
26. X. Chen, Y. Shen, P. Zhou, X. Zhong, G. Li et al., Bimetallic Au/Pd nanoparticles decorated ZnO nanowires for NO_2 detection. Sens. Actuators B Chem. **289**, 160–168 (2019). https://doi.org/10.1016/j.snb.2019.03.095
27. M. Yin, Y. Wang, L. Yu, H. Wang, Y. Zhu et al., Ag nanoparticles-modified Fe_2O_3@MoS_2 core-shell micro/nanocomposites for high-performance NO_2 gas detection at low temperature. J. Alloys Compd. **829**, 154471 (2020). https://doi.org/10.1016/j.jallcom.2020.154471
28. Y. Xia, J. Wang, J.-L. Xu, X. Li, D. Xie et al., Confined formation of ultrathin ZnO nanorods/reduced graphene oxide mesoporous nanocomposites for high-performance room-temperature NO_2 sensors. ACS Appl. Mater. Interfaces **8**(51), 35454–35463 (2016). https://doi.org/10.1021/acsami.6b12501
29. H. Tabata, Y. Sato, K. Oi, O. Kubo, M. Katayama, Bias- and gate-tunable gas sensor response originating from modulation in the Schottky barrier height of a graphene/MoS_2 van der Waals heterojunction. ACS Appl. Mater. Interfaces **10**(44), 38387–38393 (2018). https://doi.org/10.1021/acsami.8b14667
30. J. Li, Y. Lu, Q. Ye, M. Cinke, J. Han et al., Carbon nanotube sensors for gas and organic vapor detection. Nano Lett. **3**(7), 929–933 (2003). https://doi.org/10.1021/nl034220x
31. M. Donarelli, S. Prezioso, F. Perrozzi, F. Bisti, M. Nardone et al., Response to NO_2 and other gases of resistive chemically exfoliated MoS_2-based gas sensors. Sens. Actuators B Chem. **207**, 602–613 (2015). https://doi.org/10.1016/j.snb.2014.10.099
32. B. Cho, M.G. Hahm, M. Choi, J. Yoon, A.R. Kim et al., Charge-transfer-based gas sensing using atomic-layer MoS_2. Sci. Rep. **5**(1), 8052 (2015). https://doi.org/10.1038/srep08052
33. L. Yu, F. Guo, S. Liu, J. Qi, M. Yin et al., Hierarchical 3D flower-like MoS_2 spheres: post-thermal treatment in vacuum and their NO_2 sensing properties. Mater. Lett. **183**, 122–126 (2016). https://doi.org/10.1016/j.matlet.2016.07.086
34. H. Li, Z. Yin, Q. He, H. Li, X. Huang et al., Fabrication of single- and multilayer MoS_2 film-based field-effect

 https://doi.org/10.1007/s40820-020-00558-3

transistors for sensing NO at room temperature. Small **8**(1), 63–67 (2012). https://doi.org/10.1002/smll.201101016

35. S.-Y. Cho, S.J. Kim, Y. Lee, J.-S. Kim, W.-B. Jung et al., Highly enhanced gas adsorption properties in vertically aligned MoS_2 layers. ACS Nano **9**(9), 9314–9321 (2015). https://doi.org/10.1021/acsnano.5b04504
36. B. Liu, L. Chen, G. Liu, A.N. Abbas, M. Fathi et al., High-performance chemical sensing using Schottky-contacted chemical vapor deposition grown monolayer MoS_2 transistors. ACS Nano **8**(5), 5304–5314 (2014). https://doi.org/10.1021/nn5015215
37. W. Yuan, G. Shi, Graphene-based gas sensors. J. Mater. Chem. A **1**(35), 10078–10091 (2013). https://doi.org/10.1039/C3TA11774J
38. C. Soldano, A. Mahmood, E. Dujardin, Production, properties and potential of graphene. Carbon **48**(8), 2127–2150 (2010). https://doi.org/10.1016/j.carbon.2010.01.058
39. M. Zheng, K. Takei, B. Hsia, H. Fang, X. Zhang et al., Metal-catalyzed crystallization of amorphous carbon to graphene. Appl. Phys. Lett. **96**(6), 063110 (2010). https://doi.org/10.1063/1.3318263
40. J.H. Choi, J. Lee, M. Byeon, T.E. Hong, H. Park et al., Graphene-based gas sensors with high sensitivity and minimal sensor-to-sensor variation. ACS Appl. Nano Mater. **3**(3), 2257–2265 (2020). https://doi.org/10.1021/acsanm.9b02378
41. D. Li, R.B. Kaner, Graphene-based materials. Science **320**(5880), 1170–1171 (2008). https://doi.org/10.1126/science.1158180
42. Q. He, Z. Zeng, Z. Yin, H. Li, S. Wu et al., Fabrication of flexible MoS_2 thin-film transistor arrays for practical gas-sensing applications. Small **8**(19), 2994–2999 (2012). https://doi.org/10.1002/smll.201201224
43. K.S. Novoselov, A. Mishchenko, A. Carvalho, A.H. Castro-Neto, 2D materials and van der Waals heterostructures. Science **353**(6298), aac9439 (2016). https://doi.org/10.1126/science.aac9439
44. R. Mas-Ballesté, C. Gómez-Navarro, J. Gómez-Herrero, F. Zamora, 2D materials: to graphene and beyond. Nanoscale **3**(1), 20–30 (2011). https://doi.org/10.1039/C0NR00323A
45. H. Li, Q. Zhang, C.C.R. Yap, B.K. Tay, T.H.T. Edwin et al., From bulk to monolayer MoS_2: evolution of raman scattering. Adv. Funct. Mater. **22**(7), 1385–1390 (2012). https://doi.org/10.1002/adfm.201102111
46. N. Bertram, J. Cordes, Y.D. Kim, G. Ganteför, S. Gemming et al., Nanoplatelets made from MoS_2 and WS_2. Chem. Phys. Lett. **418**(1), 36–39 (2006). https://doi.org/10.1016/j.cplett.2005.10.046
47. B. Dubertret, T. Heine, M. Terrones, The rise of two-dimensional materials. Acc. Chem. Res. **48**(1), 1–2 (2015). https://doi.org/10.1021/ar5004434
48. Y. Han, M.-Y. Li, G.-S. Jung, M.A. Marsalis, Z. Qin et al., Sub-nanometre channels embedded in two-dimensional materials. Nat. Mater. **17**(2), 129–133 (2018). https://doi.org/10.1038/nmat5038
49. A. Gupta, T. Sakthivel, S. Seal, Recent development in 2D materials beyond graphene. Prog. Mater. Sci. **73**, 44–126 (2015). https://doi.org/10.1016/j.pmatsci.2015.02.002
50. K.F. Mak, C. Lee, J. Hone, J. Shan, T.F. Heinz, Atomically thin MoS_2: a new direct-gap semiconductor. Phys. Rev. Lett. **105**, 136805 (2010). https://doi.org/10.1103/PhysRevLett.105.136805
51. C. Mai, A. Barrette, Y. Yu, Y.G. Semenov, K.W. Kim et al., Many-body effects in valleytronics: direct measurement of valley lifetimes in single-layer MoS_2. Nano Lett. **14**(1), 202–206 (2014). https://doi.org/10.1021/nl403742j
52. J.R. Schaibley, H. Yu, G. Clark, P. Rivera, J.S. Ross et al., Valleytronics in 2D materials. Nat. Rev. Mater. **1**(11), 16055 (2016). https://doi.org/10.1038/natrevmats.2016.55
53. S.J. Kim, K. Choi, B. Lee, Y. Kim, B.H. Hong, Materials for flexible, stretchable electronics: graphene and 2D materials. Ann. Rev. Mater. Res. **45**(1), 63–84 (2015). https://doi.org/10.1146/annurev-matsci-070214-020901
54. D. Jariwala, V.K. Sangwan, D.J. Late, J.E. Johns, V.P. Dravid et al., Band-like transport in high mobility unencapsulated single-layer MoS_2 transistors. Appl. Phys. Lett. **102**(17), 173107 (2013). https://doi.org/10.1063/1.4803920
55. B. Chakraborty, H.S.S.R. Matte, A.K. Sood, C.N.R. Rao, Layer-dependent resonant Raman scattering of a few layer MoS_2. J. Raman Spectrosc. **44**(1), 92–96 (2013). https://doi.org/10.1002/jrs.4147
56. S.I. Khondaker, M.R. Islam, Bandgap engineering of MoS_2 flakes via oxygen plasma: a layer dependent study. J. Phys. Chem. C **120**(25), 13801–13806 (2016). https://doi.org/10.1021/acs.jpcc.6b03247
57. F. Schedin, A.K. Geim, S.V. Morozov, E.W. Hill, P. Blake et al., Detection of individual gas molecules adsorbed on graphene. Nat. Mater. **6**(9), 652–655 (2007). https://doi.org/10.1038/nmat1967
58. E.H. Hwang, S. Das Sarma, Acoustic phonon scattering limited carrier mobility in two-dimensional extrinsic graphene. Phys. Rev. B **77**(11), 115449 (2008). https://doi.org/10.1103/PhysRevB.77.115449
59. E.V. Castro, H. Ochoa, M.I. Katsnelson, R.V. Gorbachev, D.C. Elias et al., Limits on charge carrier mobility in suspended graphene due to flexural phonons. Phys. Rev. Lett. **105**(26), 266601 (2010). https://doi.org/10.1103/PhysRevLett.105.266601
60. S. Vadukumpully, J. Paul, N. Mahanta, S. Valiyaveettil, Flexible conductive graphene/poly(vinyl chloride) composite thin films with high mechanical strength and thermal stability. Carbon **49**(1), 198–205 (2011). https://doi.org/10.1016/j.carbon.2010.09.004
61. G. Ko, H.Y. Kim, J. Ahn, Y.M. Park, K.Y. Lee et al., Graphene-based nitrogen dioxide gas sensors. Curr. Appl. Phys. **10**(4), 1002–1004 (2010). https://doi.org/10.1016/j.cap.2009.12.024
62. S. Gupta Chatterjee, S. Chatterjee, A.K. Ray, A.K. Chakraborty, Graphene–metal oxide nanohybrids for toxic gas sensor: a review. Sens. Actuators B Chem. **221**, 1170–1181 (2015). https://doi.org/10.1016/j.snb.2015.07.070

63. J. Ma, M. Zhang, L. Dong, Y. Sun, Y. Su et al., Gas sensor based on defective graphene/pristine graphene hybrid towards high sensitivity detection of NO_2. AIP Adv. **9**(7), 075207 (2019). https://doi.org/10.1063/1.5099511
64. F. Yavari, N. Koratkar, Graphene-based chemical sensors. J. Phys. Chem. Lett. **3**(13), 1746–1753 (2012). https://doi.org/10.1021/jz300358t
65. Z. Yan, J. Lin, Z. Peng, Z. Sun, Y. Zhu et al., Toward the synthesis of wafer-scale single-crystal graphene on copper foils. ACS Nano **6**(10), 9110–9117 (2012). https://doi.org/10.1021/nn303352k
66. T.A. Land, T. Michely, R.J. Behm, J.C. Hemminger, G. Comsa, STM investigation of single layer graphite structures produced on Pt(111) by hydrocarbon decomposition. Surf. Sci. **264**(3), 261–270 (1992). https://doi.org/10.1016/0039-6028(92)90183-7
67. J. Coraux, A.T. N'Diaye, C. Busse, T. Michely, Structural coherency of graphene on Ir(111). Nano Lett. **8**(2), 565–570 (2008). https://doi.org/10.1021/nl0728874
68. W. Tian, W. Li, W. Yu, X. Liu, A review on lattice defects in graphene: types, generation, effects and regulation. Micromachines **8**(5), 163 (2017). https://doi.org/10.3390/mi8050163
69. A.K. Geim, K.S. Novoselov, The rise of graphene. Nat. Mater. **6**(3), 183–191 (2007). https://doi.org/10.1038/nmat1849
70. M. Chhowalla, H.S. Shin, G. Eda, L.-J. Li, K.P. Loh et al., The chemistry of two-dimensional layered transition metal dichalcogenide nanosheets. Nat. Chem. **5**(4), 263–275 (2013). https://doi.org/10.1038/nchem.1589
71. W. Choi, N. Choudhary, G.H. Han, J. Park, D. Akinwande et al., Recent development of two-dimensional transition metal dichalcogenides and their applications. Mater. Today **20**(3), 116–130 (2017). https://doi.org/10.1016/j.mattod.2016.10.002
72. S.-J. Choi, I.-D. Kim, Recent developments in 2D nanomaterials for chemiresistive-type gas sensors. Electron. Mater. Lett. **14**(3), 221–260 (2018). https://doi.org/10.1007/s13391-018-0044-z
73. A. Voshell, M. Terrones, M. Rana, Review of optical properties of two-dimensional transition metal dichalcogenides. SPIE 107540L (2018) https://doi.org/10.1117/12.2323132
74. T.C. Berkelbach, D.R. Reichman, Optical and excitonic properties of atomically thin transition-metal dichalcogenides. Annu. Rev. Condens. Matter Phys. **9**, 379–396 (2018). https://doi.org/10.1146/annurev-conmatphys-033117-054009
75. P. Xiao, J. Mao, K. Ding, W. Luo, W. Hu et al., Solution-processed 3D RGO–MoS_2/pyramid Si heterojunction for ultrahigh detectivity and ultra-broadband photodetection. Adv. Mater. **30**(31), 1801729 (2018). https://doi.org/10.1002/adma.201801729
76. J. Deng, L. Zong, M. Zhu, F. Liao, Y. Xie et al., MoS_2/HfO_2/silicon-on-insulator dual-photogating transistor with ambipolar photoresponsivity for high-resolution light wavelength detection. Adv. Funct. Mater. **29**(46), 1906242 (2019). https://doi.org/10.1002/adfm.201906242
77. N. Guo, L. Xiao, F. Gong, M. Luo, F. Wang et al., Light-driven WSe_2–ZnO junction field-effect transistors for high-performance photodetection. Adv. Sci. **7**(1), 1901637 (2020). https://doi.org/10.1002/advs.201901637
78. K.J. Berean, J.Z. Ou, T. Daeneke, B.J. Carey, E.P. Nguyen et al., 2D MoS_2 PDMS nanocomposites for NO_2 separation. Small **11**(38), 5035–5040 (2015). https://doi.org/10.1002/smll.201501129
79. H. Khan, A. Zavabeti, J.Z. Ou, T. Daeneke, Y. Li et al., Two dimensional tungsten oxide nanosheets with unprecedented selectivity and sensitivity to NO_2. 2017 IEEE Sensor 1–3 (2017). https://doi.org/10.1109/ICSENS.2017.8234283
80. X. Chen, X. Chen, Y. Han, C. Su, M. Zeng et al., Two-dimensional $MoSe_2$ nanosheets via liquid-phase exfoliation for high-performance room temperature NO_2 gas sensors. Nanotechnology **30**(44), 445503 (2019). https://doi.org/10.1088/1361-6528/ab35ec
81. Y. Han, Y. Liu, C. Su, S. Wang, H. Li et al., Interface engineered WS_2/ZnS heterostructures for sensitive and reversible NO_2 room temperature sensing. Sens. Actuators B Chem. **296**, 126666 (2019). https://doi.org/10.1016/j.snb.2019.126666
82. Z. Yang, C. Su, S. Wang, Y. Han, X. Chen et al., Highly sensitive NO_2 gas sensors based on hexagonal SnS_2 nanoplates operating at room temperature. Nanotechnology **31**(7), 075501 (2019). https://doi.org/10.1088/1361-6528/ab5271
83. R. Guo, Y. Han, C. Su, X. Chen, M. Zeng et al., Ultrasensitive room temperature NO_2 sensors based on liquid phase exfoliated WSe_2 nanosheets. Sens. Actuators B Chem. **300**, 127013 (2019). https://doi.org/10.1016/j.snb.2019.127013
84. S.S. Varghese, S.H. Varghese, S. Swaminathan, K.K. Singh, V. Mittal, Two-dimensional materials for sensing: graphene and beyond. Electronics **4**(3), 651–687 (2015). https://doi.org/10.3390/electronics4030651
85. M. Kumar, A.V. Agrawal, M. Moradi, R. Yousefi, Chapter 6 - Nanosensors for gas sensing applications, in eds. by A. Abdeltif, A.A. Assadi, P. Nguyen-Tri, et al., *Nanomaterials for Air Remediation* (Elsevier, 2020), pp. 107–130. https://doi.org/10.1016/B978-0-12-818821-7.00006-3
86. S. Yang, C. Jiang, S.-H. Wei, Gas sensing in 2D materials. Appl. Phys. Rev. **4**(2), 021304 (2017). https://doi.org/10.1063/1.4983310
87. K.Y. Ko, J.-G. Song, Y. Kim, T. Choi, S. Shin et al., Improvement of gas-sensing performance of large-area tungsten disulfide nanosheets by surface functionalization. ACS Nano **10**(10), 9287–9296 (2016). https://doi.org/10.1021/acsnano.6b03631
88. H. Fang, S. Chuang, T.C. Chang, K. Takei, T. Takahashi et al., High-performance single layered WSe_2 p-FETs with chemically doped contacts. Nano Lett. **12**(7), 3788–3792 (2012). https://doi.org/10.1021/nl301702r
89. Z. Feng, Y. Xie, J. Chen, Y. Yu, S. Zheng et al., Highly sensitive $MoTe_2$ chemical sensor with fast recovery rate through gate biasing. 2D Mater. **4**(2), 025018 (2017). https://doi.org/10.1021/nl301702r

 https://doi.org/10.1007/s40820-020-00558-3

90. B. Cho, A.R. Kim, D.J. Kim, H.-S. Chung, S.Y. Choi et al., Two-dimensional atomic-layered alloy junctions for high-performance wearable chemical sensor. ACS Appl. Mater. Interfaces **8**(30), 19635–19642 (2016). https://doi.org/10.1021/acsami.6b05943
91. K.P. Gattu, K. Ghule, A.A. Kashale, V.B. Patil, D.M. Phase et al., Bio-green synthesis of Ni-doped tin oxide nanoparticles and its influence on gas sensing properties. RSC Adv. **5**(89), 72849–72856 (2015). https://doi.org/10.1039/C5RA13513C
92. D. Lembke, S. Bertolazzi, A. Kis, Single-layer MoS_2 electronics. Acc. Chem. Res. **48**(1), 100–110 (2015). https://doi.org/10.1021/ar500274q
93. P. Raybaud, J. Hafner, G. Kresse, S. Kasztelan, H. Toulhoat, Structure, energetics, and electronic properties of the surface of a promoted MoS_2 catalyst: an ab initio local density functional study. J. Catal. **190**(1), 128–143 (2000). https://doi.org/10.1006/jcat.1999.2743
94. W. Yin, J. Yu, F. Lv, L. Yan, L.R. Zheng et al., Functionalized nano-MoS_2 with peroxidase catalytic and near-infrared photothermal activities for safe and synergetic wound antibacterial applications. ACS Nano **10**(12), 11000–11011 (2016). https://doi.org/10.1021/acsnano.6b05810
95. G. Eda, T. Fujita, H. Yamaguchi, D. Voiry, M. Chen et al., Coherent atomic and electronic heterostructures of single-layer MoS_2. ACS Nano **6**(8), 7311–7317 (2012). https://doi.org/10.1021/nn302422x
96. K. Kalantar-zadeh, J.Z. Ou, Biosensors based on two-dimensional MoS_2. ACS Sens. **1**(1), 5–16 (2016). https://doi.org/10.1021/acssensors.5b00142
97. F. Wypych, R. Schöllhorn, 1T-MoS_2, a new metallic modification of molybdenum disulfide. J. Chem. Soc. Chem. Commun. (1992). https://doi.org/10.1039/C39920001386
98. A. Splendiani, L. Sun, Y. Zhang, T. Li, J. Kim et al., Emerging photoluminescence in monolayer MoS_2. Nano Lett. **10**(4), 1271–1275 (2010). https://doi.org/10.1021/nl903868w
99. G. Eda, H. Yamaguchi, D. Voiry, T. Fujita, M. Chen et al., Photoluminescence from chemically exfoliated MoS_2. Nano Lett. **11**(12), 5111–5116 (2011). https://doi.org/10.1021/nl201874w
100. W. Zhao, R.M. Ribeiro, G. Eda, Electronic structure and optical signatures of semiconducting transition metal dichalcogenide nanosheets. Acc. Chem. Res. **48**(1), 91–99 (2015). https://doi.org/10.1021/ar500303m
101. S. Zhang, J. Liu, K.H. Ruiz, R. Tu, M. Yang et al., Morphological evolution of vertically standing molybdenum disulfide nanosheets by chemical vapor deposition. Materials **11**(4), 631 (2018). https://doi.org/10.3390/ma11040631
102. X. Liu, T. Xu, X. Wu, Z. Zhang, J. Yu et al., Top–down fabrication of sub-nanometre semiconducting nanoribbons derived from molybdenum disulfide sheets. Nat. Commun. **4**(1), 1776 (2013). https://doi.org/10.1038/ncomms2803
103. B. Cho, J. Yoon, S.K. Lim, A.R. Kim, D.-H. Kim et al., Chemical sensing of 2D Graphene/MoS_2 heterostructure device. ACS Appl. Mater. Interfaces **7**(30), 16775–16780 (2015). https://doi.org/10.1021/acsami.5b04541
104. Z. Yin, H. Li, H. Li, L. Jiang, Y. Shi et al., Single-layer MoS_2 phototransistors. ACS Nano **6**(1), 74–80 (2012). https://doi.org/10.1021/nn2024557
105. R. Ganatra, Q. Zhang, Few-layer MoS_2: a promising layered semiconductor. ACS Nano **8**(5), 4074–4099 (2014). https://doi.org/10.1021/nn405938z
106. K. Kaasbjerg, K.S. Thygesen, K.W. Jacobsen, Phonon-limited mobility in n-type single-layer MoS_2 from first principles. Phys. Rev. B **85**(11), 115317 (2012). https://doi.org/10.1103/PhysRevB.85.115317
107. C. Lee, H. Yan, L.E. Brus, T.F. Heinz, J. Hone et al., Anomalous lattice vibrations of single- and few-layer MoS_2. ACS Nano **4**(5), 2695–2700 (2010). https://doi.org/10.1021/nn1003937
108. A.V. Agrawal, N. Kumar, S. Venkatesan, A. Zakhidov, C. Manspeaker et al., Controlled growth of MoS_2 flakes from in-plane to edge-enriched 3d network and their surface-energy studies. ACS Appl. Nano Mater. **1**(5), 2356–2367 (2018). https://doi.org/10.1021/acsanm.8b00467
109. B. Chakraborty, A. Bera, D.V.S. Muthu, S. Bhowmick, U.V. Waghmare et al., Symmetry-dependent phonon renormalization in monolayer MoS_2 transistor. Phys. Rev. B **85**(16), 161403 (2012). https://doi.org/10.1103/PhysRevB.85.161403
110. Y.K. Hong, G. Yoo, J. Kwon, S. Hong, W.G. Song et al., High performance and transparent multilayer MoS_2 transistors: tuning Schottky barrier characteristics. AIP Adv. **6**(5), 055026 (2016). https://doi.org/10.1063/1.4953062
111. S. Das, R. Gulotty, A.V. Sumant, A. Roelofs, All two-dimensional, flexible, transparent, and thinnest thin film transistor. Nano Lett. **14**(5), 2861–2866 (2014). https://doi.org/10.1021/nl5009037
112. Q. Zhang, W. Bao, A. Gong, T. Gong, D. Ma et al., A highly sensitive, highly transparent, gel-gated MoS_2 phototransistor on biodegradable nanopaper. Nanoscale **8**(29), 14237–14242 (2016). https://doi.org/10.1039/C6NR01534D
113. Z.-T. Shi, W. Kang, J. Xu, Y.-W. Sun, M. Jiang et al., Hierarchical nanotubes assembled from MoS_2-carbon monolayer sandwiched superstructure nanosheets for high-performance sodium ion batteries. Nano Energy **22**, 27–37 (2016). https://doi.org/10.1016/j.nanoen.2016.02.009
114. J. Kang, H. Sahin, F.M. Peeters, Mechanical properties of monolayer sulphides: a comparative study between MoS_2, HfS_2 and TiS_3. Phys. Chem. Chem. Phys. **17**(41), 27742–27749 (2015). https://doi.org/10.1039/C5CP04576B
115. J. Pu, Y. Yomogida, K.-K. Liu, L.-J. Li, Y. Iwasa et al., Highly flexible MoS_2 thin-film transistors with ion gel dielectrics. Nano Lett. **12**(8), 4013–4017 (2012). https://doi.org/10.1021/nl301335q
116. B. Radisavljevic, A. Radenovic, J. Brivio, V. Giacometti, A. Kis, Single-layer MoS_2 transistors. Nat. Nanotechnol. **6**(3), 147–150 (2011). https://doi.org/10.1038/nnano.2010.279
117. Q. Yue, Z. Shao, S. Chang, J. Li, Adsorption of gas molecules on monolayer MoS_2 and effect of applied electric field. Nanoscale Res. Lett. **8**(1), 425 (2013). https://doi.org/10.1186/1556-276x-8-425

118. H. Long, A. Harley-Trochimczyk, T. Pham, Z. Tang, T. Shi et al., High surface area MoS_2/graphene hybrid aerogel for ultrasensitive NO_2 detection. Adv. Funct. Mater. **26**(28), 5158–5165 (2016). https://doi.org/10.1002/adfm.201601562
119. R. Kumar, N. Goel, M. Kumar, UV-activated MoS_2 based fast and reversible NO_2 sensor at room temperature. ACS Sens. **2**(11), 1744–1752 (2017). https://doi.org/10.1021/acssensors.7b00731
120. A.V. Agrawal, R. Kumar, S. Venkatesan, A. Zakhidov, G. Yang et al., Photoactivated mixed in-plane and edge-enriched p-type MoS_2 flake-based NO_2 sensor working at room temperature. ACS Sens. **3**(5), 998–1004 (2018). https://doi.org/10.1021/acssensors.8b00146
121. Y. Zhou, C. Zou, X. Lin, Y. Guo, UV light activated NO_2 gas sensing based on Au nanoparticles decorated few-layer MoS_2 thin film at room temperature. Appl. Phys. Lett. **113**(8), 082103 (2018)
122. J. Guo, R. Wen, J. Zhai, Z.L. Wang, Enhanced NO_2 gas sensing of a single-layer MoS_2 by photogating and piezo-phototronic effects. Sci. Bull. **64**(2), 128–135 (2019). https://doi.org/10.1016/j.scib.2018.12.009
123. Y. Xia, C. Hu, S. Guo, L. Zhang, M. Wang et al., Sulfur-vacancy-enriched MoS_2 nanosheets based heterostructures for near-infrared optoelectronic NO_2 sensing. ACS Appl. Nano Mater. **3**(1), 665–673 (2020). https://doi.org/10.1021/acsanm.9b02180
124. J. Lu, J.H. Lu, H. Liu, B. Liu, L. Gong et al., Microlandscaping of Au nanoparticles on few-layer MoS_2 films for chemical sensing. Small **11**(15), 1792–1800 (2015). https://doi.org/10.1002/smll.201402591
125. A.J. Cohen, P. Mori-Sánchez, W. Yang, Challenges for density functional theory. Chem. Rev. **112**(1), 289–320 (2012). https://doi.org/10.1021/cr200107z
126. R.O. Jones, Density functional theory: its origins, rise to prominence, and future. Rev. Mod. Phys. **87**(3), 897–923 (2015). https://doi.org/10.1103/RevModPhys.87.897
127. S. Tang, Z. Cao, Adsorption of nitrogen oxides on graphene and graphene oxides: insights from density functional calculations. J. Chem. Phys. **134**(4), 044710 (2011). https://doi.org/10.1063/1.3541249
128. D.I. Son, B.W. Kwon, D.H. Park, W.-S. Seo, Y. Yi et al., Emissive ZnO–graphene quantum dots for white-light-emitting diodes. Nat. Nanotechnol. **7**(7), 465–471 (2012). https://doi.org/10.1038/nnano.2012.71
129. T.S. Sreeprasad, A.A. Rodriguez, J. Colston, A. Graham, E. Shishkin et al., Electron-tunneling modulation in percolating network of graphene quantum dots: fabrication, phenomenological understanding, and humidity/pressure sensing applications. Nano Lett. **13**(4), 1757–1763 (2013). https://doi.org/10.1021/nl4003443
130. L.-L. Li, J. Ji, R. Fei, C.-Z. Wang, Q. Lu et al., A facile microwave avenue to electrochemiluminescent two-color graphene quantum dots. Adv. Funct. Mater. **22**(14), 2971–2979 (2012). https://doi.org/10.1002/adfm.201200166
131. J. Kong, N.R. Franklin, C. Zhou, M.G. Chapline, S. Peng et al., Nanotube molecular wires as chemical sensors. Science **287**(5453), 622–625 (2000). https://doi.org/10.1126/science.287.5453.622
132. S. Chopra, K. McGuire, N. Gothard, A.M. Rao, A. Pham, Selective gas detection using a carbon nanotube sensor. Appl. Phys. Lett. **83**(11), 2280–2282 (2003). https://doi.org/10.1063/1.1610251
133. O.K. Varghese, D. Gong, M. Paulose, K.G. Ong, C.A. Grimes, Hydrogen sensing using titania nanotubes. Sens. Actuators B Chem. **93**(1), 338–344 (2003). https://doi.org/10.1016/S0925-4005(03)00222-3
134. S. Wang, D. Huang, S. Xu, W. Jiang, T. Wang et al., Two-dimensional NiO nanosheets with enhanced room temperature NO_2 sensing performance via Al doping. Phys. Chem. Chem. Phys. **19**(29), 19043–19049 (2017). https://doi.org/10.1039/C7CP03259E
135. X. Chen, S. Wang, C. Su, Y. Han, C. Zou et al., Two-dimensional Cd-doped porous Co_3O_4 nanosheets for enhanced room-temperature NO_2 sensing performance. Sens. Actuators B Chem. **305**, 127393 (2020). https://doi.org/10.1016/j.snb.2019.127393
136. N. Huo, S. Yang, Z. Wei, S.-S. Li, J.-B. Xia et al., Photoresponsive and gas sensing field-effect transistors based on multilayer WS_2 nanoflakes. Sci. Rep. **4**(1), 5209 (2014). https://doi.org/10.1038/srep05209
137. B. Li, S. Yang, N. Huo, Y. Li, J. Yang et al., Growth of large area few-layer or monolayer MoS_2 from controllable MoO_3 nanowire nuclei. RSC Adv. **4**(50), 26407–26412 (2014). https://doi.org/10.1039/C4RA01632G
138. Y.-H. Zhang, Y.-B. Chen, K.-G. Zhou, C.-H. Liu, J. Zeng et al., Improving gas sensing properties of graphene by introducing dopants and defects: a first-principles study. Nanotechnology **20**(18), 185504 (2009). https://doi.org/10.1088/0957-484/20/18/185504
139. G. Liu, Y. Lin, Nanomaterial labels in electrochemical immunosensors and immunoassays. Talanta **74**(3), 308–317 (2007). https://doi.org/10.1016/j.talanta.2007.10.014
140. G. Aragay, F. Pino, A. Merkoçi, Nanomaterials for sensing and destroying pesticides. Chem. Rev. **112**(10), 5317–5338 (2012). https://doi.org/10.1021/cr300020c
141. D. Grieshaber, R. MacKenzie, J. Vörös, E. Reimhult, Electrochemical biosensors-sensor principles and architectures. Sensors **8**(3), 1400–1458 (2008). https://doi.org/10.3390/s80314000
142. K. Saha, S.S. Agasti, C. Kim, X. Li, V.M. Rotello, Gold nanoparticles in chemical and biological sensing. Chem. Rev. **112**(5), 2739–2779 (2012). https://doi.org/10.1021/cr2001178
143. C. Zou, J. Hu, Y. Su, F. Shao, Z. Tao et al., Three-dimensional Fe_3O_4@reduced graphene oxide heterojunctions for high-performance room-temperature NO_2 sensors. Front. Mater. **6**, 195 (2019). https://doi.org/10.3389/fmats.2019.00195
144. R. Kumar, O. Al-Dossary, G. Kumar, A. Umar, Zinc oxide nanostructures for NO_2 gas-sensor applications: a

 https://doi.org/10.1007/s40820-020-00558-3

review. Nano Micro Lett. **7**(2), 97–120 (2015). https://doi.org/10.1007/s40820-014-0023-3

145. J. Xu, Y.A. Shun, Q. Pan, J. Qin, Sensing characteristics of double layer film of ZnO. Sens. Actuators B Chem. **66**(1), 161–163 (2000). https://doi.org/10.1016/S0925-4005(00)00327-0
146. J.-H. Kim, A. Mirzaei, H.W. Kim, S.S. Kim, Low-voltage-driven sensors based on ZnO nanowires for room-temperature detection of NO_2 and CO gases. ACS Appl. Mater. Interfaces **11**(27), 24172–24183 (2019). https://doi.org/10.1021/acsami.9b07208
147. J. Zhang, Z. Qin, D. Zeng, C. Xie, Metal-oxide-semiconductor based gas sensors: screening, preparation, and integration. Phys. Chem. Chem. Phys. **19**(9), 6313–6329 (2017). https://doi.org/10.1039/C6CP07799D
148. M.M. Arafat, A.S.M.A. Haseeb, S.A. Akbar, 13.08 - Developments in semiconducting oxide-based gas-sensing materials, in by eds. S. Hashmi, G.F. Batalha, C.J. Van Tyne, et al., *Comprehensive Materials Processing* (Elsevier, 2014), pp. 205–219. https://doi.org/10.1016/B978-0-08-096532-1.01307-8
149. V. Krivetsky, A. Ponzoni, E. Comini, M. Rumyantseva, A. Gaskov, Selective modified SnO_2-based materials for gas sensors arrays. Procedia Chem. **1**(1), 204–207 (2009). https://doi.org/10.1016/j.proche.2009.07.051
150. E. Comini, G. Faglia, G. Sberveglieri, Z. Pan, Z.L. Wang, Stable and highly sensitive gas sensors based on semiconducting oxide nanobelts. Appl. Phys. Lett. **81**(10), 1869–1871 (2002). https://doi.org/10.1063/1.1504867
151. J. Hao, D. Zhang, Q. Sun, S. Zheng, J. Sun et al., Hierarchical SnS_2/SnO_2 nanoheterojunctions with increased active-sites and charge transfer for ultrasensitive NO_2 detection. Nanoscale **10**(15), 7210–7217 (2018). https://doi.org/10.1039/C8NR01379A
152. M.D. Ganji, N. Sharifi, M. Ghorbanzadeh Ahangari, A. Khosravi, Density functional theory calculations of hydrogen molecule adsorption on monolayer molybdenum and tungsten disulfide. Phys. E Low Dimens. Syst. Nanostruct. **57**, 28–34 (2014). https://doi.org/10.1016/j.physe.2013.10.039
153. M. Hijazi, V. Stambouli, M. Rieu, G. Tournier, C. Pijolat et al., Sensitive and selective ammonia gas sensor based on molecularly modified SnO_2. Multidiscip. Digit. Publ. Inst. Proc. **1**(4), 399 (2017). https://doi.org/10.3390/proceedings1040399
154. Y. Zhong, W. Li, X. Zhao, X. Jiang, S. Lin et al., High-response room-temperature NO_2 sensor and ultrafast humidity sensor based on SnO_2 with rich oxygen vacancy. ACS Appl. Mater. Interfaces **11**(14), 13441–13449 (2019). https://doi.org/10.1021/acsami.9b01737
155. T. Zhang, S. Mubeen, N.V. Myung, M.A. Deshusses, Recent progress in carbon nanotube-based gas sensors. Nanotechnology **19**(33), 332001 (2008). https://doi.org/10.1088/0957-4484/19/33/332001
156. H. Choi, J.S. Choi, J.-S. Kim, J.-H. Choe, K.H. Chung et al., Flexible and transparent gas molecule sensor integrated with sensing and heating graphene layers. Small **10**(18), 3685–3691 (2014). https://doi.org/10.1002/smll.201400434
157. Z. Zanolli, J.C. Charlier, Defective carbon nanotubes for single-molecule sensing. Phys. Rev. B **80**(15), 155447 (2009). https://doi.org/10.1103/PhysRevB.80.155447
158. S. Santucci, S. Picozzi, F.D. Gregorio, L. Lozzi, C. Cantalini et al., NO_2 and CO gas adsorption on carbon nanotubes: Experiment and theory. J. Chem. Phys. **119**(20), 10904–10910 (2003). https://doi.org/10.1063/1.1619948
159. H. Xu, X. Chen, J. Zhang, J. Wang, B. Cao et al., NO_2 gas sensing with SnO_2–ZnO/PANI composite thick film fabricated from porous nanosolid. Sens. Actuators B Chem. **176**, 166–173 (2013). https://doi.org/10.1016/j.snb.2012.09.060
160. J. Zhang, S. Wang, Y. Wang, Y. Wang, B. Zhu et al., NO_2 sensing performance of SnO_2 hollow-sphere sensor. Sens. Actuators B Chem. **135**(2), 610–617 (2009). https://doi.org/10.1016/j.snb.2008.09.026
161. Y. Xiao, Q. Yang, Z. Wang, R. Zhang, Y. Gao et al., Improvement of NO_2 gas sensing performance based on discoid tin oxide modified by reduced graphene oxide. Sens. Actuators B Chem. **227**, 419–426 (2016). https://doi.org/10.1016/j.snb.2015.11.051
162. M. Kumar, A. Kumar, A.C. Abhyankar, Influence of texture coefficient on surface morphology and sensing properties of W-doped nanocrystalline tin oxide thin films. ACS Appl. Mater. Interfaces **7**(6), 3571–3580 (2015). https://doi.org/10.1021/am507397z
163. Y.-J. Choi, I.-S. Hwang, J.-G. Park, K.J. Choi, J.-H. Park et al., Novel fabrication of a SnO_2 nanowire gas sensor with high sensitivity. Nanotechnology **19**(9), 095508 (2008). https://doi.org/10.1088/0957-4484/19/9/095508
164. W.-S. Kim, B.-S. Lee, D.-H. Kim, H.-C. Kim, W.-R. Yu et al., SnO_2 nanotubes fabricated using electrospinning and atomic layer deposition and their gas sensing performance. Nanotechnology **21**(24), 245605 (2010). https://doi.org/10.1088/0957-4484/21/24/245605
165. R. Leghrib, A. Felten, J.J. Pireaux, E. Llobet, Gas sensors based on doped-CNT/SnO_2 composites for NO_2 detection at room temperature. Thin Solid Films **520**(3), 966–970 (2011). https://doi.org/10.1016/j.tsf.2011.04.186
166. Z. Wang, Y. Zhang, S. Liu, T. Zhang, Preparation of Ag nanoparticles-SnO_2 nanoparticles-reduced graphene oxide hybrids and their application for detection of NO_2 at room temperature. Sens. Actuators B Chem. **222**, 893–903 (2016). https://doi.org/10.1016/j.snb.2015.09.027
167. S.H. Mohamed, SnO_2 dendrites–nanowires for optoelectronic and gas sensing applications. J. Alloys Compd. **510**(1), 119–124 (2012). https://doi.org/10.1016/j.jallcom.2011.09.006
168. S. Liu, Z. Wang, Y. Zhang, J. Li, T. Zhang, Sulfonated graphene anchored with tin oxide nanoparticles for detection of nitrogen dioxide at room temperature with enhanced sensing performances. Sens. Actuators B Chem. **228**, 134–143 (2016). https://doi.org/10.1016/j.snb.2016.01.023
169. Z. Zhang, M. Xu, L. Liu, X. Ruan, J. Yan et al., Novel SnO_2@ZnO hierarchical nanostructures for highly sensitive and selective NO_2 gas sensing. Sens. Actuators B Chem. **257**, 714–727 (2018). https://doi.org/10.1016/j.snb.2017.10.190

170. V.V. Quang, N.V. Dung, N.S. Trong, N.D. Hoa, N.V. Duy et al., Outstanding gas-sensing performance of graphene/SnO_2 nanowire Schottky junctions. Appl. Phys. Lett. **105**(1), 013107 (2014). https://doi.org/10.1063/1.4887486
171. A. Sharma, M. Tomar, V. Gupta, WO_3 nanoclusters–SnO_2 film gas sensor heterostructure with enhanced response for NO_2. Sens. Actuators B Chem. **176**, 675–684 (2013). https://doi.org/10.1016/j.snb.2012.09.094
172. J.-H. Kim, A. Katoch, S.-H. Kim, S.S. Kim, Chemiresistive sensing behavior of SnO_2 (n)–Cu_2O (p) core–shell nanowires. ACS Appl. Mater. Interfaces **7**(28), 15351–15358 (2015). https://doi.org/10.1021/acsami.5b03224
173. J. Sun, P. Sun, D. Zhang, J. Xu, X. Liang et al., Growth of SnO_2 nanowire arrays by ultrasonic spray pyrolysis and their gas sensing performance. RSC Adv. **4**(82), 43429–43435 (2014). https://doi.org/10.1039/C4RA05682E
174. Y.J. Kwon, S.Y. Kang, P. Wu, Y. Peng, S.S. Kim et al., Selective improvement of NO_2 gas sensing behavior in SnO_2 nanowires by ion-beam irradiation. ACS Appl. Mater. Interfaces **8**(21), 13646–13658 (2016). https://doi.org/10.1021/acsami.6b01619
175. J.Z. Ou, W. Ge, B. Carey, T. Daeneke, A. Rotbart et al., Physisorption-based charge transfer in two-dimensional SnS_2 for selective and reversible NO_2 gas sensing. ACS Nano **9**(10), 10313–10323 (2015). https://doi.org/10.1021/acsnano.5b04343
176. T. Wang, J. Hao, S. Zheng, Q. Sun, D. Zhang et al., Highly sensitive and rapidly responding room-temperature NO_2 gas sensors based on WO_3 nanorods/sulfonated graphene nanocomposites. Nano Res. **11**(2), 791–803 (2018). https://doi.org/10.1007/s12274-017-1688-y
177. H.W. Kim, H.G. Na, Y.J. Kwon, S.Y. Kang, M.S. Choi et al., Microwave-assisted synthesis of graphene–SnO_2 nanocomposites and their applications in gas sensors. ACS Appl. Mater. Interfaces **9**(37), 31667–31682 (2017). https://doi.org/10.1021/acsami.7b02533
178. J. Partridge, M. Field, J. Peng, A. Sadek, K. Kalantar-Zadeh et al., Nanostructured SnO_2 films prepared from evaporated Sn and their application as gas sensors. Nanotechnology **19**(12), 125504 (2008). https://doi.org/10.1088/0957-4484/19/12/125504
179. S. Liu, Z. Wang, Y. Zhang, C. Zhang, T. Zhang, High performance room temperature NO_2 sensors based on reduced graphene oxide-multiwalled carbon nanotubes-tin oxide nanoparticles hybrids. Sens. Actuators B Chem. **211**, 318–324 (2015). https://doi.org/10.1016/j.snb.2015.01.127
180. H. Zhang, Y. Wang, X. Zhu, Y. Li, W. Cai, Bilayer Au nanoparticle-decorated WO_3 porous thin films: on-chip fabrication and enhanced NO_2 gas sensing performances with high selectivity. Sens. Actuators B Chem. **280**, 192–200 (2019). https://doi.org/10.1016/j.snb.2018.10.065
181. I. Kortidis, H.C. Swart, S.S. Ray, D.E. Motaung, Characteristics of point defects on the room temperature ferromagnetic and highly NO_2 selectivity gas sensing of p-type Mn_3O_4 nanorods. Sens. Actuators B Chem. **285**, 92–107 (2019). https://doi.org/10.1016/j.snb.2019.01.007
182. S. Zhao, Y. Shen, P. Zhou, X. Zhong, C. Han et al., Design of Au@WO_3 core–shell structured nanospheres for ppb-level NO_2 sensing. Sens. Actuators B Chem. **282**, 917–926 (2019). https://doi.org/10.1016/j.snb.2018.11.142
183. Y.H. Navale, S.T. Navale, F.J. Stadler, N.S. Ramgir, V.B. Patil, Enhanced NO_2 sensing aptness of ZnO nanowire/CuO nanoparticle heterostructure-based gas sensors. Ceram. Int. **45**(2, Part A), 1513–1522 (2019). https://doi.org/10.1016/j.ceramint.2018.10.022
184. Y. Song, F. Chen, Y. Zhang, S. Zhang, F. Liu et al., Fabrication of highly sensitive and selective room-temperature nitrogen dioxide sensors based on the ZnO nanoflowers. Sens. Actuators B Chem. **287**, 191–198 (2019). https://doi.org/10.1016/j.snb.2019.01.146
185. R.K. Sonker, B.C. Yadav, V. Gupta, M. Tomar, Fabrication and characterization of ZnO-TiO_2-PANI (ZTP) micro/nanoballs for the detection of flammable and toxic gases. J. Hazard. Mater. **370**, 126–137 (2019). https://doi.org/10.1016/j.jhazmat.2018.10.016
186. H.-Y. Lee, Y.-C. Heish, C.-T. Lee, High sensitivity detection of nitrogen oxide gas at room temperature using zinc oxide-reduced graphene oxide sensing membrane. J. Alloys Compd. **773**, 950–954 (2019). https://doi.org/10.1016/j.jallcom.2018.09.290
187. M.S. Choi, J.H. Bang, A. Mirzaei, W. Oum, H.G. Na et al., Promotional effects of ZnO-branching and Au-functionalization on the surface of SnO_2 nanowires for NO_2 sensing. J. Alloys Compd. **786**, 27–39 (2019). https://doi.org/10.1016/j.jallcom.2019.01.311
188. H. Ma, L. Yu, X. Yuan, Y. Li, C. Li et al., Room temperature photoelectric NO_2 gas sensor based on direct growth of walnut-like In_2O_3 nanostructures. J. Alloys Compd. **782**, 1121–1126 (2019). https://doi.org/10.1016/j.jallcom.2018.12.180
189. A. Giampiccolo, D.M. Tobaldi, S.G. Leonardi, B.J. Murdoch, M.P. Seabra et al., Sol gel graphene/TiO_2 nanoparticles for the photocatalytic-assisted sensing and abatement of NO_2. Appl. Catal. B Environ. **243**, 183–194 (2019). https://doi.org/10.1016/j.apcatb.2018.10.032
190. M. Penza, R. Rossi, M. Alvisi, G. Cassano, M.A. Signore et al., Pt- and Pd-nanoclusters functionalized carbon nanotubes networked films for sub-ppm gas sensors. Sens. Actuators B Chem. **135**(1), 289–297 (2008). https://doi.org/10.1016/j.snb.2008.08.024
191. M.G. Chung, D.H. Kim, H.M. Lee, T. Kim, J.H. Choi et al., Highly sensitive NO_2 gas sensor based on ozone treated graphene. Sens. Actuators B Chem. **166–167**, 172–176 (2012). https://doi.org/10.1016/j.snb.2012.02.036
192. H.Y. Jeong, D.-S. Lee, H.K. Choi, D.H. Lee, J.-E. Kim et al., Flexible room-temperature NO_2 gas sensors based on carbon nanotubes/reduced graphene hybrid films. Appl. Phys. Lett. **96**(21), 213105 (2010). https://doi.org/10.1063/1.3432446
193. H. Zhang, Q. Li, J. Huang, Y. Du, S.C. Ruan, Reduced graphene oxide/Au nanocomposite for NO_2 sensing at low operating temperature. Sensors **16**(7), 1152 (2016). https://doi.org/10.3390/s16071152

 https://doi.org/10.1007/s40820-020-00558-3

194. X. Liu, J. Cui, J. Sun, X. Zhang, 3D graphene aerogel-supported SnO_2 nanoparticles for efficient detection of NO_2. RSC Adv. **4**(43), 22601–22605 (2014). https://doi.org/10.1039/C4RA02453B
195. A. Aziz, N. Tiwale, S.A. Hodge, S.J. Attwood, G. Divitini et al., Core–shell electrospun polycrystalline ZnO nanofibers for ultra-sensitive NO_2 Gas sensing. ACS Appl. Mater. Interfaces **10**(50), 43817–43823 (2018). https://doi.org/10.1021/acsami.8b17149
196. N. Ramgir, R. Bhusari, N.S. Rawat, S.J. Patil, A.K. Debnath et al., TiO_2/ZnO heterostructure nanowire based NO_2 sensor. Mater. Sci. Semicond. Process. **106**, 104770 (2020). https://doi.org/10.1016/j.mssp.2019.104770
197. A. Sharma, M. Tomar, V. Gupta, Room temperature trace level detection of NO_2 gas using SnO_2 modified carbon nanotubes based sensor. J. Mater. Chem. **22**(44), 23608–23616 (2012). https://doi.org/10.1039/C2JM35172B
198. M.-W. Ahn, K.-S. Park, J.-H. Heo, J.-G. Park, D.-W. Kim et al., Gas sensing properties of defect-controlled ZnO-nanowire gas sensor. Appl. Phys. Lett. **93**(26), 263103 (2008). https://doi.org/10.1063/1.3046726
199. M.W. Ahn, K.S. Park, J.H. Heo, D.W. Kim, K.J. Choi et al., On-chip fabrication of ZnO-nanowire gas sensor with high gas sensitivity. Sens. Actuators B Chem. **138**(1), 168–173 (2009). https://doi.org/10.1016/j.snb.2009.02.008
200. H. Zhang, J. Feng, T. Fei, S. Liu, T. Zhang, SnO_2 nanoparticles-reduced graphene oxide nanocomposites for NO_2 sensing at low operating temperature. Sens. Actuators B Chem. **190**, 472–478 (2014). https://doi.org/10.1016/j.snb.2013.08.067
201. S. Srivastava, K. Jain, V.N. Singh, S. Singh, N. Vijayan et al., Faster response of NO_2 sensing in graphene–WO_3 nanocomposites. Nanotechnology **23**(20), 205501 (2012). https://doi.org/10.1088/0957-4484/23/20/205501
202. N.G. Cho, D.J. Yang, M.-J. Jin, H.-G. Kim, H.L. Tuller et al., Highly sensitive SnO_2 hollow nanofiber-based NO_2 gas sensors. Sens. Actuators B Chem. **160**(1), 1468–1472 (2011). https://doi.org/10.1016/j.snb.2011.07.035
203. J. Zhang, S. Wang, Y. Wang, M. Xu, H. Xia et al., ZnO hollow spheres: preparation, characterization, and gas sensing properties. Sens. Actuators B Chem. **139**(2), 411–417 (2009). https://doi.org/10.1016/j.snb.2009.03.014
204. E. Oh, H.-Y. Choi, S.-H. Jung, S. Cho, J.C. Kim et al., High-performance NO_2 gas sensor based on ZnO nanorod grown by ultrasonic irradiation. Sens. Actuators B Chem. **141**(1), 239–243 (2009). https://doi.org/10.1016/j.snb.2009.06.031
205. J.H. Jun, J. Yun, K. Cho, I.-S. Hwang, J.-H. Lee et al., Necked ZnO nanoparticle-based NO_2 sensors with high and fast response. Sens. Actuators B Chem. **140**(2), 412–417 (2009). https://doi.org/10.1016/j.snb.2009.05.019
206. Z.U. Abideen, A. Katoch, J.-H. Kim, Y.J. Kwon, H.W. Kim et al., Excellent gas detection of ZnO nanofibers by loading with reduced graphene oxide nanosheets. Sens. Actuators B Chem. **221**, 1499–1507 (2015). https://doi.org/10.1016/j.snb.2015.07.120
207. R.K. Sonker, S.R. Sabhajeet, S. Singh, B.C. Yadav, Synthesis of ZnO nanopetals and its application as NO_2 gas sensor. Mater. Lett. **152**, 189–191 (2015). https://doi.org/10.1016/j.matlet.2015.03.112
208. X. Chen, Y. Shen, P. Zhou, S. Zhao, X. Zhong et al., NO_2 sensing properties of one-pot-synthesized ZnO nanowires with Pd functionalization. Sens. Actuators B Chem. **280**, 151–161 (2019). https://doi.org/10.1016/j.snb.2018.10.063
209. V. Kruefu, A. Wisitsoraat, A. Tuantranont, S. Phanichphant, Gas sensing properties of conducting polymer/Au-loaded ZnO nanoparticle composite materials at room temperature. Nanoscale Res. Lett. **9**(1), 467–467 (2014). https://doi.org/10.1186/1556-276X-9-467
210. A.V. Kolobov, J. Tominaga, From 3D to 2D: fabrication methods. *Two-Dimensional Transition-Metal Dichalcogenides* (Springer International Publishing, 2016), pp. 79–107. https://doi.org/10.1007/978-3-319-31450-1_4
211. J.N. Coleman, M. Lotya, A. O'Neill, S.D. Bergin, P.J. King et al., Two-dimensional nanosheets produced by liquid exfoliation of layered materials. Science **331**(6017), 568–571 (2011). https://doi.org/10.1126/science.1194975
212. R.-L. Chu, G.-B. Liu, W. Yao, X. Xu, D. Xiao et al., Spin-orbit-coupled quantum wires and Majorana fermions on zigzag edges of monolayer transition-metal dichalcogenides. Phys. Rev. B **89**(15), 155317 (2014). https://doi.org/10.1103/PhysRevB.89.155317
213. K. Lee, R. Gatensby, N. McEvoy, T. Hallam, G.S. Duesberg, High-performance sensors based on molybdenum disulfide thin films. Adv. Mater. **25**(46), 6699–6702 (2013). https://doi.org/10.1002/adma.201303230
214. R. Kumar, N. Goel, M. Kumar, High performance NO_2 sensor using MoS_2 nanowires network. Appl. Phys. Lett. **112**(5), 053502 (2018). https://doi.org/10.1063/1.5019296
215. M.A. Lukowski, A.S. Daniel, F. Meng, A. Forticaux, L. Li et al., Enhanced hydrogen evolution catalysis from chemically exfoliated metallic MoS_2 nanosheets. J. Am. Chem. Soc. **135**(28), 10274–10277 (2013). https://doi.org/10.1021/ja404523s
216. R. Kappera, D. Voiry, S.E. Yalcin, B. Branch, G. Gupta et al., Phase-engineered low-resistance contacts for ultrathin MoS_2 transistors. Nat. Mater. **13**(12), 1128–1134 (2014). https://doi.org/10.1038/nmat4080
217. R. Kappera, D. Voiry, S.E. Yalcin, W. Jen, M. Acerce et al., Metallic 1T phase source/drain electrodes for field effect transistors from chemical vapor deposited MoS_2. APL Mater. **2**(9), 092516 (2014). https://doi.org/10.1063/1.4896077
218. F.K. Perkins, A.L. Friedman, E. Cobas, P.M. Campbell, G.G. Jernigan et al., Chemical vapor sensing with monolayer MoS_2. Nano Lett. **13**(2), 668–673 (2013). https://doi.org/10.1021/nl3043079
219. S. Tongay, J. Zhou, C. Ataca, J. Liu, J.S. Kang et al., Broad-range modulation of light emission in two-dimensional semiconductors by molecular physisorption gating. Nano Lett. **13**, 2831–2836 (2013). https://doi.org/10.1021/nl4011172
220. Z. Lin, Y. Zhao, C. Zhou, R. Zhong, X. Wang et al., Controllable growth of large-size crystalline MoS_2 and resist-free

transfer assisted with a Cu thin film. Sci. Rep. **5**(1), 18596 (2015). https://doi.org/10.1038/srep18596

221. L. Zhan, W. Wan, Z. Zhu, Y. Xu, T.-M. Shih et al., Centimeter-scale nearly single-crystal monolayer MoS_2 via self-limiting vapor deposition epitaxy. J. Phys. Chem. C **121**(8), 4703–4707 (2017). https://doi.org/10.1021/acs.jpcc.6b12785
222. A.S. Pawbake, M.S. Pawar, S.R. Jadkar, D.J. Late, Large area chemical vapor deposition of monolayer transition metal dichalcogenides and their temperature dependent Raman spectroscopy studies. Nanoscale **8**(5), 3008–3018 (2016). https://doi.org/10.1039/C5NR07401K
223. X. Ling, Y.-H. Lee, Y. Lin, W. Fang, L. Yu et al., Role of the seeding promoter in MoS2 growth by chemical vapor deposition. Nano Lett. **14**(2), 464–472 (2014). https://doi.org/10.1021/nl4033704
224. H. Schmidt, S. Wang, L. Chu, M. Toh, R. Kumar et al., Transport properties of monolayer MoS_2 grown by chemical vapor deposition. Nano Lett. **14**(4), 1909–1913 (2014). https://doi.org/10.1021/nl4046922
225. S. Wu, C. Huang, G. Aivazian, J.S. Ross, D.H. Cobden et al., Vapor–solid growth of high optical quality MoS_2 monolayers with near-unity valley polarization. ACS Nano **7**(3), 2768–2772 (2013). https://doi.org/10.1021/nn4002038
226. J. Shi, D. Ma, G.-F. Han, Y. Zhang, Q. Ji et al., Controllable growth and transfer of monolayer MoS_2 on Au foils and its potential application in hydrogen evolution reaction. ACS Nano **8**(10), 10196–10204 (2014). https://doi.org/10.1021/nn503211t
227. H. Ago, H. Endo, P. Solís-Fernández, R. Takizawa, Y. Ohta et al., Controlled van der Waals epitaxy of monolayer MoS_2 triangular domains on graphene. ACS Appl. Mater. Interfaces **7**(9), 5265–5273 (2015). https://doi.org/10.1021/am508569m
228. J. Zhang, H. Yu, W. Chen, X. Tian, D. Liu et al., Scalable growth of high-quality polycrystalline MoS_2 monolayers on SiO_2 with tunable grain sizes. ACS Nano **8**(6), 6024–6030 (2014). https://doi.org/10.1021/nn5020819
229. S. Najmaei, J. Yuan, J. Zhang, P. Ajayan, J. Lou, Synthesis and defect investigation of two-dimensional molybdenum disulfide atomic layers. Acc. Chem. Res. **48**(1), 31–40 (2015). https://doi.org/10.1021/ar500291j
230. L. Zhang, K. Liu, A.B. Wong, J. Kim, X. Hong et al., Three-dimensional spirals of atomic layered MoS_2. Nano Lett. **14**(11), 6418–6423 (2014). https://doi.org/10.1021/nl502961e
231. L. Chen, B. Liu, M. Ge, Y. Ma, A.N. Abbas et al., Step-edge-guided nucleation and growth of aligned WSe_2 on sapphire via a layer-over-layer growth mode. ACS Nano **9**(8), 8368–8375 (2015). https://doi.org/10.1021/acsnano.5b03043
232. A. Roy, R. Ghosh, A. Rai, A. Sanne, K. Kim et al., Intra-domain periodic defects in monolayer MoS_2. Appl. Phys. Lett. **110**(20), 201905 (2017). https://doi.org/10.1063/1.4983789
233. X. Zeng, H. Hirwa, M. Ortel, H.C. Nerl, V. Nicolosi et al., Growth of large sized two-dimensional MoS_2 flakes in aqueous solution. Nanoscale **9**(19), 6575–6580 (2017). https://doi.org/10.1039/C7NR00701A
234. A. O'Neill, U. Khan, J.N. Coleman, Preparation of high concentration dispersions of exfoliated MoS_2 with increased Flake Size. Chem. Mater. **24**(12), 2414–2421 (2012). https://doi.org/10.1021/cm301515z
235. N. Liu, P. Kim, J.H. Kim, J.H. Ye, S. Kim et al., Large-area atomically thin MoS_2 nanosheets prepared using electrochemical exfoliation. ACS Nano **8**(7), 6902–6910 (2014). https://doi.org/10.1021/nn5016242
236. Z. Dai, W. Jin, M. Grady, J.T. Sadowski, J.I. Dadap et al., Surface structure of bulk 2H-MoS_2(0001) and exfoliated suspended monolayer MoS_2: a selected area low energy electron diffraction study. Surf. Sci. **660**, 16–21 (2017). https://doi.org/10.1016/j.susc.2017.02.005
237. D.L.C. Ky, B.-C. Tran Khac, C.T. Le, Y.S. Kim, K.-H. Chung, Friction characteristics of mechanically exfoliated and CVD-grown single-layer MoS_2. Friction **6**(4), 395–406 (2018). https://doi.org/10.1007/s40544-017-0172-8
238. G.Z. Magda, J. Pető, G. Dobrik, C. Hwang, L.P. Biró et al., Exfoliation of large-area transition metal chalcogenide single layers. Sci. Rep. **5**(1), 14714 (2015). https://doi.org/10.1038/srep14714
239. Y.-K. Huang, J.D. Cain, L. Peng, S. Hao, T. Chasapis et al., Evaporative thinning: a facile synthesis method for high quality ultrathin layers of 2D crystals. ACS Nano **8**(10), 10851–10857 (2014). https://doi.org/10.1021/nn504664p
240. D. Kong, H. Wang, J.J. Cha, M. Pasta, K.J. Koski et al., Synthesis of MoS_2 and $MoSe_2$ films with vertically aligned layers. Nano Lett. **13**(3), 1341–1347 (2013). https://doi.org/10.1021/nl400258t
241. M.V. Bollinger, J.V. Lauritsen, K.W. Jacobsen, J.K. Nørskov, S. Helveg et al., One-dimensional metallic edge states in MoS. Phys. Rev. Lett. **87**(19), 196803 (2001). https://doi.org/10.1103/PhysRevLett.87.196803
242. W. Zhou, X. Zou, S. Najmaei, Z. Liu, Y. Shi et al., Intrinsic structural defects in monolayer molybdenum disulfide. Nano Lett. **13**(6), 2615–2622 (2013). https://doi.org/10.1021/nl4007479
243. K.F. Mak, K. He, C. Lee, G.H. Lee, J. Hone et al., Tightly bound trions in monolayer MoS_2. Nat. Mater. **12**(3), 207–211 (2013). https://doi.org/10.1038/nmat3505
244. S. Mouri, Y. Miyauchi, K. Matsuda, Tunable photoluminescence of monolayer MoS_2 via chemical doping. Nano Lett. **13**(12), 5944–5948 (2013). https://doi.org/10.1021/nl403036h
245. A.K.M. Newaz, D. Prasai, J.I. Ziegler, D. Caudel, S. Robinson et al., Electrical control of optical properties of monolayer MoS_2. Solid State Commun. **155**, 49–52 (2013). https://doi.org/10.1016/j.ssc.2012.11.010
246. H. Nan, Z. Wang, W. Wang, Z. Liang, Y. Lu et al., Strong photoluminescence enhancement of MoS_2 through defect engineering and oxygen bonding. ACS Nano **8**(6), 5738–5745 (2014). https://doi.org/10.1021/nn500532f
247. S. Tongay, J. Zhou, C. Ataca, J. Liu, J.S. Kang et al., Broad-range modulation of light emission in two-dimensional semiconductors by molecular physisorption gating. Nano

 https://doi.org/10.1007/s40820-020-00558-3

Lett. **13**(6), 2831–2836 (2013). https://doi.org/10.1021/nl4011172

248. G. Finkelstein, H. Shtrikman, I. Bar-Joseph, Optical spectroscopy of a two-dimensional electron gas near the metal-insulator transition. Phys. Rev. Lett. **74**(6), 976–979 (1995). https://doi.org/10.1103/PhysRevLett.74.976
249. A.V. Agrawal, K. Kaur, M. Kumar, Interfacial study of vertically aligned n-type MoS_2 flakes heterojunction with p-type Cu-Zn-Sn-S for self-powered, fast and high performance broadband photodetector. Appl. Surf. Sci. **514**, 145901 (2020). https://doi.org/10.1016/j.apsusc.2020.145901
250. T.F. Jaramillo, K.P. Jørgensen, J. Bonde, J.H. Nielsen, S. Horch et al., Identification of active edge sites for electrochemical h_2 evolution from MoS_2 nanocatalysts. Science **317**(5834), 100–102 (2007). https://doi.org/10.1126/science.1141483
251. C. Kim, J.-C. Park, S.Y. Choi, Y. Kim, S.-Y. Seo et al., Self-formed channel devices based on vertically grown 2d materials with large-surface-area and their potential for chemical sensor applications. Small **14**(15), 1704116 (2018). https://doi.org/10.1002/smll.201704116
252. Y.-S. Shim, K.C. Kwon, J.M. Suh, K.S. Choi, Y.G. Song et al., Synthesis of numerous edge sites in MoS_2 via SiO_2 nanorods platform for highly sensitive gas sensor. ACS Appl. Mater. Interfaces **10**(37), 31594–31602 (2018). https://doi.org/10.1021/acsami.8b08114
253. J. Kibsgaard, Z. Chen, B.N. Reinecke, T.F. Jaramillo, Engineering the surface structure of MoS_2 to preferentially expose active edge sites for electrocatalysis. Nat. Mater. **11**(11), 963–969 (2012). https://doi.org/10.1038/nmat3439
254. L. Yang, H. Hong, Q. Fu, Y. Huang, J. Zhang et al., Single-crystal atomic-layered molybdenum disulfide nanobelts with high surface activity. ACS Nano **9**(6), 6478–6483 (2015). https://doi.org/10.1021/acsnano.5b02188
255. A.V. Agrawal, R. Kumar, S. Venkatesan, A. Zakhidov, Z. Zhu et al., Fast detection and low power hydrogen sensor using edge-oriented vertically aligned 3-D network of MoS_2 flakes at room temperature. Appl. Phys. Lett. **111**(9), 093102 (2017). https://doi.org/10.1063/1.5000825
256. A. Singh, M.A. Uddin, T. Sudarshan, G. Koley, Tunable reverse-biased graphene/silicon heterojunction Schottky diode sensor. Small **10**(8), 1555–1565 (2014). https://doi.org/10.1002/smll.201302818
257. M.A. Uddin, A.K. Singh, T.S. Sudarshan, G. Koley, Functionalized graphene/silicon chemi-diode H_2 sensor with tunable sensitivity. Nanotechnology **25**(12), 125501 (2014). https://doi.org/10.1088/0957-4484/25/12/125501
258. A.N. Abbas, B. Liu, L. Chen, Y. Ma, S. Cong et al., Black phosphorus gas sensors. ACS Nano **9**(5), 5618–5624 (2015). https://doi.org/10.1021/acsnano.5b01961
259. Y. Xu, C. Cheng, S. Du, J. Yang, B. Yu et al., Contacts between two- and three-dimensional materials: ohmic, Schottky, and p–n heterojunctions. ACS Nano **10**(5), 4895–4919 (2016). https://doi.org/10.1021/acsnano.6b01842
260. G. Lu, L.E. Ocola, J. Chen, Reduced graphene oxide for room-temperature gas sensors. Nanotechnology **20**(44), 445502 (2009). https://doi.org/10.1088/0957-4484/20/44/445502
261. M. Zhu, X. Li, S. Chung, L. Zhao, X. Li et al., Photo-induced selective gas detection based on reduced graphene oxide/Si Schottky diode. Carbon **84**, 138–145 (2015). https://doi.org/10.1016/j.carbon.2014.12.008
262. Metal-Semiconductor Contacts (Ed.), *Physics of Semiconductor Devices* (2006), pp. 134–196. https://doi.org/10.1002/9780470068328.ch3
263. K.S. Novoselov, D. Jiang, F. Schedin, T.J. Booth, V.V. Khotkevich et al., Two-dimensional atomic crystals. Proc. Natl. Aca. Sci. USA **102**(30), 10451–10453 (2005). https://doi.org/10.1073/pnas.0502848102
264. Q.H. Wang, K. Kalantar-Zadeh, A. Kis, J.N. Coleman, M.S. Strano, Electronics and optoelectronics of two-dimensional transition metal dichalcogenides. Nat. Nanotechnol. **7**(11), 699–712 (2012). https://doi.org/10.1038/nnano.2012.193
265. J. Zhou, Y. Gu, Y. Hu, W. Mai, P.-H. Yeh et al., Gigantic enhancement in response and reset time of ZnO UV nanosensor by utilizing Schottky contact and surface functionalization. Appl. Phys. Lett. **94**(19), 191103 (2009). https://doi.org/10.1063/1.3133358
266. T.-Y. Wei, P.-H. Yeh, S.-Y. Lu, Z.L. Wang, Gigantic enhancement in sensitivity using schottky contacted nanowire nanosensor. J. Am. Chem. Soc. **131**(48), 17690–17695 (2009). https://doi.org/10.1021/ja907585c
267. S. McDonnell, R. Addou, C. Buie, R.M. Wallace, C.L. Hinkle, Defect-dominated doping and contact resistance in MoS_2. ACS Nano **8**(3), 2880–2888 (2014). https://doi.org/10.1021/nn500044q
268. Y.Y. Illarionov, T. Knobloch, M. Waltl, G. Rzepa, A. Pospischil et al., Energetic mapping of oxide traps in MoS_2 field-effect transistors. 2D Mater. **4**(2), 025108 (2017). https://doi.org/10.1088/2053-1583/aa734a
269. M.C. Hersam, Defects at the two-dimensional limit. J. Phys. Chem. Lett. **6**(14), 2738–2739 (2015). https://doi.org/10.1021/acs.jpclett.5b01218
270. F. Banhart, J. Kotakoski, A.V. Krasheninnikov, Structural defects in graphene. ACS Nano **5**(1), 26–41 (2011). https://doi.org/10.1021/nn102598m
271. P. Vancsó, G.Z. Magda, J. Pető, J.-Y. Noh, Y.-S. Kim et al., The intrinsic defect structure of exfoliated MoS_2 single layers revealed by scanning tunneling microscopy. Sci. Rep. **6**(1), 29726 (2016). https://doi.org/10.1038/srep29726
272. H. Qiu, L. Pan, Z. Yao, J. Li, Y. Shi et al., Electrical characterization of back-gated bi-layer MoS_2 field-effect transistors and the effect of ambient on their performances. Appl. Phys. Lett. **100**(12), 123104 (2012). https://doi.org/10.1063/1.3696045
273. K. Barthelmi, J. Klein, A. Hötger, L. Sigl, F. Sigger et al., Atomistic defects as single-photon emitters in atomically thin MoS_2. Appl. Phys. Lett. **117**(7), 070501 (2020). https://doi.org/10.1063/5.0018557
274. B. Stampfer, F. Zhang, Y.Y. Illarionov, T. Knobloch, P. Wu et al., Characterization of single defects in ultrascaled MoS_2 field-effect transistors. ACS Nano **12**(6), 5368–5375 (2018). https://doi.org/10.1021/acsnano.8b00268

275. G. Lee, G. Yang, A. Cho, J.W. Han, J. Kim, Defect-engineered graphene chemical sensors with ultrahigh sensitivity. Phys. Chem. Chem. Phys. **18**(21), 14198–14204 (2016). https://doi.org/10.1039/C5CP04422G
276. B. Kumar, K. Min, M. Bashirzadeh, A.B. Farimani, M.H. Bae et al., The role of external defects in chemical sensing of graphene field-effect transistors. Nano Lett. **13**(5), 1962–1968 (2013). https://doi.org/10.1021/nl304734g
277. H. Terrones, R. Lv, M. Terrones, M.S. Dresselhaus, The role of defects and doping in 2D graphene sheets and 1D nanoribbons. Rep. Prog. Phys. **75**(6), 062501 (2012). https://doi.org/10.1088/0034-4885/75/6/062501
278. Y.-H. Zhang, L.-F. Han, Y.-H. Xiao, D.-Z. Jia, Z.-H. Guo et al., Understanding dopant and defect effect on H_2S sensing performances of graphene: a first-principles study. Comput. Mater. Sci. **69**, 222–228 (2013). https://doi.org/10.1016/j.commatsci.2012.11.048
279. F.A. Villamena, Chapter 2—chemistry of reactive species, in ed. by F.A. Villamena, *Reactive Species Detection in Biology* (Elsevier, 2017), pp. 13–64. https://doi.org/10.1016/B978-0-12-420017-3.00005-0
280. O. Leenaerts, B. Partoens, F.M. Peeters, Adsorption of H_2O, NH_3, CO, NO_2, and NO on graphene: a first-principles study. Phys. Rev. B **77**, 125416 (2008). https://doi.org/10.1103/PhysRevB.77.125416
281. H. Li, M. Huang, G. Cao, Markedly different adsorption behaviors of gas molecules on defective monolayer MoS2: a first-principles study. Phys. Chem. Chem. Phys. **18**(22), 15110–15117 (2016). https://doi.org/10.1039/C6CP01362G
282. H. Qiu, T. Xu, Z. Wang, W. Ren, H. Nan et al., Hopping transport through defect-induced localized states in molybdenum disulphide. Nat. Commun. **4**(1), 2642 (2013). https://doi.org/10.1038/ncomms3642
283. D. Liu, Y. Guo, L. Fang, J. Robertson, Sulfur vacancies in monolayer MoS_2 and its electrical contacts. Appl. Phys. Lett. **103**(18), 183113 (2013). https://doi.org/10.1063/1.4824893
284. H.G. Rosa, L. Junpeng, L.C. Gomes, M.J.L.F. Rodrigues, S.C. Haur et al., Second-harmonic spectroscopy for defects engineering monitoring in transition metal dichalcogenides. Adv. Opt. Mater. **6**(5), 1701327 (2018). https://doi.org/10.1002/adom.201701327
285. M.P.K. Sahoo, J. Wang, Y. Zhang, T. Shimada, T. Kitamura, Modulation of gas adsorption and magnetic properties of monolayer-MoS_2 by antisite defect and strain. J. Phys. Chem. C **120**(26), 14113–14121 (2016). https://doi.org/10.1021/acs.jpcc.6b03284
286. Y. Linghu, C. Wu, Gas molecules on defective and nonmetal-doped MoS_2 monolayers. J. Phys. Chem. C **124**(2), 1511–1522 (2020). https://doi.org/10.1021/acs.jpcc.9b10450
287. Y. Linghu, C. Wu, Gas molecules on defective and nonmetal doped MoS_2 monolayers. J. Phys. Chem. C **124**(2), 1511–1522 (2020). https://doi.org/10.1021/acs.jpcc.9b10450
288. D. Zhao, X. Fan, Z. Luo, Y. An, Y. Hu, Enhanced gas-sensing performance of graphene by doping transition metal atoms: a first-principles study. Phys. Lett. A **382**(40), 2965–2973 (2018). https://doi.org/10.1016/j.physleta.2018.06.046
289. H.-P. Komsa, S. Kurasch, O. Lehtinen, U. Kaiser, A.V. Krasheninnikov, From point to extended defects in two-dimensional MoS_2: evolution of atomic structure under electron irradiation. Phys. Rev. B **88**(3), 035301 (2013). https://doi.org/10.1103/PhysRevB.88.035301
290. Y. Jing, X. Tan, Z. Zhou, P. Shen, Tuning electronic and optical properties of MoS2 monolayer via molecular charge transfer. J. Mater. Chem. A **2**(40), 16892–16897 (2014). https://doi.org/10.1039/C4TA03660C
291. J. Suh, T.-E. Park, D.-Y. Lin, D. Fu, J. Park et al., Doping against the native propensity of MoS_2: degenerate hole doping by cation substitution. Nano Lett. **14**(12), 6976–6982 (2014). https://doi.org/10.1021/nl503251h
292. S. Qin, W. Lei, D. Liu, Y. Chen, In-situ and tunable nitrogen-doping of MoS_2 nanosheets. Sci. Rep. **4**(1), 7582 (2014). https://doi.org/10.1038/srep07582
293. B.B. Xiao, P. Zhang, L.P. Han, Z. Wen, Functional MoS_2 by the Co/Ni doping as the catalyst for oxygen reduction reaction. Appl. Surf. Sci. **354**, 221–228 (2015). https://doi.org/10.1016/j.apsusc.2014.12.134
294. J. Dai, J. Yuan, Adsorption of molecular oxygen on doped graphene: atomic, electronic, and magnetic properties. Phys. Rev. B **81**(16), 165414 (2010). https://doi.org/10.1103/PhysRevB.81.165414
295. Y.-H. Lu, M. Zhou, C. Zhang, Y.-P. Feng, Metal-embedded graphene: a possible catalyst with high activity. J. Phys. Chem. C **113**(47), 20156–20160 (2009). https://doi.org/10.1021/jp908829m
296. Y. Fan, J. Zhang, Y. Qiu, J. Zhu, Y. Zhang et al., A DFT study of transition metal (Fe Co, Ni, Cu, Ag, Au, Rh, Pd, Pt and Ir)-embedded monolayer MoS2 for gas adsorption. Comput. Mater. Sci. **138**, 255–266 (2017). https://doi.org/10.1016/j.commatsci.2017.06.029
297. H. Luo, Y. Cao, J. Zhou, J. Feng, J. Cao et al., Adsorption of NO_2, NH_3 on monolayer MoS_2 doped with Al, Si, and P: a first-principles study. Chem. Phys. Lett. **643**, 27–33 (2016). https://doi.org/10.1016/j.cplett.2015.10.077
298. J. Zhu, H. Zhang, Y. Tong, L. Zhao, Y. Zhang et al., First-principles investigations of metal (V, Nb, Ta)-doped monolayer MoS_2: structural stability, electronic properties and adsorption of gas molecules. Appl. Surf. Sci. **419**, 522–530 (2017). https://doi.org/10.1016/j.apsusc.2017.04.157
299. J. Song, H. Lou, Improvement of gas-adsorption performances of Ag-functionalized monolayer MoS2 surfaces: a first-principles study. J. Appl. Phys. **123**(17), 175303 (2018). https://doi.org/10.1063/1.5022829
300. O. Leenaerts, B. Partoens, F.M. Peeters, Paramagnetic adsorbates on graphene: a charge transfer analysis. Appl. Phys. Lett. **92**(24), 243125 (2008). https://doi.org/10.1063/1.2949753
301. J.T. Robinson, F.K. Perkins, E.S. Snow, Z. Wei, P.E. Sheehan, Reduced graphene oxide molecular sensors. Nano Lett. **8**(10), 3137–3140 (2008). https://doi.org/10.1021/nl8013007
302. J. Heising, M.G. Kanatzidis, Exfoliated and restacked MoS_2 and WS_2: ionic or neutral species? Encapsulation and ordering of hard electropositive cations. J. Am. Chem. Soc. **121**(50), 11720–11732 (1999). https://doi.org/10.1021/ja991644d

 https://doi.org/10.1007/s40820-020-00558-3

303. Y. Kim, S.-K. Kang, N.-C. Oh, H.-D. Lee, S.-M. Lee et al., Improved sensitivity in schottky contacted two-dimensional MoS_2 gas sensor. ACS Appl. Mater. Interfaces **11**(42), 38902–38909 (2019). https://doi.org/10.1021/acsami.9b10861
304. R. Kumar, P.K. Kulriya, M. Mishra, F. Singh, G. Gupta et al., Highly selective and reversible NO_2 gas sensor using vertically aligned MoS_2 flake networks. Nanotechnology **29**(46), 464001 (2018). https://doi.org/10.1088/1361-6528/aade20
305. T. Xu, Y. Pei, Y. Liu, D. Wu, Z. Shi et al., High-response NO_2 resistive gas sensor based on bilayer MoS_2 grown by a new two-step chemical vapor deposition method. J. Alloys Compd. **725**, 253–259 (2017). https://doi.org/10.1016/j.jallcom.2017.06.105
306. Y. Zhang, W. Zeng, Y. Li, Hydrothermal synthesis and controlled growth of hierarchical 3D flower-like MoS_2 nanospheres assisted with CTAB and their NO_2 gas sensing properties. Appl. Surf. Sci. **455**, 276–282 (2018). https://doi.org/10.1016/j.apsusc.2018.05.224
307. Y. Li, Z. Song, Y. Li, S. Chen, S. Li et al., Hierarchical hollow MoS_2 microspheres as materials for conductometric NO_2 gas sensors. Sens. Actuators B Chem. **282**, 259–267 (2019). https://doi.org/10.1016/j.snb.2018.11.069
308. N.T. Thang, L.T. Hong, N.H. Thoan, C.M. Hung, N. Van Duy et al., Controlled synthesis of ultrathin MoS_2 nanoflowers for highly enhanced NO_2 sensing at room temperature. RSC Adv. **10**(22), 12759–12771 (2020). https://doi.org/10.1039/D0RA00121J
309. W. Li, Y. Zhang, X. Long, J. Cao, X. Xin et al., Gas sensors based on mechanically exfoliated MoS(2) nanosheets for room-temperature NO(2) detection. Sensors **19**(9), 2123 (2019). https://doi.org/10.3390/s19092123
310. R. Kumar, N. Goel, A.V. Agrawal, R. Raliya, S. Rajamani et al., Boosting sensing performance of vacancy-containing vertically aligned MoS_2 using rGO particles. IEEE Sens. J. **19**(22), 10214–10220 (2019). https://doi.org/10.1109/JSEN.2019.2932106
311. N. Barsan, U. Weimar, Conduction model of metal oxide gas sensors. J. Electroceram. **7**(3), 143–167 (2001). https://doi.org/10.1023/A:1014405811371
312. P. Zhang, X. Lu, Y. Huang, J. Deng, L. Zhang et al., MoS_2 nanosheets decorated with gold nanoparticles for rechargeable Li–O_2 batteries. J. Mater. Chem. A **3**(28), 14562–14566 (2015). https://doi.org/10.1039/C5TA02945G
313. B.B. Li, S.Z. Qiao, X.R. Zheng, X.J. Yang, Z.D. Cui et al., Pd coated MoS_2 nanoflowers for highly efficient hydrogen evolution reaction under irradiation. J. Power Sources **284**, 68–76 (2015). https://doi.org/10.1016/j.jpowsour.2015.03.021
314. T.S. Sreeprasad, P. Nguyen, N. Kim, V. Berry, Controlled, defect-guided, metal-nanoparticle incorporation onto MoS_2 via chemical and microwave routes: electrical, thermal, and structural properties. Nano Lett. **13**(9), 4434–4441 (2013). https://doi.org/10.1021/nl402278y
315. X. Yang, H. Yu, X. Guo, Q. Ding, T. Pullerits et al., Plasmon-exciton coupling of monolayer MoS_2-Ag nanoparticles hybrids for surface catalytic reaction. Mater. Today Energy **5**, 72–78 (2017). https://doi.org/10.1016/j.mtener.2017.05.005
316. X. Yang, W. Liu, M. Xiong, Y. Zhang, T. Liang et al., Au nanoparticles on ultrathin MoS_2 sheets for plasmonic organic solar cells. J. Mater. Chem. A **2**(36), 14798–14806 (2014). https://doi.org/10.1039/C4TA03178D
317. N. Singh, R.K. Gupta, P.S. Lee, Gold-nanoparticle-functionalized In_2O_3 nanowires as CO gas sensors with a significant enhancement in response. ACS Appl. Mater. Interfaces **3**(7), 2246–2252 (2011). https://doi.org/10.1021/am101259t
318. V. Dobrokhotov, D.N. McIlroy, M.G. Norton, A. Abuzir, W.J. Yeh et al., Principles and mechanisms of gas sensing by GaN nanowires functionalized with gold nanoparticles. J. Appl. Phys. **99**(10), 104302 (2006). https://doi.org/10.1063/1.2195420
319. A. Kolmakov, D.O. Klenov, Y. Lilach, S. Stemmer, M. Moskovits, Enhanced gas sensing by individual SnO_2 nanowires and nanobelts functionalized with Pd catalyst particles. Nano Lett. **5**(4), 667–673 (2005). https://doi.org/10.1021/nl050082v
320. C. Liu, Y. Zhang, J. Hu, J. Ren, Y. Song et al., Defects suppression in MoS_2 caused by W doped for enhanced response/recovery behaviors against NO_2. Mater. Lett. **273**, 127961 (2020). https://doi.org/10.1016/j.matlet.2020.127961
321. I.-S. Hwang, J.-K. Choi, H.-S. Woo, S.-J. Kim, S.-Y. Jung et al., Facile control of C_2H_5OH sensing characteristics by decorating discrete Ag nanoclusters on SnO_2 nanowire networks. ACS Appl. Mater. Interfaces **3**(8), 3140–3145 (2011). https://doi.org/10.1021/am200647f
322. S. Kaewgun, C.A. Nolph, B.I. Lee, Enhancing photocatalytic activity of polymorphic titania nanoparticles by NMP solvent-based ambient condition process. Catal. Lett. **123**(3), 173–180 (2008). https://doi.org/10.1007/s10562-008-9490-9
323. J. Wu, H. Li, Z. Yin, H. Li, J. Liu et al., Layer thinning and etching of mechanically exfoliated MoS_2 nanosheets by thermal annealing in air. Small **9**(19), 3314–3319 (2013). https://doi.org/10.1002/smll.201301542
324. M.J. Madou, S.R. Morrison, 10—thin-film gas sensors, in eds. by M.J. Madou, S.R. Morrison, *Chemical Sensing with Solid State Devices* (Academic Press, 1989), pp. 419–435. https://doi.org/10.1016/B978-0-12-464965-1.50015-6
325. Y. Zhou, C. Gao, Y. Guo, UV assisted ultrasensitive trace NO_2 gas sensing based on few-layer MoS_2 nanosheet–ZnO nanowire heterojunctions at room temperature. J. Mater. Chem. A **6**(22), 10286–10296 (2018). https://doi.org/10.1039/C8TA02679C
326. B. Cho, A.R. Kim, Y. Park, J. Yoon, Y.-J. Lee et al., Bifunctional sensing characteristics of chemical vapor deposition synthesized atomic-layered MoS_2. ACS Appl. Mater. Interfaces **7**(4), 2952–2959 (2015). https://doi.org/10.1021/am508535x
327. G. Chen, T.M. Paronyan, E.M. Pigos, A.R. Harutyunyan, Enhanced gas sensing in pristine carbon nanotubes under continuous ultraviolet light illumination. Sci. Rep. **2**(1), 343 (2012). https://doi.org/10.1038/srep00343
328. Y. Kang, S. Pyo, E. Jo, J. Kim, Light-assisted recovery of reacted MoS_2 for reversible NO_2 sensing at room temperature. Nanotechnology **30**(35), 355504 (2019). https://doi.org/10.1088/1361-6528/ab2277

329. J. Wang, J. Deng, Y. Li, H. Yuan, M. Xu, ZnO nanocrystal-coated MoS_2 nanosheets with enhanced ultraviolet light gas sensitive activity studied by surface photovoltage technique. Ceram. Int. **46**(8, Part A), 11427–11431 (2020). https://doi.org/10.1016/j.ceramint.2020.01.157
330. K. Chang, W. Chen, l-Cysteine-assisted synthesis of layered MoS_2/graphene composites with excellent electrochemical performances for lithium ion batteries. ACS Nano **5**(6), 4720–4728 (2011). https://doi.org/10.1021/nn200659w
331. X. Zheng, J. Xu, K. Yan, H. Wang, Z. Wang et al., Space-confined growth of MoS_2 nanosheets within graphite: the layered hybrid of MoS_2 and graphene as an active catalyst for hydrogen evolution reaction. Chem. Mater. **26**(7), 2344–2353 (2014). https://doi.org/10.1021/cm500347r
332. Y. Niu, R. Wang, W. Jiao, G. Ding, L. Hao et al., MoS_2 graphene fiber based gas sensing devices. Carbon **95**, 34–41 (2015). https://doi.org/10.1016/j.carbon.2015.08.002
333. Y. Zhou, G. Liu, X. Zhu, Y. Guo, Ultrasensitive NO_2 gas sensing based on rGO/MoS_2 nanocomposite film at low temperature. Sens. Actuators B Chem. **251**, 280–290 (2017). https://doi.org/10.1016/j.snb.2017.05.060
334. H.S. Hong, N.H. Phuong, N.T. Huong, N.H. Nam, N.T. Hue, Highly sensitive and low detection limit of resistive NO_2 gas sensor based on a MoS2/graphene two-dimensional heterostructures. Appl. Surf. Sci. **492**, 449–454 (2019). https://doi.org/10.1016/j.apsusc.2019.06.230
335. M. Sangeetha, D. Madhan, Ultra-sensitive molybdenum disulfide (MoS_2)/graphene based hybrid sensor for the detection of NO_2 and formaldehyde gases by fiber optic clad modified method. Opt. Laser Technol. **127**, 106193 (2020). https://doi.org/10.1016/j.optlastec.2020.106193
336. S. Shao, L. Che, Y. Chen, M. Lai, S. Huang et al., A novel RGO-MoS_2-CdS nanocomposite film for application in the ultrasensitive NO_2 detection. J. Alloys Compd. **774**, 1–10 (2019). https://doi.org/10.1016/j.jallcom.2018.09.271
337. M.W. Jung, S.M. Kang, K.-H. Nam, K.-S. An, B.-C. Ku, Highly transparent and flexible NO_2 gas sensor film based on MoS_2/rGO composites using soft lithographic patterning. Appl. Surface Sci. **456**, 7–12 (2018). https://doi.org/10.1016/j.apsusc.2018.06.086
338. M. Ikram, Y. Zhao, A.U. Rehman, K. Kan, W. Zhang et al., Multilayer flower like MoS2 conjugated with thin layer $In(OH)_3$ for high-performance NO_x gas sensor at room temperature. J. Alloys Compd. **735**, 1439–1448 (2018). https://doi.org/10.1016/j.jallcom.2017.11.229
339. R. Kumar, N. Goel, M. Mishra, G. Gupta, M. Fanetti et al., Growth of MoS_2–MoO_3 hybrid microflowers via controlled vapor transport process for efficient gas sensing at room temperature. Adv. Mater. Interfaces **5**(10), 1800071 (2018). https://doi.org/10.1002/admi.201800071
340. S. Shi, R. Hu, E. Wu, Q. Li, X. Chen et al., Highly-sensitive gas sensor based on two-dimensional material field effect transistor. Nanotechnology **29**(43), 435502 (2018). https://doi.org/10.1088/1361-6528/aad94d
341. L. Liu, M. Ikram, L. Ma, X. Zhang, H. Lv et al., Edge-exposed MoS_2 nanospheres assembled with SnS_2 nanosheet to boost NO_2 gas sensing at room temperature. J. Hazard. Mater. **393**, 122325 (2020). https://doi.org/10.1016/j.jhazmat.2020.122325
342. G. Deokar, P. Vancsó, R. Arenal, F. Ravaux, J. Casanova-Cháfer et al., MoS_2–carbon nanotube hybrid material growth and gas sensing. Adv. Mater. Interfaces **4**(24), 1700801 (2017). https://doi.org/10.1002/admi.201700801
343. S. Zhao, Z. Li, G. Wang, J. Liao, S. Lv et al., Highly enhanced response of MoS_2/porous silicon nanowire heterojunctions to NO_2 at room temperature. RSC Adv. **8**(20), 11070–11077 (2018). https://doi.org/10.1039/C7RA13484C
344. S. Zhao, G. Wang, J. Liao, S. Lv, Z. Zhu et al., Vertically aligned MoS_2/ZnO nanowires nanostructures with highly enhanced NO_2 sensing activities. Appl. Surf. Sci. **456**, 808–816 (2018). https://doi.org/10.1016/j.apsusc.2018.06.103
345. X. Li, Y. Zhou, H. Tai, Y. Jiang, Z. Li, Nanocomposite films of p-type MoS_2 nanosheets/n-type ZnO nanowires: sensitive and low-temperature ppb-level NO_2 detection. Mater. Lett. **262**, 127148 (2020). https://doi.org/10.1016/j.matlet.2019.127148
346. Z. Yang, D. Zhang, H. Chen, MOF-derived indium oxide hollow microtubes/MoS_2 nanoparticles for NO_2 gas sensing. Sens. Actuators B Chem. **300**, 127037 (2019). https://doi.org/10.1016/j.snb.2019.127037
347. Y. Han, D. Huang, Y. Ma, G. He, J. Hu et al., Design of hetero-nanostructures on MoS_2 nanosheets to boost NO_2 room-temperature sensing. ACS Appl. Mater. Interfaces **10**(26), 22640–22649 (2018). https://doi.org/10.1021/acsami.8b05811
348. Y. Han, Y. Ma, Y. Liu, S. Xu, X. Chen et al., Construction of MoS_2/SnO_2 heterostructures for sensitive NO_2 detection at room temperature. Appl. Surf. Sci. **493**, 613–619 (2019). https://doi.org/10.1016/j.apsusc.2019.07.052
349. X. Xin, Y. Zhang, X. Guan, J. Cao, W. Li et al., Enhanced performances of PbS quantum-dots-modified MoS_2 composite for NO_2 detection at room temperature. ACS Appl. Mater. Interfaces **11**(9), 9438–9447 (2019). https://doi.org/10.1021/acsami.8b20984
350. J. Jaiswal, A. Sanger, P. Tiwari, R. Chandra, MoS_2 hybrid heterostructure thin film decorated with CdTe quantum dots for room temperature NO_2 gas sensor. Sens. Actuators B Chem. **305**, 127437 (2020). https://doi.org/10.1016/j.snb.2019.127437
351. Z. Wang, T. Zhang, C. Zhao, T. Han, T. Fei et al., Rational synthesis of molybdenum disulfide nanoparticles decorated reduced graphene oxide hybrids and their application for high-performance NO_2 sensing. Sens. Actuators B Chem. **260**, 508–518 (2018). https://doi.org/10.1016/j.snb.2017.12.181
352. S. Cui, Z. Wen, X. Huang, J. Chang, J. Chen, Stabilizing MoS_2 nanosheets through SnO_2 nanocrystal decoration for high-performance gas sensing in air. Small **11**(19), 2305–2313 (2015). https://doi.org/10.1002/smll.201402923

 https://doi.org/10.1007/s40820-020-00558-3